



Développement et optimisation d'un système de polarisation de neutrons ultra froids dans le cadre d'une nouvelle mesure du moment dipolaire électrique du neutron

E. Pierre

► To cite this version:

E. Pierre. Développement et optimisation d'un système de polarisation de neutrons ultra froids dans le cadre d'une nouvelle mesure du moment dipolaire électrique du neutron. Physique Nucléaire Expérimentale [nucl-ex]. Université de Caen, 2012. Français. NNT : . tel-00726870

HAL Id: tel-00726870

<https://theses.hal.science/tel-00726870>

Submitted on 31 Aug 2012

HAL is a multi-disciplinary open access archive for the deposit and dissemination of scientific research documents, whether they are published or not. The documents may come from teaching and research institutions in France or abroad, or from public or private research centers.

L'archive ouverte pluridisciplinaire **HAL**, est destinée au dépôt et à la diffusion de documents scientifiques de niveau recherche, publiés ou non, émanant des établissements d'enseignement et de recherche français ou étrangers, des laboratoires publics ou privés.

UNIVERSITÉ DE CAEN BASSE-NORMANDIE

UFR de science

Ecole Doctorale SIMEM

THÈSE

Présentée par

M. Edgard PIERRE

Et soutenue

le 26 mars 2012

En vue de l'obtention du

Doctorat de l'Université de Caen Basse-Normandie
Spécialité : Constituants élémentaires et physique théorique

Arrêté du 07 août 2006

Développement et optimisation d'un système de polarisation de neutrons ultra froids dans le cadre d'une nouvelle mesure du moment dipolaire électrique du neutron.

Directeur de thèse: **Oscar Naviliat-Cuncic**

MEMBRES du JURY

M. Christian Plonka-Spehr	Professeur	Université de Mayence	Rapporteur
M. Dominique Rebreyend	DR CNRS	LPSC Grenoble	Rapporteur
M. Thomas Lefort	MdC	Université de Caen	
M. Geza Zsigmond	Physicien	PSI Villigen	
M. Oscar Naviliat-Cuncic	Professeur	Université de Caen	Directeur de thèse

聞くは一時の恥、聞かぬは末代の恥.

Proverbe japonais

Résumé

Résumé

Le travail réalisé dans ce mémoire de thèse s'inscrit dans le cadre d'une expérience effectuée à l'institut Paul Scherrer (PSI) et dédiée à la mesure du moment dipolaire électrique du neutron (nEDM). Une sensibilité de 10^{-27} e cm est attendue à la fin 2013. La mesure est réalisée avec des neutrons ultra-froids (UCN) polarisés. Pour ce faire, de nouveaux systèmes de polarisation, de transport et d'inversion de spin ont été réalisés. Leur étude est présentée dans ce mémoire. Ils sont actuellement utilisés auprès de l'expérience. Grâce à des mesures de champs magnétiques effectuées sur le spectromètre, des simulations de champs réalisées avec les codes Radia et Maentouch, ainsi qu'à des simulations Monte-Carlo effectuées avec le code Geant4, l'efficacité du dispositif de polarisation a été calculée. L'efficacité mesurée en direct est de $88.5 \pm 0.3\%$, soit légèrement moins que la valeur attendue de 95%. Par ailleurs, la prise de données préliminaire effectuée en octobre 2011 a permis de déterminer certains des paramètres fondamentaux de l'expérience, tel les constantes de temps de remplissage, de stockage et de dépolarisation longitudinale du spectromètre. Ces paramètres sont encourageants pour la suite de l'expérience.

Abstract

The work presented in this thesis has been performed within the framework of an experiment located at the Paul Scherrer Institut (PSI) and dedicated to the measurement of the neutron electric dipole moment (nEDM). The expected sensitivity is 10^{-27} e cm at the end of 2013. The experiment requires a polarized ultracold neutron (UCN) beam. A new polarizing system, a spin transport device and a spin reversal system have been developed for this purpose. Their study is detailed in this thesis. These systems are currently installed on the experiment. Thanks to magnetic field mappings done on the spectrometer, to magnetic field simulations using the Radia and Maentouch programs and also to Monte-Carlo simulations using the Geant4 software, the efficiency of the device has been calculated. The measured efficiency is $88.5 \pm 0.3\%$, which

is slightly less than the expected value of 95%. Furthermore, this preliminary data taken in October 2011 allows the determination of some fundamental parameters of the experiment such as the filling, storage and longitudinal depolarization time constants of the spectrometer. These parameters are promising for the continuation of the experiment.

Remerciements

Je tiens tout d'abord à remercier mes deux rapporteurs de thèse **Dominique Rebreyend** et **Christian Plonka-Spehr** pour avoir jugé mon travail et m'avoir apporté de nombreux commentaires qui m'ont permis d'avancer.

Mes remerciements vont ensuite à mon directeur de thèse **Oscar Naviliat-Cuncic**, qui même si nous nous sommes croisés (mon retour au LPC coïncidant à quelques semaines prêt à son départ pour les USA) a été disponible pour moi quand j'en avais besoin. J'ai eu l'occasion d'être bien encadré durant mon séjour à PSI par **Geza Zsigmond**, merci donc de m'avoir supporté (dans le même bureau qui plus est) pendant un an et demi. Durant mon séjour au LPC, j'ai eu deux encadrants de qualité que je souhaite tout particulièrement remercier. Tout d'abord **Thomas Lefort**, avec qui je travaille depuis maintenant 7 ans (c'est lui qui m'a fait découvrir les UCN en L2, souvenirs souvenirs...), pour avoir été un enseignant exemplaire, et un encadrant patient et attentif. Je dis aussi un énorme merci à **Gilles Quéméner**, pour son aide, sa sympathie et toute les fois où j'ai pu l'embêter dans son bureau durant de longs moments...

Ma thèse a duré trois ans et trois mois. Durant cette période, j'ai été amené à travailler avec beaucoup de personnes dans deux pays différents. Je remercierais en premier lieu le groupe UCN du PSI qui m'a accueilli de décembre 2008 à mai 2010. Merci à **Klaus Kirch** et à **Manfred Daum** pour leurs conseils et leur connaissances des UCN. Merci aux ingénieurs du groupe : **Michi Meier** et **Fritz Burri**, leur support technique et leurs idées m'ont été très utiles. Merci aussi aux PhD du groupe: **Martin Fertl**, **Bea Franke**, **Lenny Göttl**, **Marlon Horras**, **Andreas Knecht** et **Johannes Zenner** pour la bonne humeur générale au labo. Enfin, je n'oublie pas les "senior scientists" : **Aliko Mtchedlishvili**, **Zema Chowdhuri**, **Philipp Schmidt-Wellenburg**, **Jochen Krempel**, **Bernhard Lauss** et **Reinhold Henneck** pour leur aide durant cette année et demi en terre helvétique. Merci aussi à toute l'équipe technique s'occupant de la source d'UCN pour m'avoir permis de prendre mes données en toute fin de thèse. Enfin, un grand "danke schön" à mes collocataires de Baden : **Didi**, **Nik**, **Ju**, **Sigi** et **Louis**.

Au LPC, ou j'ai créché de juin 2010 à avril 2012, je dis merci aux autres membres du groupe UCN pas encore cités, à savoir **Yves Lemiere**, **Maitre Gilles Ban**, l'ancien thésard **Gwendal**

Rogel (merci pour les conseils sur Geant4) et le nouveau **Victor Helaine**. Bon courage pour la suite, enjoy ton séjour en Suisse ! Au delà de mon groupe de travail, merci aux thésards du groupe interactions fondamentales (**Nono Chapon**, **Nono Leredde**, **Claire Couratin** et **Philippe Velten**) en particulier, aux autres thésards en général, et à tout les membres du labo en encore plus général. Merci en particulier, tout de même, à mon collègue de bureau **Julien “Gib” Gibelin**, ainsi qu’à tout les participants des “soirées jeux”. En dehors du labo, merci à ma colloc *ad interim* **Fanny** pour m’avoir évité la rue en fin de thèse, **Tutur**, **Anne-So** et **Mich** pour les bons moments. Un merci particulier à deux amis de longue date, ami dodécennal (**Dams**) et ami vicennal (**Tiny**) pour m’avoir fait oublier mes UCN le temps d’un verre ou d’une partie de xboite.

Enfin, merci à mes amis non cités ci-dessus (**Fruck**, **Elise**, **Tiph**, **Phil** et bien d’autres...), ainsi qu’à ma famille proche pour tout le soutien qu’ils ont pu m’apporter durant la réalisation de cette thèse.

Ces remerciements sont maintenant terminé, passons à la physique...

Table des matières

Résumé	I
Remerciements	III
Table des Matières	V
I La thèse en français	1
Résumé	3
1 Le moment dipolaire électrique du neutron	5
1.1 Motivations physiques	5
1.2 État de l’art	6
1.3 Les neutrons ultra-froids	7
2 Dispositif expérimental	9
2.1 Principe de mesure	9
2.2 Dispositif expérimental à PSI	10
3 Travail de thèse	13
3.1 Modifications du dispositif existant	13
3.1.1 L’aimant supraconducteur	14
3.1.2 Le système de guidage du spin	14
3.1.3 Le nouveau spin flipper adiabatique	15
3.2 Simulations	16
3.2.1 Dépolarisations dues aux inhomogénéités du champ magnétique	16
3.2.2 Dépolarisations dues aux collisions	17
3.3 Mesures	17

3.3.1	Efficacité de polarisation et de maintien du spin	17
3.3.2	Test des bobines de guidage	18
3.4	Resultats obtenus	18
Conclusions		19
 II Appendixes in english		 21
Summary		23
1	Electric dipole moments and ultracold neutrons	25
1.1	The Electric Dipole moment	25
1.1.1	Definition and motivations	25
	EDM and the Standard Model	25
	EDM beyond the Standard Model	27
1.1.2	EDM of atoms	28
	Paramagnetic atoms	28
	Diamagnetic atoms	28
1.1.3	The Neutron EDM	28
1.2	Ultracold neutrons	30
1.2.1	Definition	30
1.2.2	Interactions	30
	Gravitational interaction	31
	Strong interaction	31
	Interaction with a nucleus	31
	Interaction with a set of nuclei	32
	Weak interaction	34
	Electromagnetic interaction	34
	Interaction with a magnetic field	34
	Interaction with an electric field	36
1.2.3	Production	36
	The PSI UCN source	37
2	The nEDM experiment	39
2.1	Principle of the nEDM measurement	39
2.1.1	The Ramsey separated oscillatory field method	40
2.1.2	Application to the nEDM experiment	41
2.2	The nEDM apparatus at PSI	42
2.2.1	Overview	42
2.2.2	UCN transport	44
	polarizer - analyzer - spin flippers	44
	UCN guides	44
	UCN switch	44
	Precession chamber	45
	Detector	46
2.2.3	Magnetometry	47

	The mercury co-magnetometer	47
	The cesium magnetometer	47
2.2.4	High voltage	47
2.2.5	Magnetic field	47
	Four layers magnetic shield	47
	B_0 coil	48
	Trim coils	48
	Surrounding Field Compensation coils	49
3	Spin transport: the guiding field system	51
3.1	Introduction	51
3.2	Depolarization due to magnetic field inhomogeneities, adiabaticity parameter . .	51
3.3	The PSI setup: changes with respect to the ILL setup	54
3.4	Creation and optimization of the new Guiding Field system	54
3.4.1	Simulations with Radia	54
	The horizontal guiding field	56
	The vertical guiding field	61
3.4.2	Comparison with a first measurement	66
3.4.3	Simulations with Maentouch	68
	Adiabaticity parameter calculation along the vertical guide	68
	Summary of the new simulated coils	71
3.4.4	Vertical guide mapping	71
	Experimental setup	71
	Magnetic field corrections, errors estimation	72
	Analysis	76
	Comparison between Maentouch simulations and measurements . .	76
	Comparison B_0 up/down	79
	Comparison on/off axis	79
	Effect of the UCN chimney (UCK) coil	79
	Effect of the stray field of the guiding field coils on the precession chamber	81
	Improvement of the influence of external fields	81
3.5	Conclusion	82
4	UCN losses and depolarization	85
4.1	Introduction	85
4.2	The Monte Carlo simulation	85
4.2.1	Physical context of the UCN simulation	85
	Treatment of wall collisions	86
	The UCN spin treatment	86
4.2.2	Materials properties	86
4.3	Input parameters	87
4.3.1	The simulated experimental setup	87
4.4	Depolarization due to wall collisions	87
4.4.1	Filling phase	88
	UCN velocity and position distributions	88

	Polarization efficiency	90
	Depolarizations due to wall collisions during the filling phase	90
4.4.2	Storage phase	91
	Velocity and position distributions	91
	UCN losses	92
	Depolarizations due to wall collisions	92
4.4.3	Emptying phase	92
	Velocity and position distributions	93
	Depolarizations due to wall collisions	93
4.4.4	Conclusion	93
4.5	Depolarization due to field inhomogeneities	93
4.5.1	Formalism of the method	93
4.5.2	Depolarizations calculation	94
4.6	The longitudinal depolarization time T_1	94
4.6.1	Contribution on T_1 due to the wall collisions	95
	Preliminary calculation	95
	Monte Carlo simulation	95
4.6.2	Dependence of T_1 with magnetic field gradients, Redfield Theory	96
4.7	Conclusion	98
5	Study of the UCN polarization analysis, performance of the apparatus	101
5.1	Polarization principle	101
5.2	Polarizing or analyzing foils	101
5.3	The new UCN polarizer	102
5.3.1	Description of the magnet	103
5.3.2	Characterization	104
5.4	Spin reversal : the adiabatic spin flipper	106
5.4.1	Principle	106
5.4.2	Adaptions for the new experiment	108
5.4.3	Experimental setup	109
5.4.4	Analysis	112
	Scanning parameters	112
	Optimization of f	113
	Determination of the spin flipper efficiency at PSI.	113
5.5	Efficiency of the polarization analysis	114
5.5.1	Experimental setup, measurements	114
5.5.2	Extraction of the polarization	116
5.6	UCN within the precession chamber	117
5.6.1	Experimental setup	117
5.6.2	Filling of the apparatus with UCN	117
5.6.3	Storage of the UCN	119
5.6.4	Depolarization within the vertical guide	120
5.6.5	Guiding field coils tests	120
5.6.6	Estimation of the longitudinal depolarization time T_1	122
5.7	Conclusion	122

Conclusions	125
A Appendix	i
.1 The monitoring using an external detector	i
List of Tables	iii
List of Figures	v
List of Symbols	xi
List of Abbreviations	xiii

Première partie

La thèse en français

Résumé

Le modèle standard (SM), qui décrit le monde des particules élémentaires et leurs interactions est communément utilisé depuis 40 ans. Néanmoins, celui ci n'arrive pas à expliquer la violation charge-parité (CP) qui est pourtant nécessaire pour expliquer l'asymétrie matière anti-matière (BAU) dans l'Univers [1]. Des extensions du SM ont été formulées dans le but d'introduire de nouvelles sources de violation CP. Une valeur non nulle du moment dipolaire électrique d'une particule (EDM), nul au premier ordre dans le cadre du SM, permet de tester ces extensions [2]. L'EDM de diverses particules est actuellement mesuré dans plusieurs expériences. Le neutron est ici considéré, la limite actuelle de l'EDM du neutron (nEDM) est : $|d_n| < 2.9 \cdot 10^{-26} e \text{ cm}$ (90 % C.L) [3]. La collaboration européenne "nEDM" a prévu d'atteindre la sensibilité de 10^{-27} - $10^{-28} e \text{ cm}$. Une nouvelle source de neutrons ultrafroids (UCN) a été développée pour cette mesure à l'institut Paul Scherrer (PSI). Ce projet est constitué de trois phases :

- la Phase I (2005-2008) a eu lieu à l'institut Laue Langevin (ILL). L'ancien spectromètre (OILL) qui a été utilisé pour obtenir la limite actuelle a été amélioré. Cette phase a principalement été une phase de recherche et développement, spécialement pour le système de magnétométrie. Une mesure de l'nEDM a eu lieu à la fin de l'année 2008 [4].
- la Phase II (2009-2014) se déroule à PSI. Le spectromètre OILL a été déplacé de l'ILL à PSI en mars 2009 et installé près de la nouvelle source. Plusieurs effets systematiques ont été mesurés, la phase de recherche et développement a continué et les performances de l'appareillage ont été testées. Une sensibilité de $10^{-27} e \text{ cm}$ devrait être atteinte à la fin de cette phase. De plus, un nouveau spectromètre est construit en parallèle de la prise de données.
- la Phase III (2014-2016) aura lieu à PSI. Le nouveau spectromètre sera utilisé pour une prise de données de deux ans à l'issue de laquelle la sensibilité de $10^{-28} e \text{ cm}$ devrait être atteinte.

Le travail développé dans cette thèse est principalement dédié au développement, aux tests et à l'optimisation d'un nouveau système de polarisation pour les UCN.

Le premier chapitre de ce document décrit les principales motivations concernant la mesure du moment dipolaire électrique du neutron. Un résumé des propriétés physiques des UCN est aussi donné. Le deuxième chapitre concerne quant à lui le principe de mesure de l'EDM. Le dispositif expérimental OILL y est décrit. Enfin, le troisième chapitre traite des développements réalisés au cours de cette thèse, au niveau de la polarisation et du maintien du spin entre le polariseur et le détecteur, ainsi que des mesures expérimentales réalisées à l'aide du dispositif OILL.

CHAPITRE

1

Le moment dipolaire électrique du neutron

1.1 Motivations physiques

Le moment dipolaire électrique intrinsèque \vec{d} d'une particule est défini comme étant proportionnel à son spin \vec{S} . Lorsque la particule est plongée dans un champs électrique \vec{E} , le Hamiltonien de l'interaction s'écrit alors :

$$H = -d\vec{E} \cdot \vec{S} \quad (1.1)$$

En 1950, Purcel et Ramsey [5] suggèrent d'utiliser le moment dipolaire électrique du neutron comme un test de la violation de symétrie de parité P et de renversement du temps T. En appliquant les opérateurs P et T sur le Hamiltonien défini précédemment, il vient :

$$H = -\vec{d} \cdot \vec{E} \xrightarrow{P} \vec{d} \cdot \vec{E}$$

et

$$H = -\vec{d} \cdot \vec{E} \xrightarrow{T} \vec{d} \cdot \vec{E}$$

En effet, les opérateurs P et T appliqués sur \vec{E} et \vec{S} donnent :

$$\begin{array}{ll} \vec{E} \xrightarrow{P} -\vec{E} & \vec{S} \xrightarrow{P} \vec{S} \\ \vec{E} \xrightarrow{T} \vec{E} & \vec{S} \xrightarrow{T} -\vec{S} \end{array}$$

Les symétries T et P sont ainsi brisées. En supposant la validité du théorème CPT, une valeur non nulle de l'EDM brise la symétrie CP puisque T est aussi brisée. La violation CP est importante en physique puisque celle ci est, d'après Sakharov [1], une condition *sine qua non* à l'existence de l'asymétrie matière-antimatière observée dans la genèse de l'univers. Le modèle théorique utilisé actuellement pour décrire la physique des particules est le modèle standard (SM). Ce modèle contient deux sources de brisure de symétrie CP : une dans le secteur

électrofaible et l'autre dans la chromodynamique quantique (QCD). La première est la phase complexe de la matrice CKM qui régit le mélange des quarks. L'existence de cette phase induit donc une limite pour la valeur de l'EDM du neutron, qui est d'environ $10^{-32} e \text{ cm}$, soit 6 ordres de grandeur en dessous de la limite expérimentale actuelle. La seconde source de violation CP vient du Lagrangien de la chromodynamique quantique, et plus particulièrement de l'angle du vide θ . Il s'agit d'un paramètre dont la valeur doit être proche de l'unité. Ce paramètre est aussi contraint par la valeur de l'EDM du neutron. Avec la limite actuelle, θ est contraint à être inférieur à 10^{-10} . Ce phénomène inattendu est appelé “the strong CP problem”, et ne trouve pas de réponse satisfaisante dans le cadre du SM. Des extensions du SM sont ainsi formulées, et la valeur de l'nEDM permet de les tester. À titre d'exemple, le MSSM est contraint par une valeur de l'nEDM comprise entre 10^{-26} et $10^{-28} e \text{ cm}$. Une formulation plus complète des motivations physiques poussant à mesurer l'EDM du neutron peut être trouvée dans le chapitre 1 des annexes en anglais.

1.2 État de l'art

La limite supérieure sur la valeur de l'EDM du neutron a diminué de six ordres de grandeur depuis la première mesure effectuée en 1950 et la dernière valeur en 2006, mettant ainsi des contraintes strictes sur les modèles théoriques au delà du modèle standard. La figure 1.1 montre l'évolution de la limite supérieure sur la valeur de l'EDM du neutron.

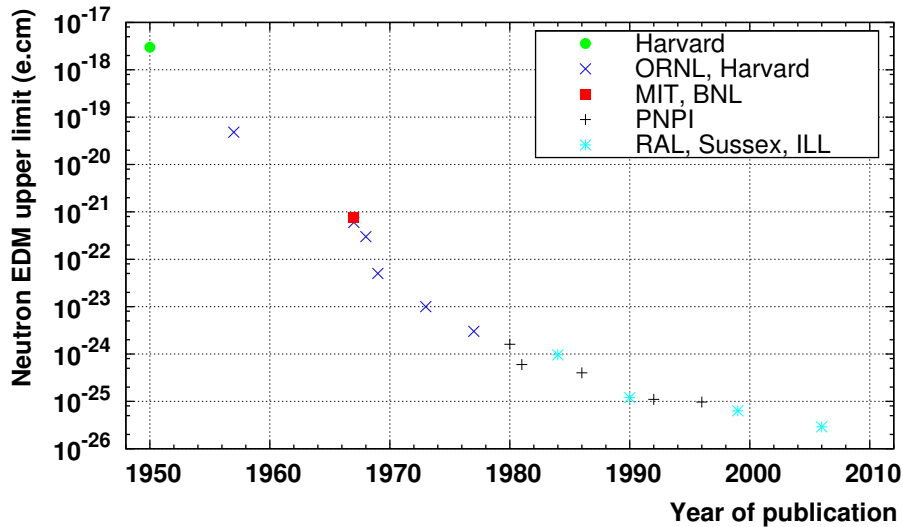


FIGURE 1.1 : Évolution de la limite sur la valeur du moment dipolaire électrique du neutron.

Les premières expériences de recherche du moment dipolaire électrique du neutron utilisaient des faisceaux de neutrons thermiques (et plus tard froids) pour effectuer la mesure. La première limite fut donnée par Ramsey [6] suite à une réanalyse des données de Havens, Rabi et Rainwater [7]. La première mesure directe fut celle de Smith, Purcell et Ramsey [8] qui conduisit à l'obtention d'une limite de $|d_n| < 5 \cdot 10^{-20} e \text{ cm}$. Les faisceaux de neutrons ont été utilisés jusqu'en 1977 pour des expériences nEDM. À ce stade, les effets systématiques liés aux vitesses élevées des neutrons dans le faisceau (effet $\vec{v} \times \vec{E}$) étaient devenu insurmontables. La limite finale obtenue

avec un faisceau de neutrons froids est $|d_n| < 3 \cdot 10^{-24} \text{ e cm}$ [9]. Il fallait trouver un autre moyen de déterminer l'nEDM. C'est ainsi que les expériences avec des neutrons ultra-froids prirent le relais. La première a eu lieu en 1980 avec une expérience à l'Institut de Physique Nucléaire de Saint Petersburg (PNPI), et une limite de $|d_n| < 1.6 \cdot 10^{-24} \text{ e cm}$ [10] fut obtenue. En 26 ans, cette limite fut réduite de deux autres ordres de grandeur.

1.3 Les neutrons ultra-froids

Les neutrons ultra-froids sont des neutrons de très basse énergie, de l'ordre de la centaine de neV. La température correspondante est de l'ordre du mK, d'où la dénomination “ultra-froid”. Outre leur neutralité et leur longue durée de vie d'environ 15 minutes (qui sont des propriétés inhérentes du neutron), leur principal attrait est leur propriété de confinement, ce qui en font des particules de choix pour des études à basse énergie. En effet, un neutron d'énergie E arrivant sur une surface avec un angle d'incidence θ peut être réfléchi si :

$$\sin \theta \leq \sqrt{\frac{V_F}{E}} \quad (1.2)$$

où V_F est le “potentiel de Fermi”, une propriété du matériau. L'énergie des UCN est si faible que l'inégalité (1.2) est vérifiée quel que soit l'angle θ . Il est ainsi possible de stocker les UCN. De plus, l'énergie des UCN est du même ordre de grandeur que l'énergie mise en jeu lors de l'interaction avec trois des quatre forces fondamentales (gravitation, forte et électromagnétique). En effet, un UCN est soumis à la gravité et gagne environ 100 neV par mètre de chute. Il existe un couplage entre un champ magnétique et le moment magnétique du neutron. Le gain (ou la perte, suivant l'état de spin de l'UCN) d'énergie est de 60 neV par T. Enfin, l'interaction forte gouverne l'interaction de l'UCN avec les matériaux par le biais du potentiel de Fermi. La valeur de ce potentiel est de l'ordre de quelques centaines de neV. Il est ainsi possible d'utiliser les UCN pour tester les interactions fondamentales. Les propriétés des UCN sont décrites plus en détail dans le chapitre 1 des annexes en anglais.

CHAPITRE

2

Dispositif expérimental

2.1 Principe de mesure

La technique de mesure du moment dipolaire électrique du neutron est restée fondamentalement la même depuis la première mesure faite par Purcell et Ramsey en 1957. Un neutron est placé dans une région dans laquelle règne un champ électrique de forte intensité \vec{E} et un champ magnétique de faible intensité \vec{B}_0 . Le Hamiltonien de l'interaction s'écrit alors :

$$H = -\vec{d}_n \cdot \vec{E} - \vec{\mu}_n \cdot \vec{B}_0 \quad (2.1)$$

Le Hamiltonien peut aussi s'écrire en fonction de la fréquence de précession du neutron ω_n : $H = \hbar\omega_n/2$. Il s'agit maintenant de considérer les deux configurations où les champs magnétique et électrique sont parallèles ($\uparrow\uparrow$) ou anti-parallèles ($\uparrow\downarrow$). En soustrayant les deux énergies et en supposant que le champ magnétique ne change pas entre les deux configurations, il est possible d'extraire l'expression de l'EDM du neutron :

$$d_n = -\frac{\hbar}{4E}(\omega_{L\uparrow\uparrow} - \omega_{L\uparrow\downarrow}) \quad (2.2)$$

Une mesure de la fréquence de précession du neutron dans les deux configurations permet ainsi de mesurer l'EDM. Ces deux fréquences sont très proches. En effet, la limite supérieure actuelle sur la valeur de l'EDM induit une différence de fréquence de 10^{-7} Hz. La méthode de Ramsey est utilisée pour déterminer cette différence de fréquence (plus de détails se trouvent dans le chapitre 2 des annexes en anglais). Pour cela, les neutrons sont polarisés et placés dans une région où règne des champs électrique et magnétique colinéaires, selon l'axe z . Puis un champ radiofréquence est appliqué à la fréquence de résonance des neutrons pour placer leur spin dans le plan $x0y$, où ils précessent librement durant un temps T . Durant cette période, les neutrons acquièrent un décalage de phase directement proportionnel au temps de précession libre et

au décalage de fréquence induit par une valeur non nulle de l'EDM du neutron. A la fin du temps de precession libre, un second champ radiofréquence est appliqué pour basculer le spin des neutrons selon l'axe z , puis les neutrons sont analysés et détectés. L'EDM du neutron est proportionnel au nombre de neutrons de spin haut (N_+) et de spin bas (N_-) comptés pour les configurations ($\uparrow\uparrow$) et ($\uparrow\downarrow$) :

$$d_n = -\frac{\hbar(\Delta N_{\uparrow\uparrow} - \Delta N_{\uparrow\downarrow})}{4\alpha T E N_0} \quad (2.3)$$

avec $N_0 = N_+ + N_-$, $\Delta N = N_+ - N_-$ et α un paramètre nommé visibilité et dépendant du pouvoir d'analyse du système de polarisation. L'erreur statistique sur la valeur de l'EDM du neutron est alors :

$$\sigma_{d_n} = \frac{\hbar}{2\alpha T E \sqrt{N_0}} \quad (2.4)$$

Il est ainsi possible de diminuer l'incertitude statistique en augmentant le nombre de neutrons détecté. Pour cette raison, l'appareillage OILL a été transporté de l'ILL (où la densité de neutron est de 50 cm^{-3}) à PSI (où la densité de neutron attendue est de 1000 cm^{-3}). Une grande visibilité permet aussi de diminuer l'erreur statistique. Le but de ce travail de thèse est d'améliorer le système de polarisation dans le but d'améliorer la visibilité.

2.2 Dispositif expérimental à PSI

La figure 2.1 montre le schéma du spectromètre OILL tel qu'il est en octobre 2011. Une description complète du dispositif expérimental se trouve dans le chapitre 2 des annexes en anglais.

Les UCN sont produits dans la source et sont polarisés grâce au polariseur supraconducteur (voir chapitre suivant). Ils sont ensuite guidés dans le "switch" (dispositif permettant de choisir dans quelle direction les UCN sont transportés) vers la chambre de precession où règne un champ magnétique homogène et vertical (\vec{B}_0) de $1 \mu\text{T}$. Ce champ magnétique est protégé des fluctuations extérieures grâce à quatre couches de blindage magnétique en Mu-métal, ainsi que d'un système de compensation actif de champ magnétique. Ce système est constitué de trois paires de bobines en configuration Helmholtz nommées SFC (pour "Surrounding Field Compensation coils"). L'homogénéité du champ dans la chambre est contrôlée par deux systèmes de magnétométrie : le co-magnétomètre mercure qui est placé dans la même enceinte que les UCN, et des magnétomètres césium à l'extérieur de la chambre. La phase de remplissage dure environ 40 s. Une haute tension de l'ordre de $\pm 12 \text{ kV/cm}$ est alors appliquée. Le spin des UCN est placé dans le plan xOy grâce à un champ magnétique radiofréquence, puis précesse librement pendant environ 150 s. Enfin, un second champ RF est appliqué, la chambre de precession est ouverte (le "switch" est placé en position de vidage), puis le spin des neutrons est analysé. Il est à noter que l'analyseur ne permet le passage que d'un seul état de spin. Il faut donc utiliser un système de renversement de spin (appelé "spin flipper" et décrit dans le chapitre suivant) pour pouvoir laisser passer, et donc détecter les UCN ayant l'autre état de spin. En supposant un nombre de neutrons détecté de 350000 par cycle de mesure, et une visibilité de 0.75, l'erreur statistique est de $\sigma_{d_n} = 4 \times 10^{-25} \text{ ecm}$ par cycle, soit $\sigma_{d_n} = 3 \times 10^{-27} \text{ ecm}$ par an. Cette valeur nous permettrait d'atteindre une nouvelle limite pour l'EDM du neutron de $|d_n| < 4 \times 10^{-27} \text{ ecm}$ (95% C.L.) après deux ans de prise de données.

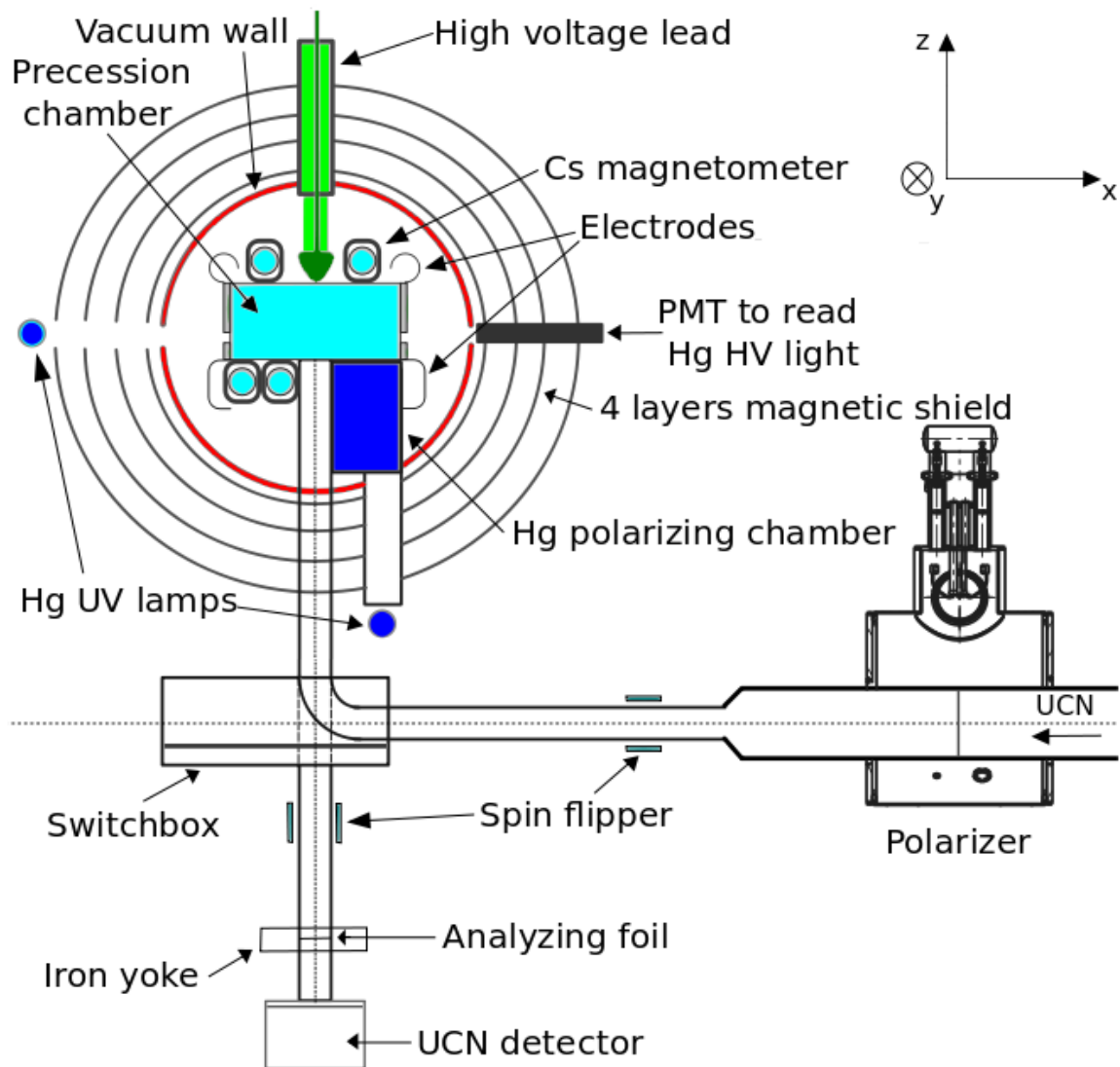


FIGURE 2.1 : Schéma de l'expérience nEDM à PSI.

CHAPITRE

3

Travail de thèse

Les travaux effectués durant cette thèse peuvent être classés en trois parties distinctes. La première concerne la conception et les tests du système de polarisation-analyse, qui ont eu lieu principalement à PSI. La deuxième partie traite de simulations Monte-Carlo ayant pour but de quantifier les dépolarisations qui peuvent avoir lieu dans l'appareillage. Ces simulations furent effectuées au LPC. Enfin, la dernière partie présente les résultats expérimentaux obtenus avec OILL.

3.1 Modifications du dispositif existant

Le dispositif OILL a subi de nombreuses améliorations depuis sa remise en fonctionnement en 2005 jusqu'à ce jour. L'une d'elles est l'amélioration du système de polarisation et d'analyse de spin des neutrons ultra-froids. A l'ILL, les UCN étaient polarisés grâce à une couche de fer (épaisseur de l'ordre de la centaine de nm) déposée sur une feuille d'aluminium (épaisseur de l'ordre de la dizaine de μm). La feuille de fer était magnétisée grâce à un système d'aimants permanents disposés autour de celle-ci. Les UCN voient ainsi une barrière de potentiel lorsqu'ils arrivent sur la feuille. La hauteur de cette barrière dépend du spin des UCN. Un état de spin sera réfléchi par la feuille de polarisation, et l'autre état sera transmis. Il s'agit ainsi d'un processus de polarisation par transmission. L'intensité du faisceau d'UCN est ainsi divisée par deux à l'entrée du polariseur (en supposant un faisceau initial entièrement dépolarisé). Il existe une probabilité pour les UCN d'être absorbés dans la feuille de polarisation, ce qui réduit le nombre de neutrons détectés à la fin d'un cycle. Il est aussi possible que les UCN se dépolarisent lors d'un rebond sur la feuille ou lors de la transmission dans la feuille. Dans ce cas, le paramètre α est dégradé. Le système de polarisation a donc été modifié dans le but de réduire ces deux effets. Néanmoins, même si le polariseur a été changé, l'analyse de spin se fait de la même manière à PSI qu'à l'ILL, pour des raisons de géométrie et d'encombrement.

3.1.1 L'aimant supraconducteur

Le nouveau système de polarisation est une bobine de type solénoïde supraconductrice délivrant un champ magnétique axial de 5 T en son centre. Une bobine générant un champ magnétique de cette intensité peut en effet être utilisée en tant que polariseur. Le champ magnétique à l'intérieur d'une feuille de fer est de l'ordre de 2 T, ce qui équivaut à un potentiel magnétique de 120 neV. À cela s'ajoute le potentiel de Fermi du fer, qui est de 210 neV. Il est ainsi possible de polariser les UCN dont l'énergie est comprise entre 90 et 330 neV. La figure 3.1 illustre ce principe. L'UCN voit une barrière de potentiel positive ou négative suivant son état de spin (terme $-\vec{\mu} \cdot \vec{B}$) et une composante positive indépendante du spin (terme V_F). Le potentiel associé au champ de 5 T est

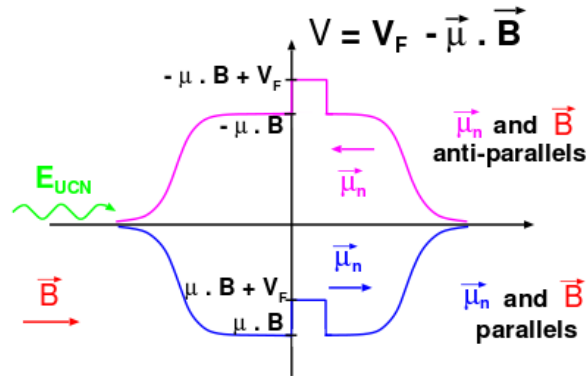


FIGURE 3.1 : Principe de polarisation de neutrons à travers une feuille de fer. Le potentiel vu par le neutron dépend de son spin.

de 300 neV. Il est donc possible de polariser les neutrons ayant une énergie inférieure à 300 neV, tout en évitant les interactions dues à la transmission dans un élément ferromagnétique.

L'aimant supraconducteur a été acheté à une entreprise. Une partie de ce travail de thèse a consisté à mettre en fonctionnement cet aimant, et le caractériser. Cela passe par une mesure du champs produit par l'aimant, pour vérifier que celui ci répond aux spécificités demandées. Une carte de champs théorique a été fournie par l'entreprise. Les mesures ont ainsi pu être comparées aux valeurs attendues. Il en résulte un accord entre les valeurs calculées et mesurées à la fois pour des valeurs de champs élevées (supérieur au Tesla) ainsi que pour les valeurs de champ de fuite entre 1 G et 1 T. Le champ de fuite lointain (intensité inférieure à 1 G) mesuré n'est pas en accord avec les valeur théoriques : la composante axiale est plus importante d'environ 30% par rapport à la valeur attendue. Néanmoins, ceci est sans incidence pour l'expérience, le blindage absorbant le champ de fuite lointain. L'aimant supraconducteur peut donc être utilisé avec des neutrons ultra-froids. Plus de détails concernant le polariseur sont donnés dans le chapitre 5 des annexes en anglais.

3.1.2 Le système de guidage du spin

La situation concernant le maintien du spin des UCN entre le polariseur et la chambre de stockage est devenue différente depuis le changement du polariseur. A l'ILL, le champ de fuite des aimants permanents du polariseur ajouté au champ magnétique terrestre permettait un transport adiabatique du spin. A PSI, l'aimant supraconducteur se situe à environ trois mètres

de la chambre. Le champ de fuite de l'aimant est insuffisant pour maintenir une polarisation suffisante le long du trajet. De plus, le champ terrestre est maintenant compensé par les bobines SFC. Il faut donc ajouter de nouvelles sources de champs magnétique pour permettre un transport de spin avec le moins de dépolarisation possible. Deux programmes de simulation de champs magnétique (RADIA et MAENTOUCH) furent utilisés pour la création et l'optimisation du nouveau système. Ce système doit limiter la dépolarisation des UCN dans le guide suite à une variation brusque du champ magnétique.

En présence d'un champ magnétique, les UCN précessent autour de celui-ci à une fréquence directement proportionnelle à l'intensité du champ. Le spin d'un UCN plongé dans un champ magnétique restera aligné à celui-ci si les variations du champ ω_{champ} sont bien moins rapides que la fréquence de précession de Larmor du spin ω_L . Cela se traduit par un coefficient d'adiabaticité, défini comme étant le rapport de la fréquence de précession par la fréquence de rotation du champ :

$$k = \frac{\omega_L}{\omega_{champ}} \quad (3.1)$$

Ce coefficient doit rester bien plus grand que 1 et une valeur de 10 sera le seuil retenu. Une cartographie du guide vertical fut effectuée après le placement des nouvelles bobines de correction pour vérifier que les variations du champ magnétique dans le guide sont bien adiabatiques. Le minimum du coefficient d'adiabaticité mesuré est supérieur à 12. Le nouveau système de maintien de spin est composé de sept nouvelles bobines :

- deux solénoïdes placés sur le guide horizontal.
- trois bobines rectangulaires placées sur le “switch”.
- une bobine “saddle” au dessus du “switch”, le long du guide vertical.
- un petit solénoïde placé à l'extrémité de la bobine “saddle”.

Plus de détails concernant le système de guidage de spin sont donnés dans le chapitre 3 des annexes en anglais.

3.1.3 Le nouveau spin flipper adiabatique

Le polariseur ne peut laisser passer qu'un seul et unique état de spin. Or, le second état de spin doit aussi être mesuré pour pouvoir calculer le pouvoir de polarisation-analyse du dispositif. Pour cela, il faut ajouter à l'appareillage un dispositif permettant de renverser le spin des UCN. Ce dispositif est appelé “spin flipper adiabatique”. Son fonctionnement est basé sur un passage adiabatique des neutrons à travers une résonance magnétique. Un champ magnétique radiofréquence B_1 est ajouté au champ magnétique statique de guidage de spin B_0 (en présence d'un gradient de champ). Le champ RF doit être orthogonal au champ de guidage, et sa fréquence doit être égale à la fréquence de précession de Larmor du champ de guidage en un point, qui sera appelé point de résonance. En ce point précis, le neutron voit un champ magnétique uniquement selon la direction du champ RF (dans le référentiel propre du neutron tournant à la même fréquence que le champ RF). Ainsi, en sortant de la zone de résonance, le spin du neutron a été inversé. Les étapes du processus de reversement de spin sont montrées sur la figure 3.2.

Le champ statique utilisé est le champ de fuite du polariseur (qui est dans la même direction que le guide neutron). Il faut donc ajouter une bobine qui génèrera un champ RF orthogonal au

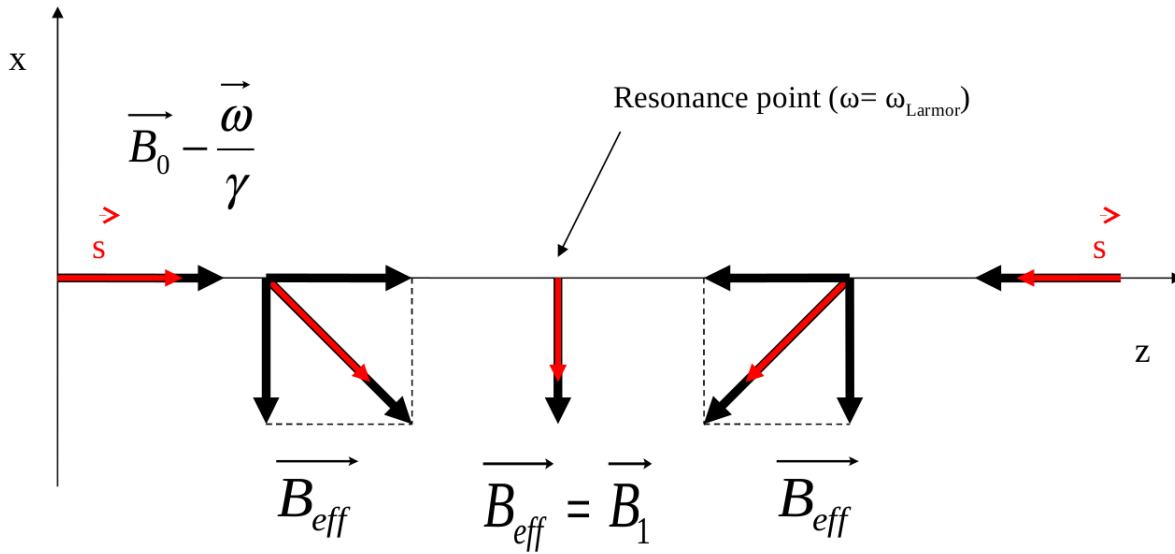


FIGURE 3.2 : Evolution du spin durant le processus de renversement de spin. Le champ magnétique B_0 est selon l'axe z , et le champ RF B_1 selon l'axe x .

guide. Des simulations RADIA ont été utilisées pour définir une géométrie convenable. La bobine RF est une paire de bobines rectangulaires placées en configuration de Helmholtz. L'efficacité du spin flipper fut déterminée à l'ILL avec des UCN. Elle est compatible avec 100 %. Plus de détails concernant l'élaboration et les tests du nouveau spin flipper sont donnés dans le chapitre 5 des annexes en anglais.

3.2 Simulations

Diverses simulations Monte-Carlo ont été faites dans le but de quantifier les dépolarisations ayant lieu dans l'appareillage OILL. Les deux principales sources de dépolarisation peuvent être dues aux inhomogénéités du champ magnétique ou aux collisions des UCN sur les parois des guides. Plus de détails concernant les simulations Monte-Carlo sont donnés dans le chapitre 4 des annexes en anglais.

3.2.1 Dépolarisations dues aux inhomogénéités du champ magnétique

Les dépolarisations dues aux inhomogénéités du champs magnétique ont lieu lorsque le critère d'adiabaticité n'est plus rempli. Le spin des neutron n'arrive plus "à suivre" les variations du champ magnétique, et il y a dépolarisation. La simulation s'est déroulée en deux temps. Des trajectoires d'UCN ont été simulées dans OILL en utilisant le code G4UCN. Puis les cartes champs simulées par MAENTOUCH et les trajectoires d'UCN ont été importés dans un code qui intègre les équations du spin (équations de Bloch) le long de la trajectoire des UCN. Le cas où des UCN de mauvais état de spin (càd non analysable) sont stockés au dessus de la feuille d'analyse a été considéré. La polarisation décroît avec le temps, jusqu'à atteindre une perte de 4 % à la fin d'un temps de stockage de 40 s.

3.2.2 Dépolarisations dues aux collisions

Les dépolarisations dues aux collisions sur les murs ont été estimées seulement en utilisant le code G4UCN. Un modèle probabiliste a été utilisé : à chaque matériau est associé une probabilité pour qu'un UCN soit dépolarisé lorsqu'il entre en contact avec le matériau. Les probabilités ont été précédemment déterminées expérimentalement. Des UCN ont été simulés lors des différentes phases d'un cycle de mesure (remplissage de la chambre, stockage, comptage). Il en résulte une dépolarisation inférieure à 1 % lors d'un cycle.

3.3 Mesures

La dernière partie de cette thèse présente les résultats expérimentaux obtenus avec l'appareillage OILL à PSI. La campagne de mesure a eu lieu en octobre 2011. Le chapitre 5 des annexes en anglais traite plus en détail cette partie.

3.3.1 Efficacité de polarisation et de maintien du spin

Le polariseur a été testé à l'aide de neutrons ultra-froid à PSI, lorsque la source a été opérationnelle. Cette mesure a utilisé le dispositif présenté sur la figure 3.3.

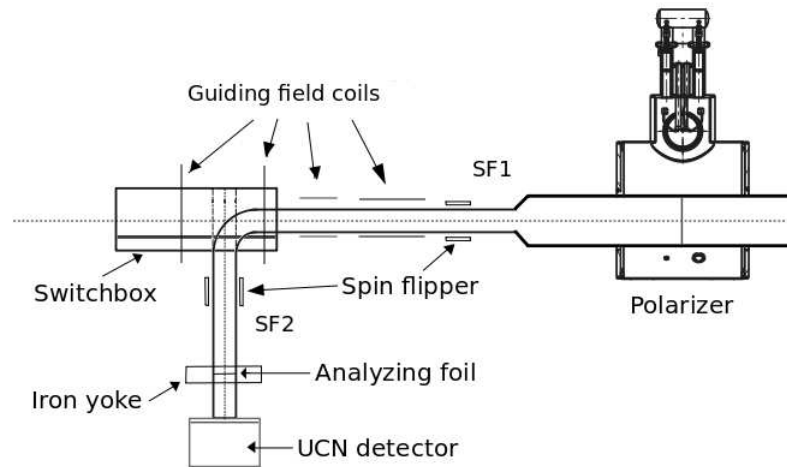


FIGURE 3.3 : Appareillage OILL en configuration pour la mesure d'efficacité de polarisation.

Deux mesures sont nécessaires pour déterminer l'efficacité : une mesure sans utilisation de spin flipper, et une avec un spin flipper allumé. Ainsi, il est possible de déterminer le pouvoir de polarisation-analyse, qui est :

$$A \times P = \frac{N_0 - N_1}{f \times N_0 + N_1} \quad (3.2)$$

où N_0 est le nombre de neutrons comptés avec le spin flipper éteint, N_1 le nombre de neutrons comptés avec le spin flipper allumé, et f est l'efficacité du spin flipper. Une efficacité de 88.5 ± 0.3 % a été mesurée.

f a été déterminé en utilisant une mesure similaire, mais nécessitant deux spin flipper.

$$\left\{ \begin{array}{l} f1 = \frac{N_{11} - N_{10}}{N_{00} - N_{01}} \\ f2 = \frac{N_{11} - N_{01}}{N_{00} - N_{10}} \end{array} \right. \quad (3.3)$$

$$(3.4)$$

avec N_{00} le nombre d'UCN comptés avec les deux spin flippers éteint, N_{10} le nombre d'UCN comptés avec le premier spin flipper allumé, N_{01} le nombre d'UCN comptés avec le second spin flipper allumé, et N_{11} le nombre d'UCN comptés avec les deux spin flippers allumés. Là encore, les efficacités de spin flip sont en accord avec 100 %.

3.3.2 Test des bobines de guidage

L'efficacité des bobines de guidage a été testée avec des UCN. Nous avons pu observer que l'utilisation de bobines additionnelles est nécessaire pour le maintien du spin, car l'asymétrie mesurée sans bobine de guidage est très faible (environ 30 %). Celle-ci est d'environ 73 % lorsque toutes les bobines de guidage sont alimentées. Néanmoins, une asymétrie identique a été obtenue en utilisant uniquement les bobines de guidage sur le guide horizontal et la bobine "UCN Kamin" qui se trouve à l'entrée du blindage. Cette configuration est donc suffisante pour un maintien du spin durant la mesure.

3.4 Resultats obtenus

Le nouveau système de polarisation a été installé et testé avec succès. Il fallait tout d'abord prouver l'efficacité d'un aimant supraconducteur en tant que polariseur d'UCN. Cette efficacité a été démontrée grâce à des simulation Monte-Carlo. L'aimant peut polariser prêt de 100% du faisceau, ce qui en fait un système de polarisation compétitif, l'efficacité du precedent système étant inferieur à 95%. Néanmoins, une cartographie magnétique a montré que des zones de champs faible existaient entre le polariseur et la chambre de precession. Ces zones peuvent dépolariser les UCN. Des bobines de guidage ont donc été concues et testées. Une simulation de precession de spin a montré que les inhomogénéités du champ entraînent une dépolarisation de moins de 4%. Une mesure expérimentale a néanmoins montré que la polarisation était maintenue même en ométant les bobines rectangulaires et saddle. Cela est due aux champs rémanent présent qui permettent un maintien adiabatique du spin des UCN même sans ces bobines de correction. Les simulations MC ont pour but de quantifier les dépolarisations dans le système expérimental. Il fallait vérifier que ces dépolarisation restaient "acceptable" pour une mesure du moment dipolaire électrique du neutron, soit une asymétrie finale compatible avec 95%. La valeur obtenue est de $94.4 \pm 1.6\%$. Enfin, les mesures expérimentales avaient pour but de vérifier l'efficacité du système de polarisation, ainsi que de comparaison avec les simulations. L'asymétrie mesurée expérimentalement est de $73.0 \pm 0.6\%$, soit environ 7% de moins que les valeur type obtenues lors de la phase I à l'ILL et 20% de moins que la valeur obtenue par simulations.

Conclusions

Ce travail de thèse avait pour but de fournir un nouveau système de polarisation et d'analyse de spin pour la phase II de la mesure du moment dipolaire électrique du neutron à PSI.

Un nouveau système de guidage de spin composé de sept bobines a été conçu et optimisé grâce à deux codes de simulation de champs magnétique. Pour cela, l'étude du paramètre d'adiabaticité k a été faite. Le nouveau système a été testé et installé avec succès sur l'appareillage OILL à PSI. Une estimation des dépolarisations due aux inhomogénéités du champs magnétique et due aux collisions sur les parois a été effectuée en utilisant un code de simulation Monte-Carlo. Les données expérimentales donnent des résultats en deçà des valeurs obtenues par la simulation. L'état de surface des matériaux utilisés est une explication possible de ce désaccord.

Le nouveau polariseur a été caractérisé via une cartographie de son champ magnétique. Il a été installé sur la ligne de neutrons ultra-froids et son efficacité a été mesuré avec l'efficacité de l'analyseur.

Un nouveau système de renversement de spin a aussi été conçu. Il utilise le champs de fuite du nouveau polariseur comme champ statique. Son efficacité a été mesuré et est compatible avec 100 %.

La valeur de l'efficacité de polarisation-analyse est au final en dessous de celle attendu. La cause probable de cette difference est une analyse inefficace de spin. Des mesures dédiées seront effectuées pour vérifier cette hypothèse.

Part II

Appendixes in english

Summary

The Standard Model (SM) describes the world of elementary particles and fundamental interactions. It is a coherent model in particles physics and is commonly used for 40 years. Nevertheless, it fails to explain the charge-parity (CP) symmetry violation required to explain the baryon asymmetry of the universe (BAU) [1]. Several extensions of the SM have been built in order to find new CP violation sources. A non-zero value of the intrinsic electric dipole moment (EDM) of a particle is a powerful test of these extensions [2]. EDM measurements are currently on going for several particles. The current upper limit on the neutron EDM is: $|d_n| < 2.9 \cdot 10^{-26} e \text{ cm}$ (90 % C.L) [3]. The European collaboration “nEDM” plans to reach the limit of 10^{-27} - $10^{-28} e \text{ cm}$. A new high density ultracold neutrons (UCN) source at the Paul Scherrer Institut (PSI) has been developed for this purpose. The project consists in three phases:

- the Phase I (2005-2008) has been completed at Institut Laue Langevin (ILL). The old spectrometer (OILL) which was used to determine the current best limit was improved. This phase was mainly an R & D phase, especially for the magnetometry system. Data has been taken at the end of 2008.
- the Phase II (2009-2014) takes currently place at PSI. The OILL apparatus was moved to PSI in March 2009 and was installed near the new source. Several systematic effects were measured, the R & D was pursued and the performances of the apparatus were tested. A limit of $10^{-27} e \text{ cm}$ should be reached at the end of this phase. In parallel, the design of a new spectrometer has been studied and started.
- the Phase III (2014-2016) will be at PSI. The new spectrometer will be used in order to reach the $10^{-28} e \text{ cm}$ limit.

The work developed in this thesis is mainly dedicated to the development, the tests and the optimization of a new polarizing-analyzing system.

The first chapter of this document gives the main motivations for the measurement of electric dipole moments. Furthermore, a summary of the properties of UCN is given. The second chapter is a description of the nEDM experiment. The measuring technique is explained and the

components of the OILL apparatus are described. The third chapter concerns the developments performed for the spin transport from the polarizer down to the detector. Magnetic field calculations using two simulation codes were carried out in order to design new guiding field coils. Then a magnetic field mapping was performed at PSI and compared to the simulations. The fourth chapter is devoted to depolarization and losses calculations. Depolarizations due to wall collisions and magnetic field inhomogeneities were estimated using Monte Carlo (MC) simulations and the integration of the Bloch equations. Furthermore, two characteristic times of the experiment (the storage time T_0 and the depolarization time T_1) were estimated, and compared to the measured ones. Finally, the last chapter deals with experimental study of the UCN polarization-analysis and the estimate of the apparatus performances with UCN.

CHAPTER

1

Electric dipole moments and ultracold neutrons

1.1 The Electric Dipole moment

1.1.1 Definition and motivations

EDM and the Standard Model

An electric dipole moment (EDM) can be defined when two identical and unlike charges $\pm q$ are located at a distance r from each other. Then $\vec{d} = q\vec{r}$. It may be observed in a system when the barycenter of the positive charges is separated from the barycenter of the negative charges. The EDM is measured when the system is placed in an electric field. The isolated system exists in a superposition of eigenstates. The degeneracy is removed when an electric field is applied. But an isolated particle may also have an EDM in a pure eigenstate. In quantum mechanics, Wigner-Ekarts theorem demonstrates that the EDM of an isolated particle must be aligned along its spin which is the only intrinsic vector of the particle. Then the EDM is: $\vec{d} = d\vec{S}$. The interaction between this EDM and the electric field reads:

$$H = -d\vec{E} \cdot \vec{S} \quad (1.1)$$

All particles with non zero spin can have an EDM.

In 1950, Purcel and Ramsey [6] suggested to use the EDM of the neutron as a test of parity violation. Applying the P and T operators on the Hamiltonian, we have:

$$H = -\vec{d} \cdot \vec{E} \xrightarrow{P} \vec{d} \cdot \vec{E}$$

and

$$H = -\vec{d} \cdot \vec{E} \xrightarrow{T} \vec{d} \cdot \vec{E}$$

Indeed, the P and T operators applied on \vec{E} and \vec{S} give:

$$\begin{array}{ll} \vec{E} \xrightarrow{P} -\vec{E} & \vec{S} \xrightarrow{P} \vec{S} \\ \vec{E} \xrightarrow{T} \vec{E} & \vec{S} \xrightarrow{T} -\vec{S} \end{array}$$

Both T and P are violated. Assuming the CPT theorem, the EDM violates CP since T is broken.

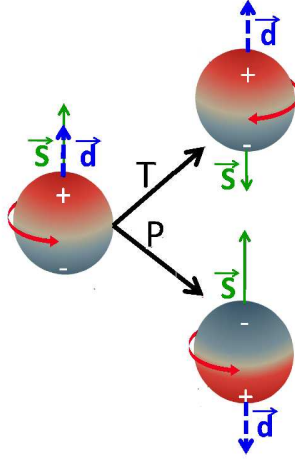


Figure 1.1: Scheme showing the CP and T violation of a particle with an electric dipole moment.

The search for a non zero EDM is motivated by new CP violation sources beyond the Standard Model. The two potentially CP violation sources within the SM are described below: one concerning the strong sector, the other one the electroweak sector [11].

In quantum chromodynamics, the interaction Lagrangian can be broken up in two parts: one concerning the interaction of quarks and gluons and a part relative to the non trivial vacuum structure of the theory [12] This second part can be written:

$$\mathcal{L}_\theta = -\frac{\theta}{16\pi^2} \text{Tr} \left[\tilde{F}_{\mu\nu} F^{\mu\nu} \right] \quad (1.2)$$

with $F_{\mu\nu}$ the gluon field strength tensor, and $\tilde{F}_{\mu\nu}$ its dual counterpart, defined by $\tilde{F}_{\mu\nu} = \frac{1}{2}\epsilon_{\mu\nu\alpha\beta}F^{\alpha\beta}$. The Lagrangian is also parameterized by the θ angle, which is a QCD phase called vacuum angle, and defined over $[0, 2\pi]$. From this angle the parameter $\bar{\theta}$ can be determined [13]. This parameter is naturally supposed to be close to unity. EDM of neutron is directly proportional to $\bar{\theta}$: we have $d_n \sim \bar{\theta} \times 2 \times 10^{-16} e \text{ cm}$ [14]. The current limit on d_n is $\sim 10^{-26} e \text{ cm}$ [3], constrains $\bar{\theta}$ to $\bar{\theta} \sim 10^{-10}$! This unexpected situation is known as "the strong CP problem" [15]. To solve this problem, Peccei and Quinn [16] bring into play a new particle: the axion, but this particle has not been observed yet.

Another CP violation source can be observed within the SM, in the electroweak sector. This source concerns the complex phase δ of the Cabibbo-Kobayashi-Maskawa matrix which describes the quarks mixing flavors.

The complex phase of the CKM matrix is related to the quarks EDM. Shabalin [17] has shown that there is no contribution to a quark EDM up to three loops. It can be demonstrated using the unitarity of the CKM matrix. The calculated quark EDM are: $d_d \sim d_u \sim 10^{-34} e \text{ cm}$. Another approach consists in using only a two quarks interaction (the third one being spectator) [18].

In this case, the two quarks interact weakly, and one loop is enough to create an EDM. Then, $d_d \sim d_u \sim 10^{-32} e \text{ cm}$. This is still 6 orders of magnitude below the current experimental limit (Fig. 1.3) It is not possible to experimentally test the CP violation which arises from the electroweak sector by a measurement of the neutron EDM, the next generation of experiments will not reach such a sensitivity.

EDM beyond the Standard Model

The Standard Model does not predict why the universe is made of matter. According to the Big Bang theory [19], at the beginning of the universe, both matter and antimatter annihilated and produced photons. But some matter has persisted and is the proof of an asymmetric situation. In 1967, Sakharov [1] has determined three conditions necessary to explain this asymmetry:

- laws governing matter and antimatter are different
- violation of baryon number
- deviation from the thermal equilibrium

The first point corresponds to CP violation. But the amount of CP violation in the Standard Model is not sufficient to explain the baryogenesis. In fact, there are 9 orders of magnitude between the theoretical and measured baryon to photon ratios [20]: $\eta_{exp} \sim 10^{-19}$ and $\eta_{theo} \sim 10^{-10}$. The Standard Model has extensions which can include new CP violation sources. Some extensions predict a value for the neutron EDM around $10^{-28} e \text{ cm}$. This limit is one order of magnitude from the current best experimental limit. Experiments can test these models. For example, in the minimal supersymmetric model (MSSM), there are two phases θ_A and θ_μ which violate CP [21, 22]. Electric dipole moments can be extracted from these phases and conversely the EDM constrains the phases.

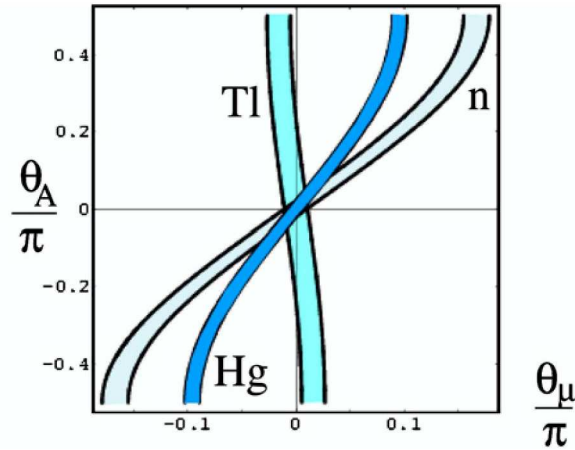


Figure 1.2: Constraints imposed by the neutron, thallium and mercury EDM on the two phases θ_A and θ_μ . Picture taken from [2]

Figure 1.2 shows the constraints from the neutron, thallium and mercury EDM on the two CP violating phases. These phases must be close to zero ($< 10^{-2}$). This is called the SUSY CP problem.

It is possible to measure EDM of atoms, as discussed in the next paragraph.

1.1.2 EDM of atoms

Two kinds of atoms can be defined in terms of their electronic outer layer: the paramagnetic atoms, and the diamagnetic atoms.

Paramagnetic atoms

Paramagnetic atoms have at least one single electron in the outer shell. In this configuration, the main contribution to the EDM comes from the electron EDM. This is due to the motion of the electrons. If the electrons were static, the Schiff's screening theorem [23] would predict a zero contribution from the single electron EDM. In fact, this theorem states that the electric charges of an atom are placed in a way that the external electric fields are canceled. Heavy atoms (high Z) with small angular momentum (J) and large polarizability (α , Sec. 1.2.2) are the ones with the largest EDM [2]. Indeed, we have :

$$d_{par} \sim \frac{10\alpha^2 Z^3}{J(J+1/2)(J+1)^2} d_e \quad (1.3)$$

The electron EDM can be extracted from the measurement of the EDM of these atoms. The current value: $d_e = (6.9 \pm 7.4) \times 10^{-28} e \text{ cm}$ comes from the measurement with the ^{205}Tl atom [24].

Diamagnetic atoms

In contrast to paramagnetic atoms, diamagnetic atoms do not have a single electron on the outer layer: their angular momentum is zero. The measurement of the atom EDM probes the nuclear EDM and the proton EDM can be extracted from this. The best limit on d_p comes from the measurement of ^{199}Hg EDM and is $d_p < 5.4 \times 10^{-24} e \text{ cm}$ [25].

1.1.3 The Neutron EDM

Since 1950 [5], the measured upper limit on d_n has been decreased by 6 orders of magnitude (Fig. 1.3). Physicists have used two kinds of neutrons: cold or very cold neutron beams and ultra-cold neutrons (Sec. 1.2) stored in a vessel. For the first type of experiment, the sensitivity is limited by the relativistic $v \times E$ effect [26]. Inside an electric field \vec{E} , a neutron with velocity \vec{v}_n experiences an effective magnetic field:

$$\vec{B} = \frac{\vec{E} \wedge \vec{v}_n}{c^2} \quad (1.4)$$

With a cold neutron mean velocity of 150 m.s^{-1} , the $v \times E$ gives a false EDM of $2 \cdot 10^{-24} e \text{ cm}$ [9]. For the second type of experiments, the neutron velocity is below 8 m.s^{-1} , which decreases the $v \times E$ systematic effect. Over the last 50 years, the neutron densities have continuously increased. This allowed the reduction of the statistical uncertainty leading to the upper limit $|d_n| < 2.9 \cdot 10^{-26} e \text{ cm}$ (90 % C.L.) [3]. This result was obtained with the apparatus we are using.

There is 6 collaborations around the world which try to improve the sensitivity on the upper limit on the neutron EDM. The expected schedules to reach new sensitivities for each of these experiments is given in Fig. 1.4.

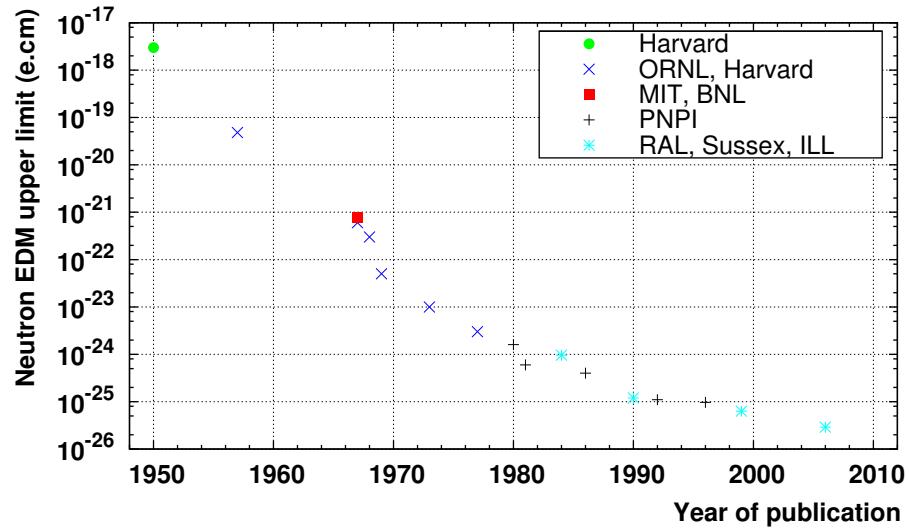


Figure 1.3: Evolution on the nEDM limit with time [3, 6, 8–10, 27–38].

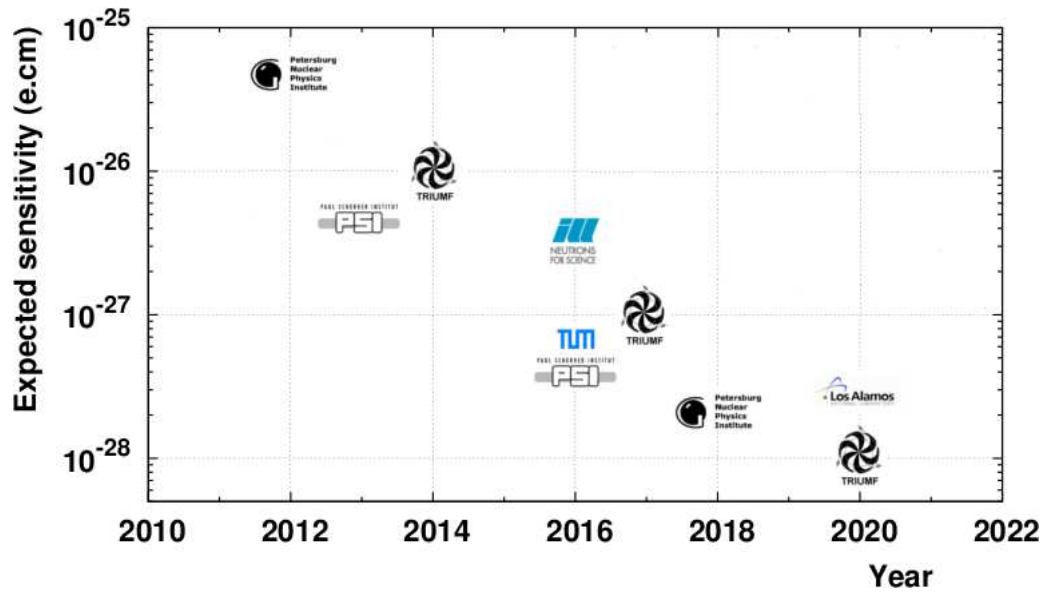


Figure 1.4: Expected reachable sensitivities for the six nEDM experiments: PNPI collaboration (ILL, Gatchina), nEDM collaboration (PSI), Japan-Canada collaboration (RCNP, TRIUMF), CryoEDM (ILL), Munich experiment (TUM) and US collaboration (LANL)

1.2 Ultracold neutrons

The neutron was discovered by Chadwick in 1932 while he was bombarding Beryllium with α particles [39]. It is only stable inside the nucleus and may be extracted using fission or spallation processes. As a free particle, it decays to a proton via the weak interaction with a rather long lifetime (Sec. 1.2.2). Because of their neutrality and their long lifetime, fast neutrons with an energy larger than 500 keV are commonly used to probe matter since they easily penetrate into it. Once moderated (via collisions on light nuclei), their wave behavior appears. The associated De Broglie wavelength is given by:

$$\lambda_n = \frac{h}{\sqrt{2m_n E}} \quad (1.5)$$

with E the neutron energy, m_n the neutron mass and h the Planck constant. When λ_n becomes larger than the distance between two atoms, neutron may be reflected by matter. This is because the neutron does not interact with a single nucleus but with a set of nuclei. This phenomenon was first formulated by Fermi in 1936 [40] and observed 10 years later [41]. A neutron with a kinetic energy E and an incidence angle θ will be reflected on a surface if:

$$\sin \theta \leq \sqrt{\frac{V_F}{E}} \quad (1.6)$$

where V_F is called Fermi potential. It is a characteristic of the material, and is defined as:

$$V_F = \frac{2\pi\hbar^2}{m_n} \sum_i N_i b_i \quad (1.7)$$

with N_i the atom density of element i and b_i the coherent scattering length of element i . This potential is really small: a few hundreds of neV at most.

1.2.1 Definition

In 1959, Zeldovich [42] suggested the existence of very slow neutrons that may be fully reflected from material surfaces and therefore trapped in vessels. In fact, Eq. (1.6), shows that $\theta \in [0, 2\pi]$ if $E < V_F$. Neutrons fulfilling this condition are called ultracold neutrons (UCN). Their energy is below 300 neV, corresponding to velocities below 8 m/s, or, to temperatures close to 3 mK: this is why they are called ultracold. The ability to be trapped makes the neutron a very interesting probe for fundamental physics: it can be stored, manipulated and studied during a time as long as its lifetime. The best limits on the neutron lifetime or neutron EDM come from measurements with trapped UCN [3, 43].

1.2.2 Interactions

Neutrons are affected by the four fundamental interactions. A very interesting property is that the typical energy associated to each force (except the weak force) have the same order of magnitude. Typical potential energies for three of the four interactions are listed in Table 1.1.

The potential energies corresponding to typical experimental apparatus dimensions, applied magnetic fields and coatings have the same order of magnitude as the kinetic energy of UCN.

Table 1.1: UCN and interaction strengths.

Interaction	Formulation	Energy
Gravitation	$m_n g h$	100 neV per meter
Strong	V_F	few 100 neV
EM	$\mu_n B$	60 neV per Tesla

Gravitational interaction

Like all massive particles, neutrons are sensitive to gravitation. The gravitational potential is given by:

$$V_g = m_n g h \quad (1.8)$$

This corresponds to about 100 neV per meter. A UCN with a kinetic energy of 300 neV cannot rise above 3 meters. This property is used in UCN monochromators [44] or in UCN detectors in order to increase their efficiency.

Strong interaction

Interaction with a nucleus

The interaction between UCN and nuclei (wall materials) is governed by the strong force. For the scattering process, the wave function of the neutron far from the interaction potential is written as:

$$\psi = \psi_{inc} + \psi_{scat} \sim e^{ikr} + f(\theta) \frac{e^{ikr}}{r} \quad (1.9)$$

The wave function is the sum of an incident plane wave function and a scattered spherical wave function weighted by the term $f(\theta)$ called the scattering amplitude. $f(\theta)$ depends on the interaction potential. The square of this term corresponds to the scattering cross section:

$$\frac{d\sigma}{d\Omega} = |f(\theta)|^2 \quad (1.10)$$

The interaction potential is much larger than the UCN energy, so perturbation theory cannot be used. To solve this problem, Fermi [40] used a pseudo-potential which describes the interaction:

$$V_F(\vec{r}) = \frac{2\pi\hbar^2}{m_n} b \delta^{(3)}(\vec{r}) \quad (1.11)$$

where b is directly proportional to the coherent scattering amplitude:

$$b = -\frac{m_n}{m^*} f(\theta) \quad (1.12)$$

with m^* the reduced mass of the system:

$$m^* = \frac{m_n m_{nucleus}}{m_n + m_{nucleus}} \quad (1.13)$$

This pseudo-potential is adapted if the scattering is calculated to first order Born approximation.

Interaction with a set of nuclei

UCN have a large wavelength compared to the atomic radius (50 to 130 nm compared to 0.1 nm). Therefore, during a scattering process, a UCN interacts with hundreds of nuclei. The mean potential, called the Fermi potential, is given in Eq. (1.7). A critical velocity can be defined from this potential:

$$v_c = \sqrt{2V_F/m_n} \quad (1.14)$$

Table 1.2 shows several common materials with their Fermi potential and associated critical velocity.

Table 1.2: Fermi potentials, critical velocities and losses factor (Sec. 1.2.2) of materials used in UCN physics.

Material	V_F [neV]	v_c [m/s]	W [neV]
Al	54	3.2	$1.1 \cdot 10^{-3}$
Be	252	6.9	$1.3 \cdot 10^{-3}$
C (graphite)	195	6.1	$1 \cdot 10^{-3}$
C (diamond)	306	7.7	$3.1 \cdot 10^{-5}$
Cu	168	5.7	$2.5 \cdot 10^{-2}$
DPS	162	5.6	$3.8 \cdot 10^{-2}$
Fe	210	6.3	$1.9 \cdot 10^{-2}$
Ni (natural)	252	6.9	$3.2 \cdot 10^{-2}$
^{58}Ni	335	8	$3 \cdot 10^{-2}$
Quartz	90	4.1	$3.6 \cdot 10^{-4}$
Stainless steel	185	5.9	$1.5 \cdot 10^{-2}$

The arrival of a neutron on a surface may be described as the arrival of a neutron on a potential step. The neutron energy can be divided in two parts: one perpendicular to the surface (E_\perp), and one parallel to it (E_\parallel). Classically, the neutron is transmitted if $E_\perp > E_c$, and reflected if $E_\perp < E_c$. In a quantum approach, it is not the case anymore. Let us consider a one dimensional problem: the potential step can be described as:

$$V(x) = \begin{cases} 0 & x < 0 \\ V & x > 0 \text{ with } V > 0 \end{cases} \quad (1.15)$$

Figure 1.5 shows this potential and the three waves.

If the UCN energy is written E_\perp , then the UCN wave function is:

$$\psi = \begin{cases} Ae^{ik_x x} + rAe^{-ik_x x} & x < 0 \\ tAe^{ik_t x} & x > 0 \end{cases} \quad (1.16)$$

with $k_x = \sqrt{\frac{2m_n}{\hbar^2} E_\perp}$, $k_t = \sqrt{\frac{2m_n}{\hbar^2} (E_\perp - V)}$, rA being the amplitude of the reflected wave and tA the amplitude of the transmitted wave. Using the continuity conditions, the probability of reflection $R = r^2$ and transmission $T = \frac{k_t}{k_x} t^2$ are calculated:

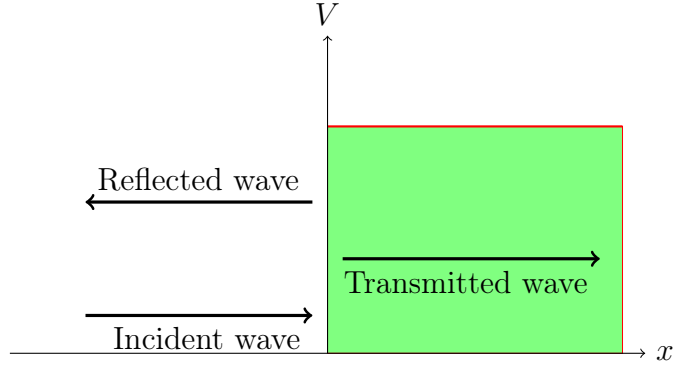


Figure 1.5: Potential step with incident, transmitted and reflected waves.

$$R = 1 - T = \left(\frac{1 - \sqrt{1 - V/E_{\perp}}}{1 + \sqrt{1 - V/E_{\perp}}} \right)^2 \quad (1.17)$$

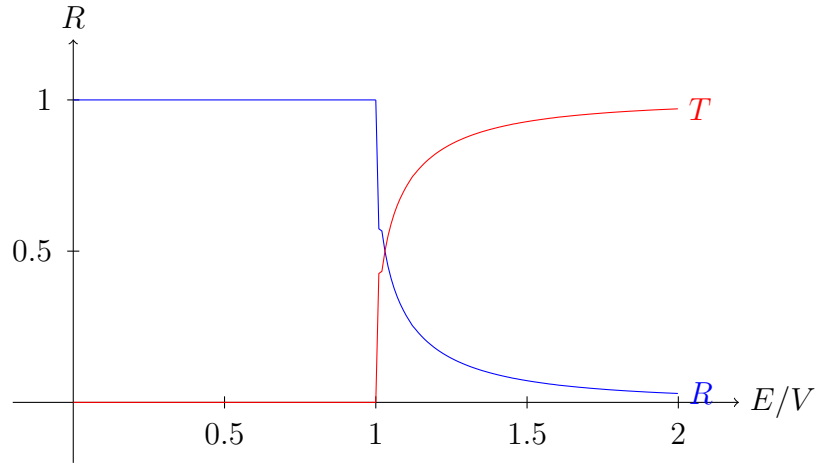


Figure 1.6: Reflection and transmission coefficients for a UCN incident with a perpendicular energy E upon a Fermi potential V .

If $E_{\perp} < V$, k_t is not real and the wave function penetrates shortly the potential wall. During the penetration, the UCN may be lost. An imaginary part is added to the potential to account for that: $V_F = V - iW$. The loss time is directly proportional to W : $1/\tau_{loss} = 2W/\hbar$ [45]. Furthermore, this loss time can be expressed using the loss cross section (including the losses due to absorption and due to inelastic up-scattering): $1/\tau_{loss} = Nv\sigma_{loss}$ with N the material atomic density, v the UCN velocity and σ_{loss} the total losses cross section. Then the Fermi potential is:

$$V_F = V - iW = N\hbar \left(\frac{2\pi\hbar}{m_n} b - \frac{i}{2} v\sigma_{loss} \right) \quad (1.18)$$

Using the fact that $W \ll V$ (Table 1.2), the probability of reflection R is:

$$R = 1 - 2\frac{W}{V}\sqrt{\frac{E_{\perp}}{V - E_{\perp}}} = 1 - \mu(E_{\perp}) \quad (1.19)$$

where $\mu(E_{\perp})$ is the wall loss probability per bounce. This probability increases if the incident energy is close to V .

Weak interaction

The β^- decay of the free neutron is governed by the weak interaction via the reaction:

$$n \rightarrow p + e^- + \bar{\nu}_e \quad (1.20)$$

In that case, a d quark is changed in a u quark with a W^- boson emission. It is shown in Fig. 1.7.

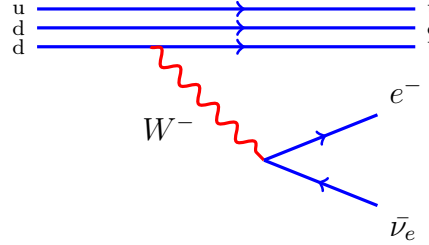


Figure 1.7: Feynman diagram of the neutron beta decay. A down quark turns to a up quark with an emission of a W^- boson, which disintegrates into an electron plus an antineutrino.

Electromagnetic interaction

Interaction with a magnetic field

Due to its magnetic moment $\mu_n = -9.6623641(23) \cdot 10^{-27}$ J/T [46], the neutron interacts with magnetic fields. The magnetic potential energy is defined as:

$$V_m = -\vec{\mu}_n \cdot \vec{B} \quad (1.21)$$

In term of Pauli matrices $\vec{\sigma}$, the potential energy can be rewritten:

$$V_m = -\gamma_n \frac{\hbar}{2} \vec{\sigma} \cdot \vec{B} \quad (1.22)$$

where $\gamma_n = 2\mu_n/\hbar$ is the gyromagnetic ratio of the neutron. There is a direct coupling between the magnetic field and the spin of the neutron. Indeed, the magnetic field exerts a torque on the spin:

$$\vec{\Gamma} = \gamma_n \vec{S} \times \vec{B} \quad (1.23)$$

This torque leads to the evolution of the spin with time:

$$\frac{d\vec{S}}{dt} = \gamma_n \vec{S} \times \vec{B} \quad (1.24)$$

The spin precesses around the magnetic field direction with an angular frequency $\omega_L = \gamma_n B$. It is called Larmor frequency. The measurement of the corresponding Larmor precession frequency is also the cornerstone of the nEDM experiment, which is based on the measurement of a shift of this Larmor frequency depending on the relative orientation of the electric and magnetic fields (Chap. 2).

Equations (1.24) describe spin evolution in the presence of a magnetic field and are called Bloch equations [47]. They are classical equations, in opposition to the time dependent Schrödinger equation which can also describes the spin motion in quantum mechanics, but lead to the same results. Bloch equations will be treated in different ways in the next chapters of this thesis. The rewriting of the Bloch equations in the frame rotating with the neutron spin will lead to the adiabaticity parameter (Chap. 3) and to the operating principle of spin flipper devices (Chap. 5). They will also be integrated numerically (Chap. 4). Furthermore, depolarization terms can be added to the Bloch equations to take relaxation processes into account. Two characteristic times are added: T_1 is the longitudinal relaxation time, and T_2 is the transverse relaxation time:

$$\begin{aligned} \frac{dS_x}{dt} &= \gamma(\vec{S} \times \vec{B})_x - \frac{S_x}{T_2} \\ \frac{dS_y}{dt} &= \gamma(\vec{S} \times \vec{B})_y - \frac{S_y}{T_2} \\ \frac{dS_z}{dt} &= \gamma(\vec{S} \times \vec{B})_z - \frac{S_z - S_0}{T_1} \end{aligned}$$

where S_0 is asymptotic value of S_z in time. The two relaxation times T_1 and T_2 are limiting times for the nEDM measurement. The longitudinal time will be calculated (Chap. 4) and also measured (Chap. 5).

One can build a model in which the effective potential experienced by the neutron is spin dependent. In the presence of a material and a magnetic field, the potential seen by the UCN is the addition of the Fermi pseudo potential and the magnetic potential:

$$V = V_F + V_m = \frac{2\pi\hbar^2}{m_n} N b \mp \mu_n B \quad (1.25)$$

For a ferromagnetic element, V_F and V_m , have a comparable magnitude (V_F is some hundreds of neV, and V_m corresponds to about 60 neV.T⁻¹). If $V_F \leq V_m$, a neutron with a spin antiparallel to the magnetic field will experience a zero or negative potential (all such spin state neutrons are passing through the element), and the neutrons with a spin parallel to the magnetic field will experience a positive potential wall. This phenomenon is depicted in Fig. 1.8. By this effect, it is possible to polarize UCN [48].

In the presence of an inhomogeneous magnetic field, the force exerted on the UCN is:

$$\vec{F}_m = -\text{grad}(V_m) \quad (1.26)$$

This force is also spin dependent, the gradient is acting as in a Stern and Gerlach experiment. Polarization can be obtained using a high magnetic field [49].

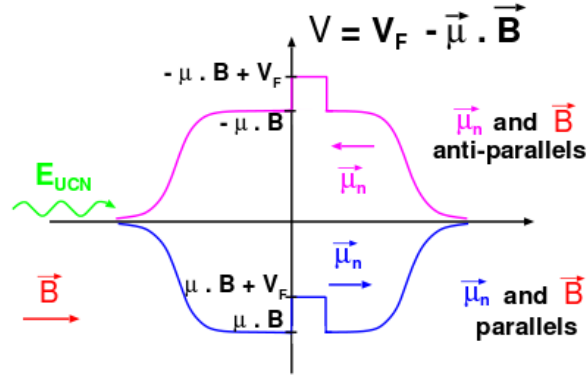


Figure 1.8: Principle of the polarization using a magnetic field. The potential experienced by the neutron depends on its spin (spin and magnetic moment of the neutron are anti-aligned).

Interaction with an electric field

Neutrons have an electric internal distribution because of its quark structure. Assuming a charge density $\rho(\vec{r})$, the neutron electric charge can be written:

$$q_n = \int \rho(\vec{r}) d\vec{r} \quad (1.27)$$

The non zero value of the neutron charge is a direct test of charge conservation. Indeed, if q_n is different from zero, then the neutron anti-neutron oscillation is not allowed. At present, the neutron charge limit is [50]:

$$q_n = (-0.4 \pm 1.1) \times 10^{-21} q_e \text{ (68 \% c.l.)} \quad (1.28)$$

Several experiments are aiming at decreasing this limit in the next years [51, 52].

The second effect of the electric internal structure is the existence of the neutron EDM (Chap. 2). Added to this EDM, an induced EDM can also be created if the neutron is placed inside an electric field. It is directly proportional to E:

$$d_n = 4\pi\epsilon_0\alpha_n E \quad (1.29)$$

The α_n term is called the neutron polarizability. Using lattice QCD, a theoretical value is $\alpha_n = 3.8 \times 10^{-4} \text{ fm}^3$ [53]. The most recently measured value of α_n is three times larger: $\alpha_n = 12.5 \pm 1.8 \text{ (stat)}^{+1.1}_{-0.6} \text{ (syst)} \pm 1.1 \text{ (model)} \times 10^{-4} \text{ fm}^3$ [54]. The induced EDM created by the electric field of our experiment will be $d_n = 1.1 \times 10^{-32} e \text{ cm}$, which is five orders of magnitude below the expected sensitivity of the experiment (Chap. 2).

1.2.3 Production

Neutrons may be produced with two different techniques: either using the fission reaction (as in the ILL nuclear reactor), or using spallation process (as at PSI). The liberated neutrons are decelerated to UCN velocity by several steps. A moderator is placed close to the neutrons production location. They are thermalized by elastic collision with the nuclei of the moderator. When the thermal equilibrium is reached with the nuclei of the moderator, the neutrons velocity

distribution is close to a Maxwellian distribution. Few of these neutrons are UCN (Fig. 1.9). In order to increase the UCN density, neutrons are cooled down. Neutrons are first down scattered in a suitable material (typically heavy water) to reach the thermal level ($T=300$ K), then a colder moderator (some tens of K) is used to reach the cold level. The Ultracold state is reached by using a very cold moderator (T is a few K). At this temperature, the energy is transferred from cold neutrons (CN) to material via phonon excitation [55]. Another possible moderator to obtain a high UCN density is the superfluid Helium [56]. With a 8.9 Å cold neutron beam, the energy of neutrons is converted to the one of a phonon [57]. Theoretically, it is possible to reach several millions of UCN per cm^3 . Experimentally, some 10000 UCN per cm^3 are expected. Table 1.3 shows the present and future UCN sources in the world.

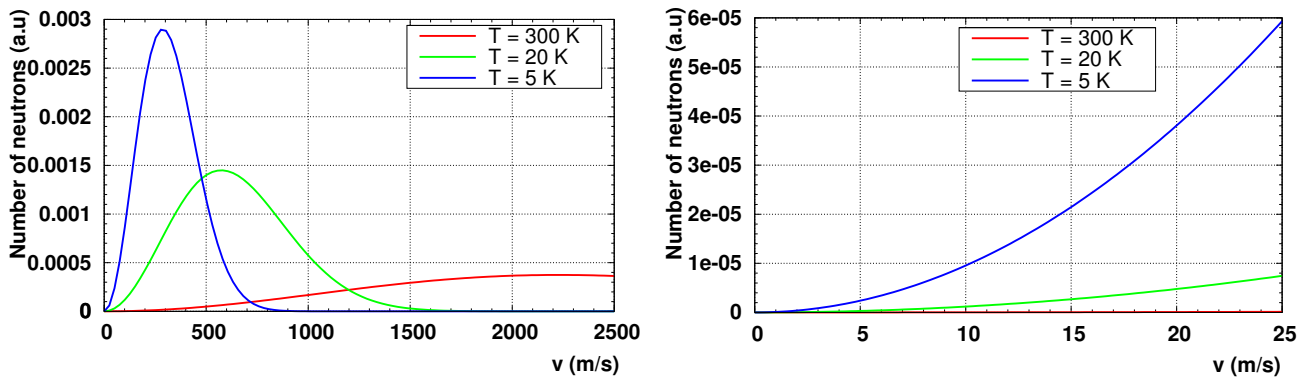


Figure 1.9: Velocity distributions for 300 K neutrons (D_2O moderator), 20 K neutrons (L D_2 moderator) and 5 K neutrons (S D_2 moderator). A minimal part of the distribution are UCN, even with a very cold moderator (about 10^{-11} for 300 K, 10^{-9} for 20 K and 10^{-8} for 5 K).

Table 1.3: Summary of UCN sources around the world.

Location	Neutron source	Moderator	UCN density (cm^{-3})	status
PSI (Switzerland)	spallation	SD_2	1000	working
ILL (France)	reactor	LD_2	50	working
TRIGA (Germany)	reactor	SD_2	10	working
FRM-II (Germany)	reactor	SD_2	10000	2012
TRIUMF (Canada)	spallation	superfluid He	5800	2016
RCNP (Japan)	spallation	superfluid He	15	working
PNPI (Russia)	reactor	SD_2	10000	2014
SNS (USA)	spallation	superfluid He	150	working
LANL (USA)	spallation	SD_2	30	working

The PSI UCN source

At PSI, neutrons are generated by spallation: a high intensity proton beam (2 mA, 600 MeV, [58]) strikes a lead target as shown in Fig. 1.10. The PSI UCN source is using this superthermal

conversion with a solid deuterium moderator: extracted neutrons are thermalized in a 3 m³ heavy water tank, then a solid deuterium converter (30 L) scatters neutrons down to UCN energy. The upward scattered neutrons are stored in a 1.6 m³ DLC coated storage volume [59]. Then the UCN are guided to the experimental area through NiMo coated glass tubes. A 1000 UCN/cm³ density is expected at the exit of the storage volume.

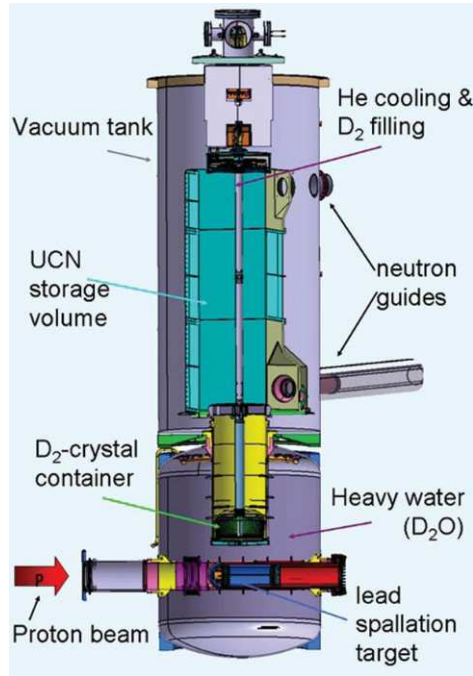


Figure 1.10: The PSI UCN source.

CHAPTER

2

The nEDM experiment

This chapter focuses on the technique used for the measurement of the neutron electric dipole moment. The first part is dedicated to the principle of the neutron EDM measurement. The second part, to the OILL spectrometer used for the nEDM determination, stressing on the new components of the system.

2.1 Principle of the nEDM measurement

In the presence of an electric field, the interaction term of the neutron EDM \vec{d}_n with an external electric field \vec{E} reads:

$$\hat{H} = -\hat{\vec{d}}_n \cdot \vec{E} \quad (2.1)$$

The coupling of the EDM with an electric field is analogous to the coupling of a magnetic dipole moment(MDM) $\vec{\mu}_n$ with a magnetic field \vec{B} :

$$\hat{H} = -\hat{\vec{\mu}}_n \cdot \vec{B} \quad (2.2)$$

The two contributions are naturally added in the presence of a magnetic and electric fields:

$$\hat{H} = -\hat{\vec{d}}_n \cdot \vec{E} - \hat{\vec{\mu}}_n \cdot \vec{B} \quad (2.3)$$

Figure 2.1 shows the splitting in energy of the neutron when it is subjected to a magnetic and an electric field.

The strategy to measure the $\vec{d}_n \cdot \vec{E}$ contribution is to use a very homogeneous magnetic field \vec{B} and a high electric field \vec{E} . With the values used at PSI ($B_0=1 \mu$ T and $E=10$ kV·cm⁻¹), and the currently known values and limit of the MDM and EDM ($\mu_n=-0.966 \times 10^{-26}$ J·T⁻¹ and $d_n < 4.8 \times 10^{-47}$ C·m), we still have:

$$\frac{\mu_n \cdot B}{d_n \cdot E} > 1.7 \times 10^9 \quad (2.4)$$

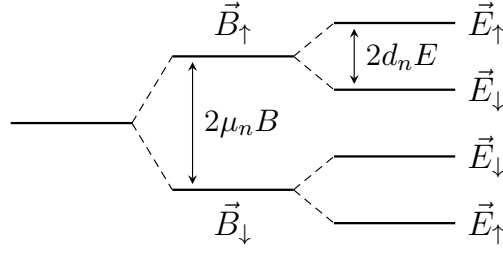


Figure 2.1: Energy levels of a neutron in the presence of collinear magnetic and electric fields.

This means that $\vec{\mu}_n \cdot \vec{B}$ has to be determined very accurately. For an accurate measurement, B has to be as homogeneous as possible within the experiment vessel, to decrease some magnetic field dependent systematic effects. The aim of the experiment is to reach a relative homogeneity $\Delta B/B$ of 10^{-5} within the storage volume per cycle. A high electric field is also needed. Having a large electric field between the two electrodes leads to a larger contribution of the EDM - electric field interaction in the Hamiltonian, but also to larger electric field dependent systematic effects, in addition to technical problems (creation of sparks). The most precise way so far to measure the EDM is to measure the precession frequency of the UCN in the presence of \vec{E} and \vec{B} fields. The Hamiltonian can be rewritten as a function of the precession frequency: $H = \hbar\omega_n/2$. This precession frequency is measured with two different fields configurations: with magnetic and electric fields parallels ($\uparrow\uparrow$) or anti-parallel ($\uparrow\downarrow$). According to Fig. 2.1, we have:

$$\hbar(\omega_{n\uparrow\uparrow} - \omega_{n\uparrow\downarrow}) = 2\mu_n(B_{\uparrow\uparrow} - B_{\uparrow\downarrow}) + 2d_n(E_{\uparrow\uparrow} - E_{\uparrow\downarrow}) \quad (2.5)$$

where we have $B_{\uparrow\uparrow} = B_{\uparrow\downarrow}$ and $E_{\uparrow\uparrow} = -E_{\uparrow\downarrow}$, then the EDM is directly proportional to the difference of the Larmor frequencies:

$$d_n = -\frac{\hbar}{4E}(\omega_{n\uparrow\uparrow} - \omega_{n\uparrow\downarrow}) \quad (2.6)$$

A sensitive way to measure the neutron precession frequency is with the Ramsey separated oscillatory field method [5]. This method was initially designed for atomic physics but is also very powerful with neutrons. This method was developed in 1950 and has been used up to now.

2.1.1 The Ramsey separated oscillatory field method

The initial population of neutrons is polarized along a static magnetic field B_0 (chosen as the z direction). Then a radiofrequency magnetic field pulse is applied for a suitable duration. This rotates the neutron spin in the plane orthogonal to the B_0 field (xy plane). The pulse is called “ $\pi/2$ ” because it turns the spin by $\pi/2$ rad. At the end of the pulse, the particles are precessing in the xy plane during the precession time T (≈ 150 s in our application). If the nEDM exists, a phase shift appears during the precession time which leads to a frequency shift. Finally, a second identical $\pi/2$ pulse is applied. It places the spin collinear to the static field axis (anti-parallel to B_0). The two $\pi/2$ pulses are producing a π flip only if the frequency of the two pulses correspond to resonance frequency $\omega = \omega_0$. It is possible to determine the resonance frequency by tuning the RF frequency of the two pulses. The resonance is determined by counting the two spin states populations of neutrons.

2.1.2 Application to the nEDM experiment

In the case of the nEDM measurement, a $12 \text{ kV}\cdot\text{cm}^{-1}$ electric field is added to the magnetic field during the whole cycle. This leads to a shift of the resonance frequency if the neutron EDM differs from zero (Eq. (2.6)). With the current limit on EDM and the applied electric field, such a frequency shift is lower than 10^{-7} Hz . The frequency shift between the RF frequency and the resonance frequency $\Delta\omega = \omega - \omega_0$ leads to a phase shift $\Delta\phi = \Delta\omega T$ (T is the precession time defined in the previous section). Four measurements are performed to measure the resonance frequency. For each measurement, both UCN spin states are measured. For instance, the number of spin up states as a function of the RF frequency is shown in Fig. 2.2. The minimum of counts

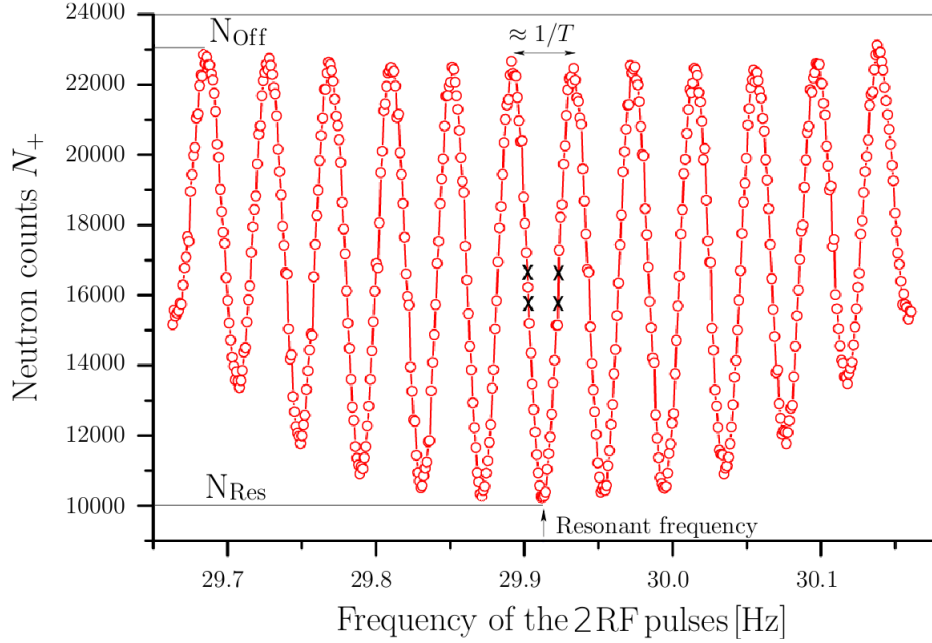


Figure 2.2: Ramsey Curve measured by the Sussex/RAL/ILL collaboration, and taken from [60].

is measured at the resonance frequency. The number of counts for the spin up (N_+) or spin down (N_-) states depends on the frequency shift $\Delta\omega$ [44]:

$$N_{\pm}(\Delta\phi) = \frac{N_+ + N_-}{2} (1 \mp \alpha \cos(\Delta\phi)) = \frac{N_+ + N_-}{2} (1 \mp \alpha \cos(\Delta\omega T)) \quad (2.7)$$

where α is the visibility of the central resonance fringe. It is a quality factor related to the polarization and spin analysis and it is defined as:

$$\alpha = \frac{N_{Off} - N_{Res}}{N_{Off} + N_{Res}} \quad (2.8)$$

N_{Off} is the maximum number of neutrons measured far from the resonance region and N_{Res} the minimum value at the resonance (Fig. 2.2). From $N_+ - N_-$, one can extract the frequency shift:

$$\Delta\omega = \frac{\arccos\left(\frac{N_- - N_+}{\alpha(N_+ + N_-)}\right)}{T} \approx \frac{\pi}{2T} - \frac{N_- - N_+}{\alpha T(N_+ + N_-)} \quad (2.9)$$

If the neutron EDM exists, $N_+ - N_-$ is different when the two fields are parallel ($\uparrow\uparrow$) with respect to the antiparallel field configuration ($\uparrow\downarrow$). Assuming that the precession time, the visibility and the number of neutrons are the same for the two field configurations, the electric dipole moment as a function of the number of UCN is:

$$d_n = -\frac{\hbar(\Delta N_{\uparrow\uparrow} - \Delta N_{\uparrow\downarrow})}{4\alpha T E N_0} \quad (2.10)$$

where $N_0 = N_+ + N_-$ and $\Delta N = N_+ - N_-$. From this formula, the statistical uncertainty can be derived:

$$\sigma_{d_n} = \frac{\hbar}{2\alpha T E \sqrt{N_0}} \quad (2.11)$$

As expected the statistical uncertainty depends on the number of neutrons N , but also on the strength of the electric field E , the precession time T and the visibility α . The used electric field will be 12 kV/cm. The precession time was optimized to 150 s, it has to be as large as possible to decrease the statistical uncertainty, but not too long in order to avoid UCN depolarizations and losses in the chamber which decrease either α and N_0 . Thanks to the new UCN source, a value of $N_0 = 350000$ is expected. Finally, the visibility has to be as large as possible, the requirement is $\alpha = 0.7$ after 150 s of free precession. This would be achievable with a new polarizer (Chap. 5). With these requirements, a statistical sensitivity of $\sigma_{d_n} = 4 \times 10^{-25} e$ cm per cycle, and $\sigma_{d_n} = 3 \times 10^{-27} e$ cm per year of measurement is expected. Systematic errors must also be taken into account to reach the expected sensitivity. For phase II at PSI, the overall systematic error has to be at the same order of magnitude as the statistical error and is expected to be $1.3 \cdot 10^{-27} e$ cm [61].

2.2 The nEDM apparatus at PSI

The experimental setup used by the nEDM collaboration at PSI has been built 20 years ago by the Sussex/RAL/ILL collaboration [3]. It has been already used for 4 years (2005-2009) at ILL and will be operating up to 2013-2015 at PSI. The current best limit on the neutron EDM has been measured with it [3]. Several pieces have been upgraded since 2005. This section provides a description of the upgraded OILL apparatus.

2.2.1 Overview

Figure 2.3 shows a global scheme of the OILL spectrometer (June 2011). Ultracold neutrons are coming from the PSI UCN source inside a 180 mm guide and arrive in the warm bore of the superconducting polarizer magnet. The polarized ultracold neutrons enter the precession chamber where there are stored. The electric field is applied. ^{199}Hg atoms are injected in the same storage vessel as the UCN (they are called co-magnetometer) in order to measure the magnetic field, and the $\pi/2$ RF pulses are applied. Then the spin of the UCN and mercury atoms precess during the precession time T . A second set of $\pi/2$ pulses are applied and the precession chamber is opened. The UCN fall to the analyzer foil. Both spin states are counted using a glass scintillator detector.

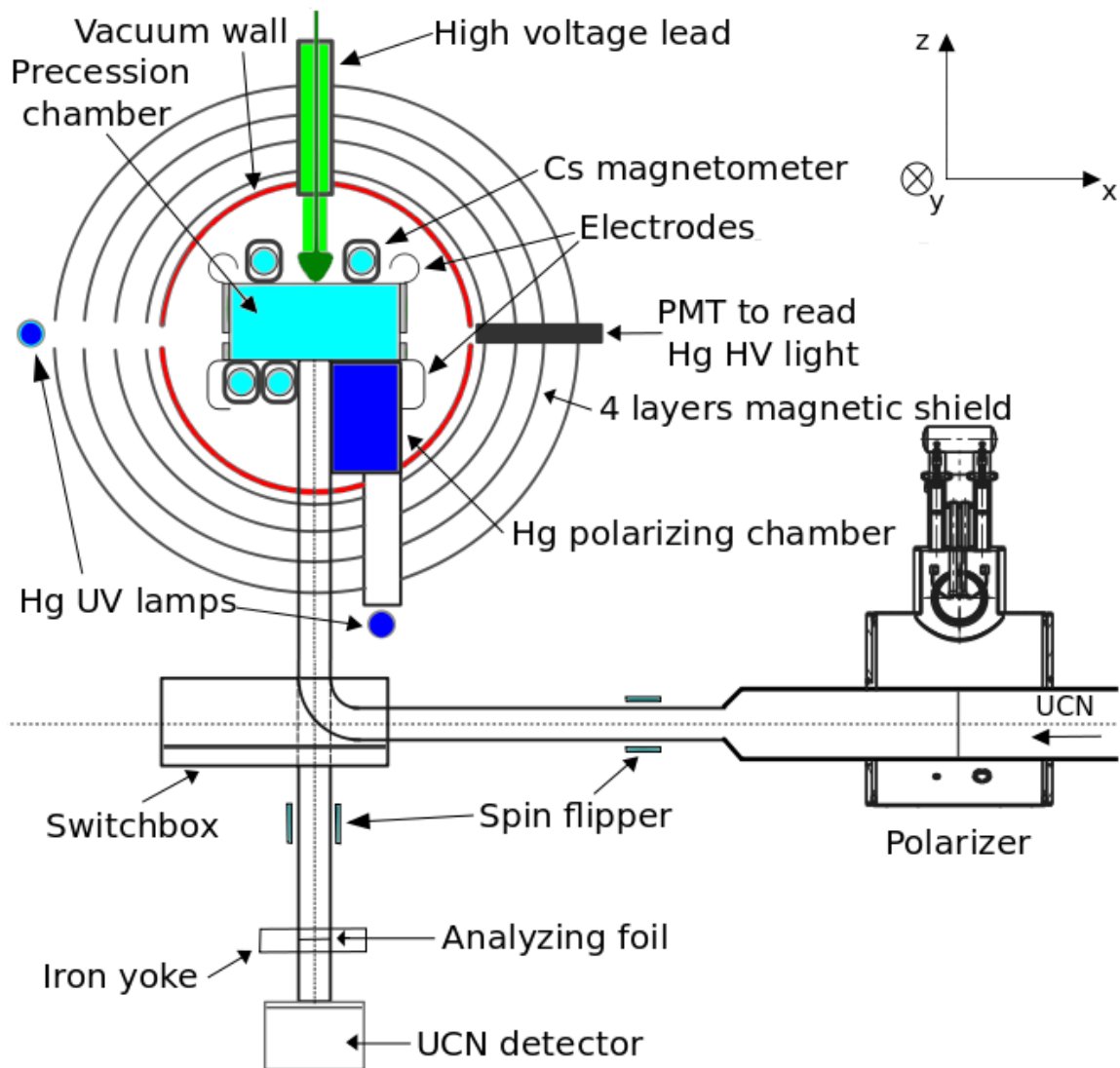


Figure 2.3: A global scheme of the OILL apparatus at PSI. More details are given in the text.

2.2.2 UCN transport

polarizer - analyzer - spin flippers

The polarizer is a superconducting solenoid with a warm bore. It creates a 5T axial field at the center, which allows a 100 % polarization for UCN with an axial velocity lower than 7.6 m.s^{-1} . The use of a superconducting solenoid as a polarizer for UCN is explained in Ref. [49]. The polarizer rejects half of the UCN beam intensity: the wrong spin state UCN go back to the UCN tank. In any case, the wrong spin state UCN cannot go through the polarizer unless the spin state changes. In order to do so, a radio-frequency spin flipper upstream from the SC magnet was setup. Calculations have shown that 25 % of the rejected UCN have their spin flipped and therefore can pass through the magnetic barrier [62]. Two other spin flippers have been setup in the experiment. The first one located just after the SC magnet, allows the selection of the UCN spin state stored in the chamber (the SC magnet can only select one spin state). The second spin flipper is placed above the analyzing foil. It allows counting both UCN spin states. The foil is made of an aluminum substrate with a thickness of $25 \mu\text{m}$ and an iron coating of 400 nm. The foil is magnetized with permanent magnets, which produces a 90 mT magnetic field at the center. As a result, the iron layer is magnetized close to saturation, *i.e.* close to 2 T. This creates a potential barrier which depends on the UCN spin state: for a magnetic field of 2 T, the potential barrier is 89 neV for one spin state, and 330 neV for the other spin state). The SC magnet is described in Chap. 5.

UCN guides

The ultracold neutron guides have two different diameters. The guides from the UCN source to the polarizer have an inner diameter of 180 mm. The diameter is 73 mm downstream from the polarizer, the diameter has been reduced in order to pass through the magnetic shield. The guides are made of borosilicate glass coated with a mixture of nickel and molybdenum (85 % Ni, 15 % Mo). With such coated glass tubes, the roughness can drop below 10 nm. Their transmission has been measured to be above 99 % [63], compared to about 80 % for stainless steel guides [64]. Furthermore, the glass tubes do not affect radio frequency magnetic fields, this allows the use of RF spin flippers.

UCN switch

In order to be able to perform the filling, the emptying and the monitoring of the UCN beam, a switch box has been built. It consists in a rotating plate (Fig. 2.4), on which four guide tubes are fixed. Five positions are available (the numbers are shown in the left panel of Fig. 2.4):

1. a stainless steel bent tube allows the filling of the precession chamber. It connects the horizontal guide to the vertical guide (going to the precession chamber). A small hole in this tube is used to perform monitoring during the filling.
2. a bent tube allows the emptying of the horizontal guide. This position is used when the UCN are precessing in the chamber, the UCN in the horizontal guide are counted during this period, and allow a monitoring of the incoming UCN flux.
3. a vertical guide allows the emptying of the precession chamber to the detector.

4. an horizontal guide which is used for the test beamline.
5. a vertical hole used to pump the precession chamber.

The rotating system is controlled by non magnetic piezo-motors. The positioning accuracy of the guides is less than 0.1 mm. Each tube is coated with NiMo as for the UCN guides.

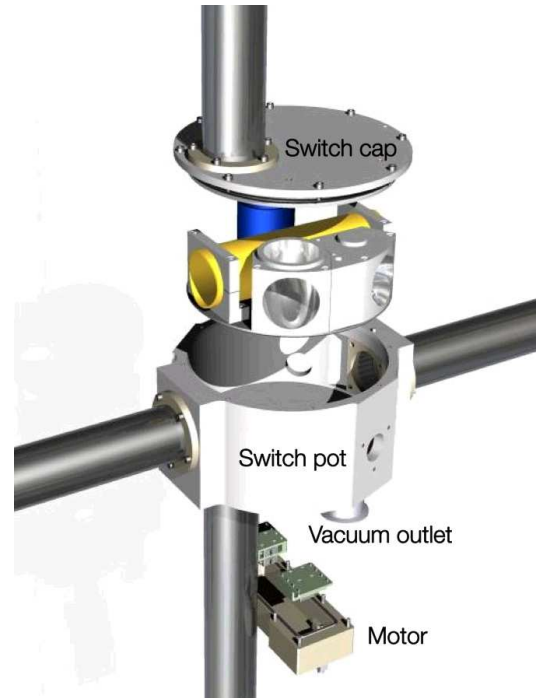
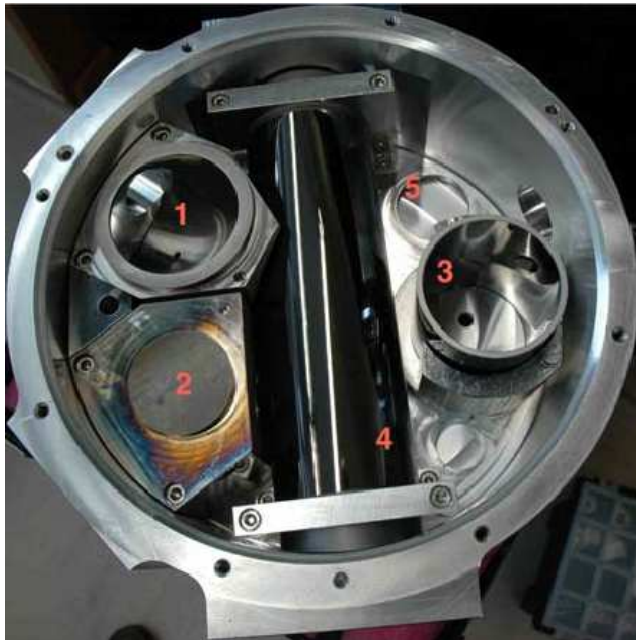


Figure 2.4: Left panel: Photo of the rotating plate with the inner guides. Right panel: Exploded drawing of the switch design.

Precession chamber

The precession chamber is the vessel where the UCN are freely precessing during the application of the electric field. The mercury co-magnetometer is also stored in the chamber. The chamber is a 470 mm diameter and 120 mm height cylinder.

It is made of two parts: two horizontal plates (the electrodes) and a vertical hollow cylinder (the insulator ring). Both electrodes are made of Aluminium coated with Diamond Like Carbon (DLC), which has a Fermi potential of 260 neV. Further developments are on going with non metallic electrodes made of carbon [65]. The insulator ring has a very large resistivity ($> 10^{16} \Omega\text{cm}$) in order to limit the leakage currents which may flow from one electrode to the other when the HV is applied. The Sussex/RAL/ILL collaboration was using a quartz insulator which has a low depolarization probability for UCN and mercury, but also a low Fermi potential (95 neV). A new insulator made of polystyrene coated with deuterated polystyrene (DPS) was built. The mercury performances are the same, but the Fermi potential is increased up to 162 neV [66].

Detector

A new detection system was constructed for the nEDM experiment at PSI. The former experiment used the standard Strelkov Helium 3 gas counter [45]. The main problem of such detectors is the duration of the signal ($\approx 2 \mu\text{s}$) which is too long for the high counting rates (up to 10^6 UCN/s) expected at PSI. A new type of high counting rate UCN detector based on ^6Li doped glass scintillator was developed. The cross section of the neutron capture on ^6Li nuclei is $\sigma_{abs}^{th}=940$ barn for thermal neutrons. The reaction is:



The energy released by the two charged products induces the excitation of the Ce_2O_3 molecules. They deexcite by scintillation (≈ 7000 photons per neutron capture) and emit blue photons which are collected by a photomultiplier tube. Efficiency tests have shown an UCN efficiency of detection similar to gas ^3He counters [67]. The nEDM detector Nanosc (Fig. 2.5) is segmented in 9 channels (hence its name). Each channel is made of a square scintillator ($28 \times 28 \text{ mm}$), coupled to a Hamamatsu photomultiplier tube (PMT). This allows decreasing the maximum counting rate per channel down to an acceptable rate for the PMT, *i.e.* few 10^5 UCN/s. Edge events occur when one of the two products escapes the scintillator without depositing all its energy. The scintillators are sensitive to gammas, but a good n/γ discrimination can be achieved if the edge events are suppressed. In order to recuperate the energy of the escaping fragments, a ^6Li depleted glass is used in front of a ^6Li enriched layer resulting in a full energy collection [67]. Glass scintillators of such type have been tested in the beam of SINQ and received about 10^{13} neutrons per cm^3 [68] without deterioration. Finally, the Fermi potential of such a scintillators is between 85 and 110 neV, larger than the aluminum Fermi potential used for the entrance window of the gas detector. In the nEDM experiment the detector is located 1600 mm below the precession chamber so that UCN will have at least 160 neV. This allows the slowest UCN from the chamber to be detected.



Figure 2.5: The multi-detector Nanosc.

2.2.3 Magnetometry

The monitoring of the magnetic field is a key point of the nEDM experiment. Two magnetometers are used in order to perform such a task. They allow the correction for magnetic field fluctuations during cycles and the estimate of magnetic field gradients.

The mercury co-magnetometer

The mercury scalar co-magnetometer was already used in the experiment performed at ILL by the Sussex/RAL/ILL collaboration. It allowed the Sussex/RAL/ILL collaboration to reduce by one order of magnitude as compared to previous external magnetometer the systematic error on the neutron EDM [69]. The co-magnetometer gives a volume and time averaged value of the magnetic field modulus within the precession chamber for each cycle. This allows the correction on the measured neutron frequency. ^{199}Hg are produced by heating mercury oxide, polarized by a discharge bulb containing mercury and injected within the precession chamber. A $\pi/2$ pulse is used to rotate the spin as it is done with UCN, and the mercury is precessing during nearly the same time as the UCN. The magnetic gradients cannot be estimated with the mercury co-magnetometer, another magnetometry system has to be used. The performances and the improvement of the mercury co-magnetometer for the nEDM experiment at PSI were the aim of two PhD thesis within the collaboration [4, 70].

The cesium magnetometer

The scalar cesium magnetometers are a new part of the experiment at PSI. They have been added to estimate the vertical gradients of the field modulus. The system consists in laser optically pumped cesium vapor. In a magnetic field, the precession frequency of the vapor is measured with an integrated RF pickup coil. The technical challenges were to reduce the size of the system and make it high voltage compatible. The Cs magnetometers are only able to measure the modulus of the magnetic field. Twelve magnetometers are used to estimate the vertical gradients: eight below the bottom electrode, and four above the top electrode (Fig. 2.3). The performances and optimization of the Cesium magnetometers for the nEDM experiment at PSI are the aim of a PhD thesis in the collaboration [71].

2.2.4 High voltage

The high voltage system was completely redesigned for the experiment at PSI. Preliminary tests were done in a dedicated test setup. An electric field of 200 kV was reached. In the nEDM apparatus, it was possible to reach 140 kV with small sparks (less than 1 nA). The monitoring of the leakage current was also improved. It is now possible to measure leakage currents smaller than 50 pA. The performances and optimization of the High voltage setup for the nEDM experiment at PSI are the aim of a PhD thesis in the collaboration [65].

2.2.5 Magnetic field

Four layers magnetic shield

The magnetic field inside the precession chamber is protected from external magnetic disturbances with a magnetic shield made of high permeability magnetic material. Mu-Metal, with a large

magnetic permeability (around 20000) has been used. The PSI shield is the same as the one used by the Sussex/RAL/ILL collaboration. It consists in four cylindrical shield layers. The shielding factors, which are the ratio of the external field divided by the internal field, are given in Table 2.1. The ratio depends on the field direction due to symmetry breaking of the shield: the four cylinders have endcaps (to access the vacuum chamber) and holes (feedthrough for the high voltage, the neutrons and the mercury). This leads to a reduction of the shielding factor in the Y and Z directions. Shielding factors were measured in 2009 using low frequency excitations (10 mHz), as expected, the shielding factor is smaller in the Y direction (endcaps) and Z direction (holes).

Table 2.1: Measured shielding factor at PSI

Direction	Shielding factor
X	13300 ± 600
Y	1600 ± 20
Z	8600 ± 300

B_0 coil

The B_0 coil creates the static magnetic field ($B_0 = 1 \mu\text{T}$) in the precession chamber. This coil is the same as in the previous experiment. The ideal model of the B_0 coil consists in 54 horizontal rectangular coils wound on the vacuum chamber of the experiment. Each coil is separated by a distance of 2 cm ($\cos\theta$ geometry). The field created by this coil is not homogeneous inside the precession chamber because of the shield defects (holes, endcaps). Trim coils are used in order to correct for such inhomogeneities.

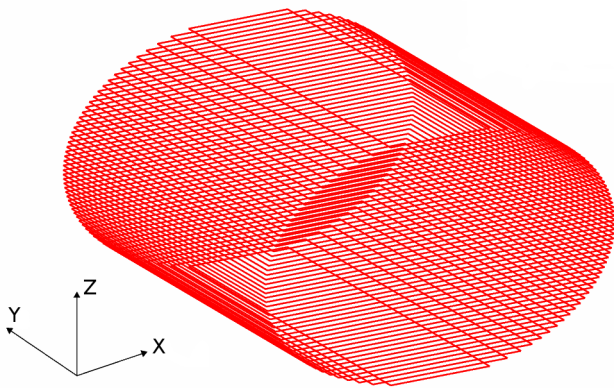


Figure 2.6: Drawing of the B_0 coil. This geometry is used for magnetic field simulations (Chap. 3)

Trim coils

The trim coils are used to improve the field homogeneity within the precession chamber. At ILL, eight trim coils were used for the correction of the vertical field inhomogeneities, three trim coils for the compensation of the holes disturbances. At PSI, the trim coils were fully redesigned. Thirty three coils are now in place. These coils can be divided in four groups:

- the chimney coils, used to compensate the effect of the holes in the magnetic shield. They are placed in the neutron hole, the mercury hole and the high voltage hole.
- the Top-Bottom coils, mainly used for the correction of the vertical gradients.
- the Left-Right coils, mainly used for the correction of the horizontal gradients (along the X axis).
- the Helmholtz coils, used for the correction of the horizontal gradients (along the Y axis).

These coils are shown in Fig. 2.7 (except the three chimney coils). Most of the Top-Bottom coils were already existing. The Left-Right coils are new. They are identical to the Top-Bottom.

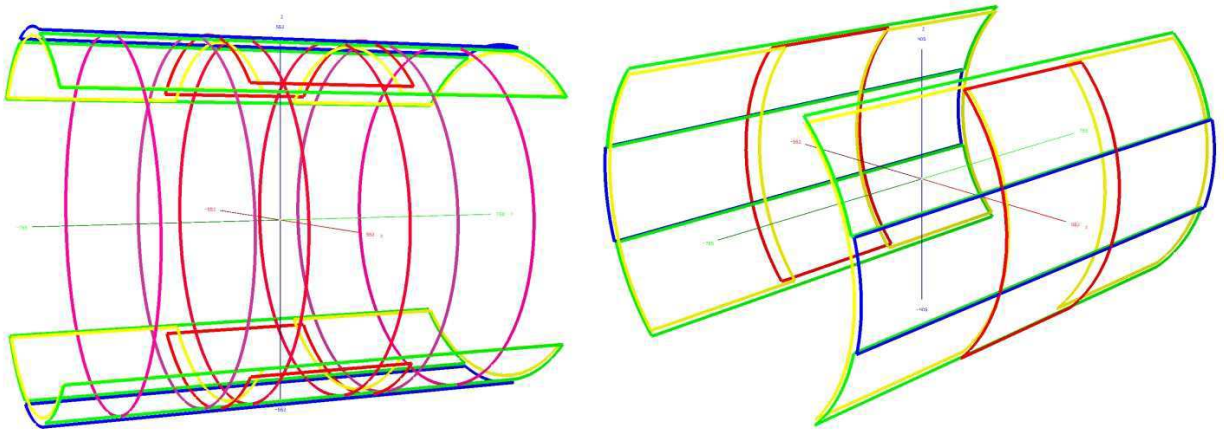


Figure 2.7: Left (a): Top-Bottom and Helmholtz trim coils. Right (b): Left-Right trim coils.

The fields created by the coils were mapped. The current optimization was first calculated, followed by a “by hand” optimization. It leads a homogeneity of $5 \cdot 10^{-5}$ in the storage volume. Furthermore, the trim coils system can be used to generate gradients, with the purpose of studying effects depending on magnetic field inhomogeneities.

Surrounding Field Compensation coils

The Surrounding Field Compensation (SFC) coils are a set of three pairs of rectangular Helmholtz coils. Their aim is to actively compensate the external magnetic field of the noisy magnetic environment at PSI (several experiments are using magnetic field around the nEDM experiment). Therefore, in the precession chamber the field is passively shielded by the four layers of the magnetic shield and, actively, by the SFC. The scheme of the SFC coils is shown in Fig. 2.8.

The study and optimization of the SFC system is included in a PhD thesis in the collaboration [72].

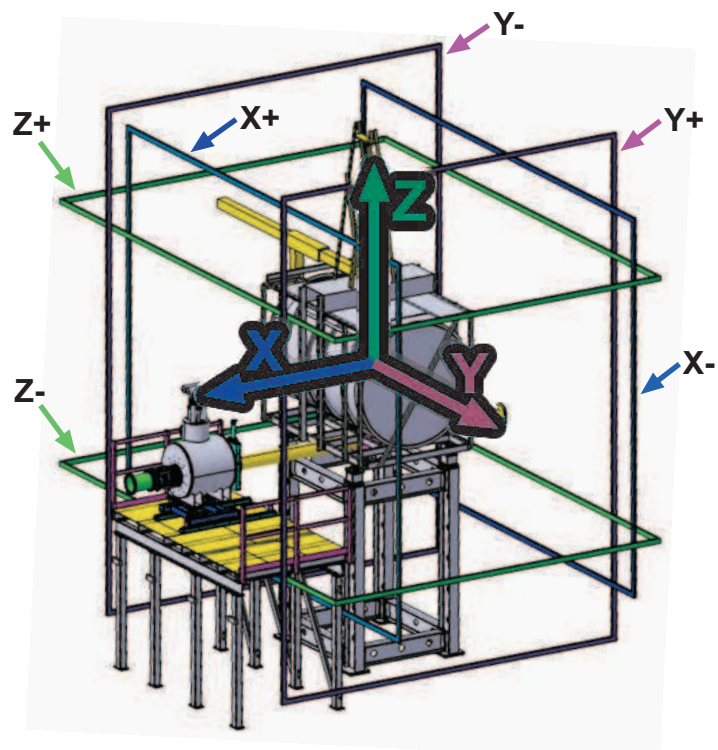


Figure 2.8: Drawing of the SFC coils

CHAPTER

3

Spin transport: the guiding field system

3.1 Introduction

This chapter focuses on how to maintain the polarization during the UCN transport from the superconducting polarizer magnet (SC) to the precession chamber. Two sources of depolarization may occur within the UCN guides during transport: depolarization due to wall collisions and depolarization due to magnetic field inhomogeneities. The first one is related to microscopic interactions between neutrons and nuclei. This phenomenon is described in the next chapter. The second phenomenon is a pure electromagnetic process: the interaction between the neutron spin and the ambient magnetic field. We will see in this chapter how depolarizations have been limited by the addition and optimization of a guiding field system.

3.2 Depolarization due to magnetic field inhomogeneities, adiabaticity parameter

As seen in Chap. 1, for a single UCN in the laboratory frame R_{lab} , Bloch equations are given by:

$$\frac{d\vec{P}}{dt} = \gamma_n \vec{P} \times \vec{B} \quad (3.1)$$

with \vec{P} the polarization vector and γ_n the gyromagnetic ratio of the neutron.

In this frame, the magnetic field is assumed static (the radio frequency magnetic fields are not treated in this part, and the current sources which supply the coils are assumed absolutely stable). A neutron at rest in the laboratory frame will not “see” any evolution of the magnetic field. In the frame moving with the neutron R_{UCN} , the static field becomes time dependent, and

any change in the magnetic field direction can be seen as a rotation of this field. The angular frequency of this rotation is noted $\vec{\Omega}$. A new frame R_{rot} is defined as a frame placed at the neutron place and with the x axis staying aligned with the magnetic field and the y axis staying orthogonal to the magnetic field. In this frame, the neutron is seeing an additional motional magnetic field directly proportional to the angular frequency: $\vec{B}_{mot} = \frac{\vec{\Omega}}{\gamma_n}$. This leads to a new expression for the Bloch equations:

$$\left. \frac{d\vec{P}}{dt} \right|_{rot} = \gamma_n \vec{P} \times \left(\vec{B} + \frac{\vec{\Omega}}{\gamma_n} \right) \quad (3.2)$$

This equation can also be written using the notation of angular frequencies:

$$\left. \frac{d\vec{P}}{dt} \right|_{rot} = \vec{P} \times (\vec{\omega}_L + \vec{\Omega}) \quad (3.3)$$

The spin motion depends on the relative values of the Larmor frequency of the neutron and the rotation rate of the field $\vec{\Omega}$. The adiabaticity parameter k is defined as the ratio of these two quantities:

$$k = \frac{\omega_L}{\Omega} \quad (3.4)$$

If $k \gg 1$, the predominant term in the Bloch equations is the Larmor precession frequency ω_L . In this case, the field is slowly varying compared to the Larmor rotation frequency, the neutron spin is able to “follow” the magnetic field: one says that the adiabatic condition is fulfilled. In the other case ($k \not\gg 1$), the spin does not have time to stay aligned with the magnetic field, and depolarizations occur. If the adiabaticity condition is fulfilled everywhere inside the UCN guide from the polarizer to the precession chamber, then the polarization is conserved. In our case, the critical point is a $\pi/2$ rotation of the field from $-x$ direction to $\pm z$ direction (Figure 3.3 shows a view of the system with its reference frame.) In the case of a field rotation from a time t_1 to t_2 , at a frequency ω , the magnetic field components can be expressed as:

$$B_x = B \cos \omega(t_2 - t_1), \quad B_z = B \sin \omega(t_2 - t_1) \quad (3.5)$$

For a magnetic field with the same magnitude during the rotation, the polarization along the new magnetic field direction can be expressed analytically and is a function of k . It can be calculated by solving the Bloch equations in R_{rot} . Thus, the expressions of the polarization along the x , y and z axis as a function of the rotation angle θ for an initially fully polarized UCN along the x axis are [73]:

$$P_x = \frac{\cos(\theta)(k^2 + \cos(\theta\sqrt{1+k^2})) + \sqrt{1+k^2} \sin(\theta) \sin(\theta\sqrt{1+k^2})}{1+k^2} \quad (3.6)$$

$$P_y = \frac{k - k \cos(\theta\sqrt{1+k^2})}{1+k^2} \quad (3.7)$$

$$P_z = \frac{\sin(\theta)(k^2 + \cos(\theta\sqrt{1+k^2}))}{1+k^2} - \frac{\cos(\theta) \sin(\theta\sqrt{1+k^2})}{\sqrt{1+k^2}} \quad (3.8)$$

In our case, the polarization along the new axis after a $\pi/2$ rotation is:

$$P = \frac{k^2 + \cos(\frac{\pi}{2}\sqrt{1+k^2})}{1+k^2} \quad (3.9)$$

Figure 3.1 shows the evolution of the probability as a function of k . An adiabaticity factor of 12 is enough to get a polarization along the z axis at more than 99 % after one passage in the rotation region. This will be our requirement.

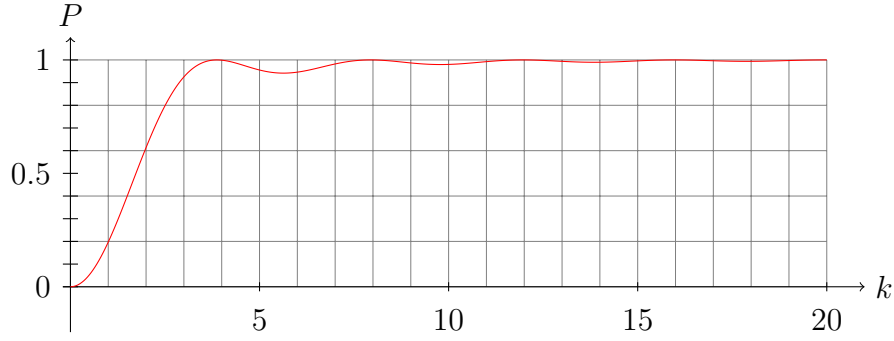


Figure 3.1: Evolution of P_z after a $\pi/2$ rotation of the magnetic field as a function of the adiabaticity parameter.

Outside of the rotation area, the field is kept along the guide axis, *i.e.* $B_{\parallel} \gg B_{\perp}$. In this case, the probability of spin flip decreases exponentially with k . The polarization along the initial axis is [74]:

$$P = 1 - e^{-\pi k} \quad (3.10)$$

For a neutron at rest in a time dependent field, k is a function of the time variation of the field:

$$k = \frac{\omega_L}{\Omega} = \frac{\gamma_n B^2}{\frac{dB}{dt}} \quad (3.11)$$

Assuming a neutron going along the z axis with a velocity v_n , the adiabaticity parameter can be rewritten as a function of the velocity and the gradient of the transversal component of the field:

$$k = \frac{\gamma_n B^2}{v_n \frac{dB_{\perp}}{dz}} \quad (3.12)$$

The adiabaticity parameter can also be written as the exact ratio of angular frequencies:

$$k = \frac{\gamma_n B}{v_n \frac{d\alpha}{dz}} \quad (3.13)$$

with $v_n \frac{d\alpha}{dz} = \frac{d\alpha}{dt} = \Omega$. In this way, it is possible to calculate the adiabaticity parameter between two close points 1 and 2 as:

$$k = \frac{\gamma_n B \parallel \vec{r}_2 - \vec{r}_1 \parallel}{v_n \arccos(\frac{\vec{B}_1 \cdot \vec{B}_2}{B_1 B_2})} \quad (3.14)$$

Both Eqs. (3.12) and (3.14) are used to analyze and interpret the mappings at PSI (Sec. 3.4.4) and simulations. They are giving the same results at the level of 10 %. One has to determine the neutron velocity used in these formulae. A constant velocity was used, larger than the maximum velocity the UCN can have (then the adiabaticity parameter is underestimated). The UCN spectrum is “cleaned” in the source tank by the Fermi potential of the tank walls, which is $V_F = 260$ neV. This corresponds to a velocity of 7 m/s. This velocity is used in the calculations.

A new holding field system has to be setup at PSI in order to keep the polarization of the UCN during their transport. Let us first compare the present situation at PSI with the former one at ILL before discussing the simulations and measurements which have led to the final setup.

3.3 The PSI setup: changes with respect to the ILL setup

In terms of polarization and spin transportation, the situation between the experiment at ILL (phase I) and at PSI (phase II) is different: first of all, the polarizing iron foil was replaced by a superconducting solenoid magnet in order to improve the polarization efficiency (Chap. 5). Due to a large stray field of the magnet (15 G at one meter on the axis of the coil) and because of the size of the polarizer (the superconducting coil is in a cylindrical helium vessel with a diameter of 86.4 cm and a length of 83.2 cm, the helium vessel is connected to a cooling device) the distance between the polarizer and the precession chamber was increased, from 1.5 m to 3.5 m. Furthermore, the Earth’s magnetic field (which was part of the holding field for the UCN at ILL) is now reduced by the Surrounding Field Compensation coils system (Sec. 2.2.5). Finally, the analyzing system has changed and is not at the same location as before: its stray field is different. Figure 3.2 shows the field modulus difference between the ILL configuration and PSI configuration along the vertical guide (no trim coils are used). At PSI, the field modulus is really smaller than at ILL before the second external shielding layer. Furthermore, the adiabaticity parameter along the vertical guide is small (Fig. 3.4). New magnetic field sources have to be added to allow an adiabatic transport of the neutron spin (Fig. 3.3) along the whole path from the polarizer to the precession chamber.

3.4 Creation and optimization of the new Guiding Field system

Two different systems can be used to create a magnetic field: permanent magnets or coils. Coils are chosen for this task to allow tuning of magnetic fields. Several simulations were performed to choose a working configuration. Two magnetic field computation codes were used to perform the simulations: RADIA [75] and MAENTOUCH [76].

3.4.1 Simulations with Radia

RADIA [77] is a magnetic field computation code written in C++ and using MATHEMATICA [78]. It is based on the *Boundary Integral Method* (BIM): each magnetic material of the simulation is divided into small cells in which the magnetization is considered constant. Magnetic fields can be created by three kinds of field sources:

- magnetic materials (divided small cells)

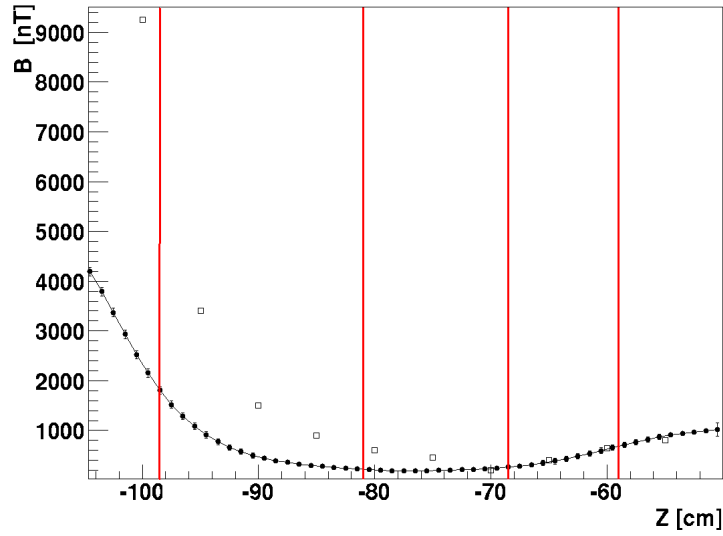


Figure 3.2: Modulus of the magnetic field at the center of the vertical guide as a function of the height for a B_0 down configuration. (0 cm corresponds to the center of the precession chamber) Black dots are from a measurement performed at PSI with SFC ON. Empty squares were done at ILL and comes from [4]. Red lines corresponds to the positions of the four shielding layers. No trim coils were used.

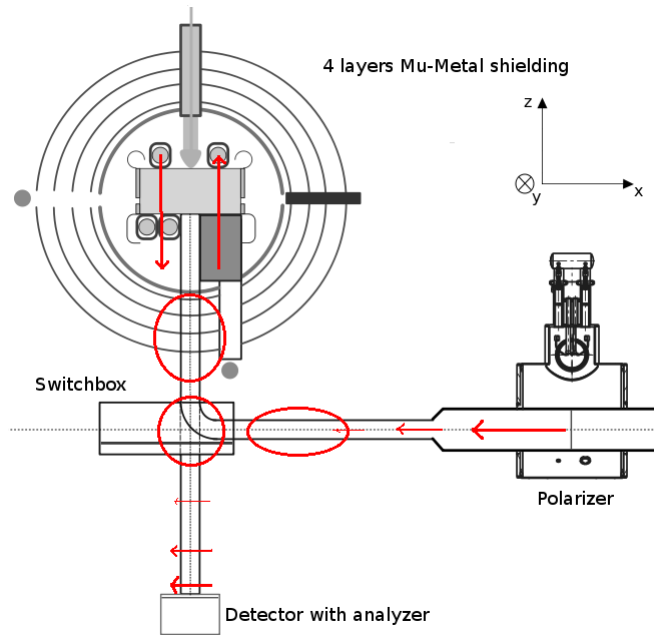


Figure 3.3: Scheme showing the nEDM experiment and main magnetic field sources. The arrows are the direction of the magnetic field. Red ellipses corresponds to regions where low field is expected. The experiment reference frame is also depicted.

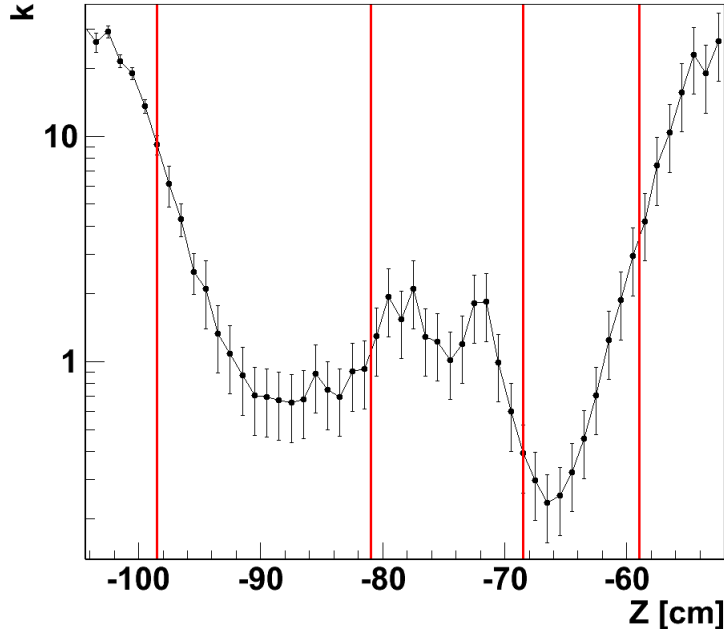


Figure 3.4: Adiabaticity parameter k along the vertical guide at PSI with no trim coils. The values of k are definitely below the requirement.

- current sources as wires (mathematical lines)
- constant background field

In case of current sources, the field is integrated along the wire using the Biot and Savart law. The magnetic field created by all the field sources is a function of the magnetization of each cell. Indeed, having N cells, the magnetic field \vec{H}_i at the center of the i -th cell is:

$$\vec{H}_i = \sum_{k=1}^N \mathbf{Q}_{ik} \vec{M}_k + \vec{H}_{ext_i} \quad (3.15)$$

\vec{M}_k is the magnetization of the k -th cell, \vec{H}_{ext_i} the contribution of the external fields at the center of the i -th cell and \mathbf{Q}_{ik} a 3×3 matrix which elements are functions of the geometry of the cell. All these $N \times 3 \times 3$ matrices form the so called Interaction Matrix. A relaxation scheme is applied to the matrix to determine the value of all individual magnetization vectors. After that, the magnetic field can be calculated at each point of space by adding the contribution of each field source and cell. It was possible to determine the regions where the magnetic field has to be enforced as shown for instance in Fig. 3.3. The problem was divided into two different parts. The first part concerns the magnetic field along the horizontal guide, from the SCM to the switchbox. The second part is related to the vertical guide.

The horizontal guiding field

Two main field sources have an influence on the horizontal magnetic field along the UCN guide:

- the stray field of the superconducting polarizer (acting close to the magnet)
- the stray field of the analyzer (acting close to the switchbox)

The superconducting solenoid magnet was not simulated in RADIA as a coil. Its geometry is not exactly known, but the field created by the superconducting coils was provided by the company which built the magnet and maps were also done (Chap. 5). Due to the cylindrical geometry of the coil, the magnetic field components of the magnet are given as a radial part B_r and an axial part B_x . We can observe in the theoretical field plots that the radial component of the field B_r at 36.5 mm from the center is at least 10 times smaller than B_x . Furthermore, in a plane perpendicular to the guide line, the field is rather homogeneous (differences less than 1 %). Using all these considerations, the magnetic field can be fitted by a function which depends only on the x coordinate (axial). The function used to fit the area of interest is:

$$\frac{1}{ax^2 + bx + c} \quad (3.16)$$

The result is shown in Fig. 3.5. The fit function is:

$$B_x(x) = \frac{1}{2.74 \times 10^{-6} \times x^2 - 6.78 \times 10^{-4} \times x + 4.54 \times 10^{-2}} \quad (3.17)$$

The contribution of the SCM field was added outside of RADIA using the fit function, assuming the SCM does not magnetize the magnetic pieces simulated in RADIA. This assumption is justified by comparing the magnetic field generated by the SCM at the location of the magnetic pieces and the one generated by the initially magnetized pieces in RADIA. There are 3 orders of magnitude between the two fields.

The second part is the analyzer. Its geometry is known and it was added to RADIA (Fig. 3.6). As described in Sec. 2.2.2, the analyzer is made of soft iron for the return yoke and NdFeB magnets for the magnetization of the iron foil. The soft iron, called XC10, contains less than 0.09% carbon. RADIA disposes of several pre-defined materials in its database. One of them is the XC06, which is close to the XC10. This material was used for the simulation. RADIA parameters for the magnets (magnetic susceptibility and magnitude of the remnant magnetization vector) were tuned to fit with the measured field. A value of 1.325 T for the remnant magnetization was used. Table 3.1 shows the comparison between the mapped field and the field simulated with RADIA. Measured and calculated fields are in agreement.

Table 3.1: Mapping of the analyzer stray field modulus compared to the simulated one in RADIA. $z = 0$ corresponds to the center of the return yoke. The z direction is the same as the experiment

z (cm)	0	10.5	14.5	16.5	18.5	20.5	22.5	24.5	26.5	28.5	30.5
B_{meas} (G)	300	37	15	9	6	4	3.5	2.4	2	1.6	1
B_{calc} (G)	329	42	15	10	7	4	3.1	2.2	1.8	1.3	1

The last system simulated comprises the Earth field and the Surrounding Field Compensation system (Sec. 2.2.5). The Earth magnetic field was measured at PSI before the layers of Mu-metal

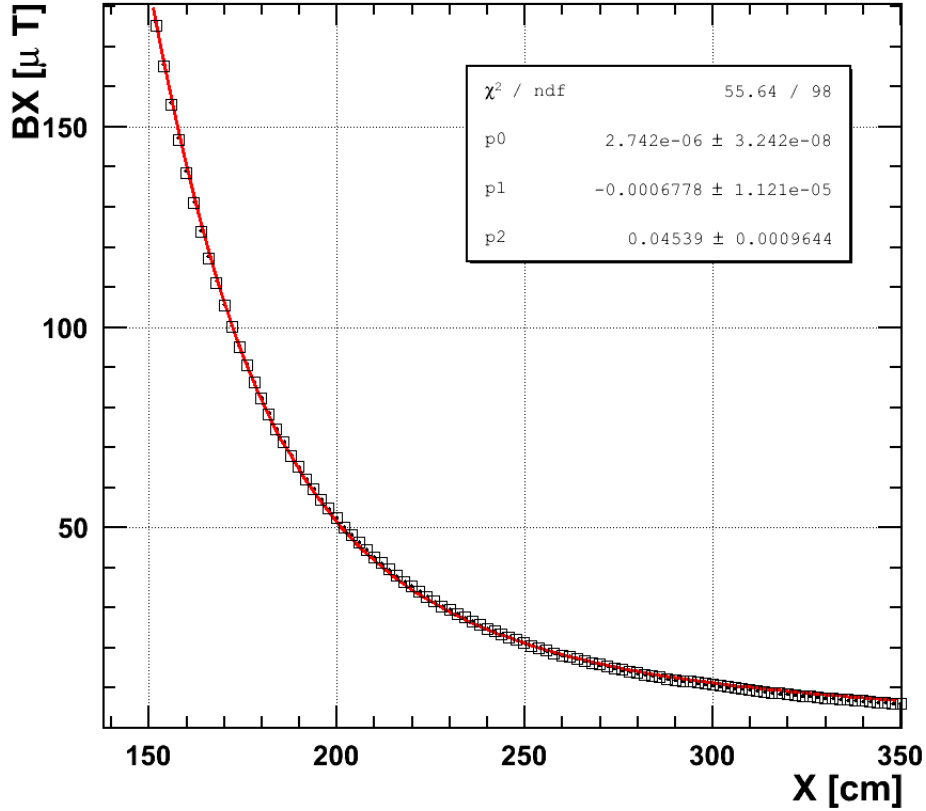


Figure 3.5: Axial stray field of the superconducting magnet. Black dots represents the field at the center of the UCN guide, empty squares the field at the edges of the UCN guide and the red line is the fit. $x = 0$ corresponds to the center of the SC magnet.

shielding was placed. Its value is:

$$\mathbf{B} = \begin{pmatrix} 37.0 \mu\text{T} \\ 10.4 \mu\text{T} \\ -40.5 \mu\text{T} \end{pmatrix} + \begin{pmatrix} -0.7 & -1.3 & 1.1 \\ -1.3 & -0.4 & 1.0 \\ 1.1 & 1.0 & 1.1 \end{pmatrix} \begin{pmatrix} X \\ Y \\ Z \end{pmatrix} \times 1 \mu\text{T/m} \quad (3.18)$$

The point $X = Y = Z = 0$ corresponds to the origin of the experiment reference frame (center of the precession chamber). Unfortunately, it is not possible to use such a function in RADIA, the software does not allow the use of a non constant background field. It was decided to assume a constant Earth field, by taking into account only the value at the center of the frame. The error done by this assumption is less than 3 % for the X and Z components and is larger for the Y component, about 10 %. The SFC were simulated using mathematical lines. The sizes and positions of the simulated coils are the same as the ones measured on site. These numbers are summarized in Table 3.2. To simplify the model, each coil of the SFC was modeled by a single wire although in reality each coil is made of 9 to 18 wires. This simplification was justified



Figure 3.6: The analyzer and its RADIA model. The four magnets are in blue, the return yoke is in red). RADIA parameters were adjusted to fit with the real analyzer field (Table 3.1).

because the wires are thin and compact (6 mm^2 cross section) compared to the coils dimensions. Far away from the wires, the field created by N wires with a current I is equivalent to a single wire with a current $N \times I$. Currents were optimized to cancel the Earth field at the origin. These

Table 3.2: Dimensions and positions of the 6 SFC coils used in the RADIA simulation. All the distances are given in cm. The offsets are the differences between the position of the coil pairs center and the experiment reference frame origin.

coil	long side	short side	distance	x offset	y offset	z offset
X_-	788	608	422	-23	0	-7
X_+	787	607				
Y_-	816	594	512	11	3	-19
Y_+	843	595				
Z_-	802	584	423	11	1	-16
Z_+	797	584				

systems were used for the horizontal guide field simulation (the analyzer, the SFC and the Earth field as elements of the code, the SC magnet as a function). The result is shown in Fig. 3.7 (black line). At 30 cm from the switchbox center, the magnetic field is close to zero, and can be canceled if an external field source is switched on. This can happen with large external field sources like the superconducting magnets from other experiments (Sec. 3.4.4). To avoid this effect in the horizontal guide, it is possible to boost the stray fields of the polarizer and analyzer by adding field sources. This was done by the addition of a solenoid between the SC magnet and the switch to boost the stray field of the magnet and also rectangular coils around the switch, to boost the horizontal component of the analyzer stray field. As a result, low field regions are avoided as shown in Fig. 3.7.

In these regions, the minimum field value is $60 \mu\text{T}$, which is larger than the maximum external field disturbances measured ($40 \mu\text{T}$). Furthermore, there is no rotation of the field

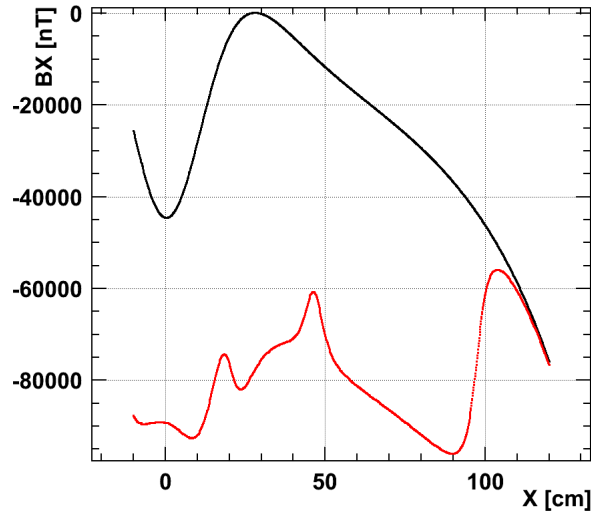


Figure 3.7: Simulated field along the horizontal guide with guiding coils added (red line) and without (black line). A $60 \mu\text{T}$ holding field was assumed. The zero here is the crossing point between horizontal and vertical guide.

along the guide since the field sources are just solenoids. The adiabaticity parameter k is more than 1000 in this area. The field is mainly axial, no depolarizations due to magnetic field inhomogeneities are expected here. Nevertheless depolarizations can occur along the horizontal guide if the solenoid is separated in two parts, and if there is a gap in between these two parts. This is the case in our setup where a mechanical piece is used to hold the horizontal guide and prevents us to use a single solenoid. The adiabaticity parameter was calculated on and off axis as a function of the gap size. The results are shown in Table 3.3. The two extremes cases are considered: at the center of the neutron guide and at the edges of the guide.

Table 3.3: Adiabaticity parameter as a function of the gap between the two solenoids.

Gap (mm)	k on axis	k off axis
0	1000000	5000
20	200000	200
40	100000	90
60	80000	20
80	20000	17
100	8000	15
120	3000	14

One can see that k deteriorates quickly close to the guide edge. This is due to the fact that the magnetic field created by a solenoid decreases quadratically with the distance from the axis. It does not appear to be a problem in our case because the adiabaticity parameters are larger

than one even with a large gap. But a large gap means a large region where the magnetic field can potentially cancel in case of external perturbations. So the smallest gap was chosen, it corresponds to the thickness of the mechanical piece (40 mm).

Table 3.4 summarizes the specificities of the new coils.

Table 3.4: Characteristics of the coils used for the horizontal spin guiding system.

coil	type	length (mm)	radius (mm)	number of turns	current (mA)
HGSW	Solenoid	250	83	250	50
HGSC	Solenoid	300	83	300	50
SR 1	Rectangular	300	130	49	60
CSWC	Rectangular	300	350	50	60
SR 2	Rectangular	300	130	49	60

The vertical guiding field

For the vertical part, RADIA has unfortunately reached its limitations for the design of the coils which are going through the shield. The adiabaticity parameter k is inversely proportional to the gradient of the magnetic field (Eq. (3.12)). Because of the way to calculate the magnetic field created by each uniformly magnetized cell in RADIA, it becomes difficult to calculate gradients. Indeed, in the extensions of the cells faces, the magnetic calculation diverges. The geometry of the vertical guiding field coils was roughly chosen by doing an approximation within RADIA (the aim was to reduce the number of cells and thus the crossing of the facets planes). Then, the fine optimization (tuning of the current, location of the coils and slight modification of the geometry) was done by using another computation code (Sec. 3.4.3). The magnetic shielding layers were not simulated to reduce the number of cells. In the real magnetic shield (Sec. 2.2.5), three vertical Mu-metal cylinders are soldered on the shielding layers around the neutron hole. This was done to reduce the effect of the hole on the field homogeneity in the precession chamber. These three cylinders are very close and can be considered as one whole cylinder which was the only one being simulated. Indeed, it is the closest magnetic piece and therefore contributes more to the field. The magnetic field has to be rotated from the switchbox (field along the x axis) to the precession chamber (field along the z axis). Some coils will be added to perform this rotation. Other requirements for these coils are:

1. to keep an acceptable adiabaticity factor inside the vertical guide.
2. to be able to guide the neutron spin in the same way independently of the polarity of the B_0 coil.
3. to avoid magnetizing other parts of the shield.
4. to avoid field inhomogeneities inside the precession chamber (low gradients outside of the coils).
5. to be efficient over the whole neutron guide (on the main axis, but also off axis).

6. to be independent of the existing field sources of the experiment
7. to be simple, compact and easily tunable.

A first series of simulations was performed to test a simple system: two rectangular coils going inside the shielding layers to boost the horizontal field. The length of these coils was chosen to keep a continuity between the field they generate and the B_0 coil stray field. A problem was observed close to the horizontal wires of the coils, where the magnetic field turns abruptly (mainly horizontal below the wires, mainly vertical above the wires, as shown in Fig. 3.8).

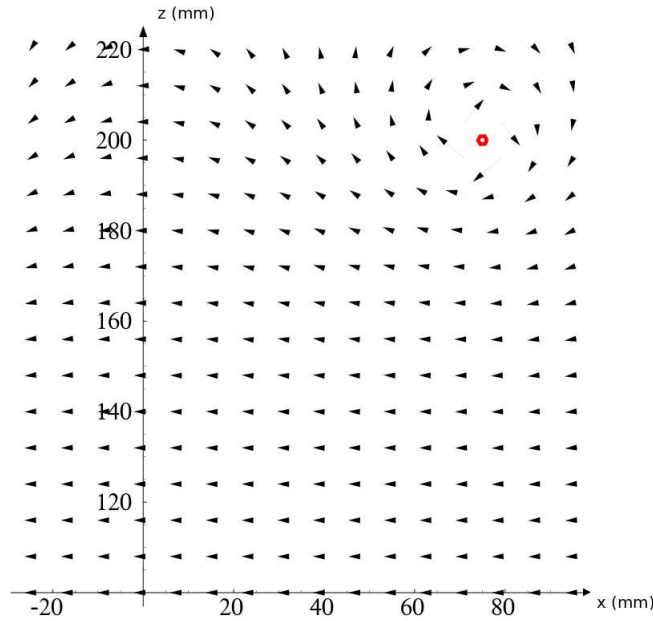


Figure 3.8: Rotation of the field close to the horizontal wire of the rectangular coil (the coil is in the yOz plane, the plane of the plot, xOz , is a plane of symmetry for the coil). The red circle denotes the cross section of the horizontal wire.

A field source which turns smoothly the magnetic field must be added here. The system will be composed of two parts:

- a part which extends the horizontal field from the switchbox
- a part which rotates the field from horizontal to vertical directions

Because of the geometry of the system (cylindrical guides) and to respect the point 5 above, the choice for the first part was turned to saddle coils, which provide good homogeneity between the two coils [79]. Four parameters are important in saddle coils, as shown in Fig. 3.9. The geometric parameters are: the radius of the coils, their lengths, the aperture angle of the coils and the current used [80]. These parameters have to be optimized.

The length L was selected using the fact that the field of the new guiding field system and the B_0 coil stray field have to overlap adiabatically without any trim coil (point 6). Figure 3.2 shows that the minimum value of the magnetic field is reached between 70 to 80 cm from the

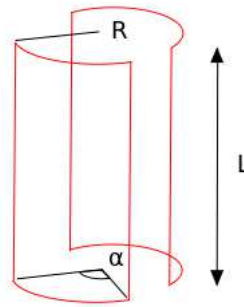


Figure 3.9: Scheme of a saddle coil pair with its tunable parameters: the length L , the radius R and the aperture angle α .

center of the precession chamber. Thus the length of the saddle coil pair is not a free parameter, the most important point is the length of the saddle combined to the second system and the range of its stray field. To increase the adiabaticity parameter, the magnetic field generated by the second system has to be strong. To limit its influence on the magnetization of the shielding layers (point 3), the extremity of the saddle coils is placed between two layers. It corresponds to a length of 47 cm. To have some positioning freedom during measurement, the coils length was reduced down to 45 cm. By this way, the saddle coils starts at the top of the switchbox (transition with the field of the horizontal guiding field part) and ends between the second and the third layer of shielding where the second system will be placed. Its stray field leads to an adiabatic transition towards the B_0 coil stray field. The second important point for the guiding field is the field homogeneity. Indeed, UCN are not going only in a straight line at the center of the guide but occupy the whole guide aperture. The magnetic field must be as homogeneous as possible to have the same adiabaticity value at different locations. The homogeneity is larger inside the UCN guide if the wires of the saddle coil are as distant as possible. A quality factor of the homogeneity can be defined as:

$$H = \frac{B_{max} - B_{min}}{B_{mean}} \quad (3.19)$$

with B_{max} the maximum value of the field, B_{min} the minimum value and B_{mean} the mean value of the field in the considered volume. The smaller the quality factor H , the more homogeneous the field. This factor was chosen to optimize the coils radius. The first limitation on the radius comes from the hole inside the shielding, where the saddle coils are located. The coils radius cannot be larger than 105 mm (which corresponds to the inner radius of the Mu metal cylinder). The minimum value is 40 mm (external edges of the neutron guide). The result is shown in Fig. 3.10.

As expected, the field homogeneity is larger when the radius increases. The optimal one is 90 mm. Unfortunately, because of the tightness of the apparatus (point 7), this radius cannot be used. Other coils, wires and systems in the vertical part prevent us to use this or a larger radius. In order not to distort the coil, the maximum possible radius is 60 mm. The field homogeneities at the center and at the edge of the coil are shown in Fig. 3.11.

The last parameter of the saddle coil is its aperture angle (the current is set as a free parameter for the fine tuning). The field homogeneity depends directly on this aperture angle.

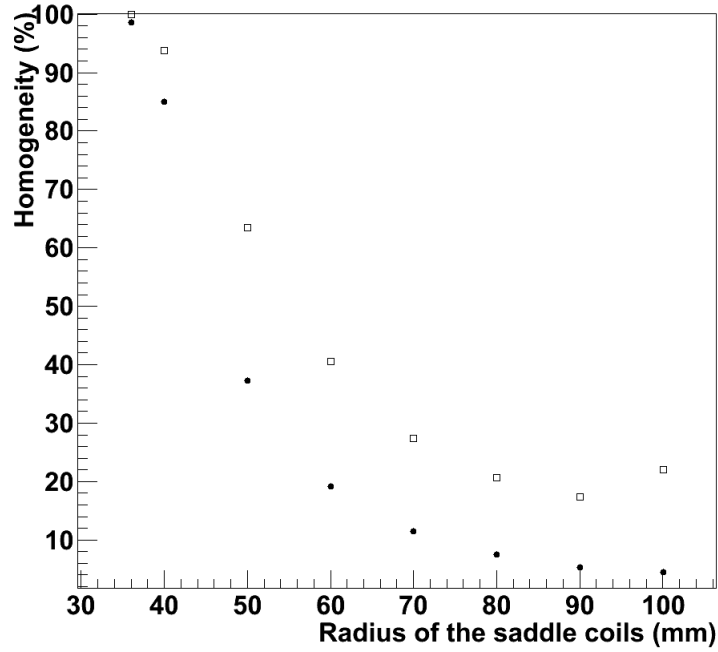


Figure 3.10: Homogeneity at the center of the saddle coils (black dots) and at the edge of the saddle coils (empty squares). The optimum radius is 90 mm.

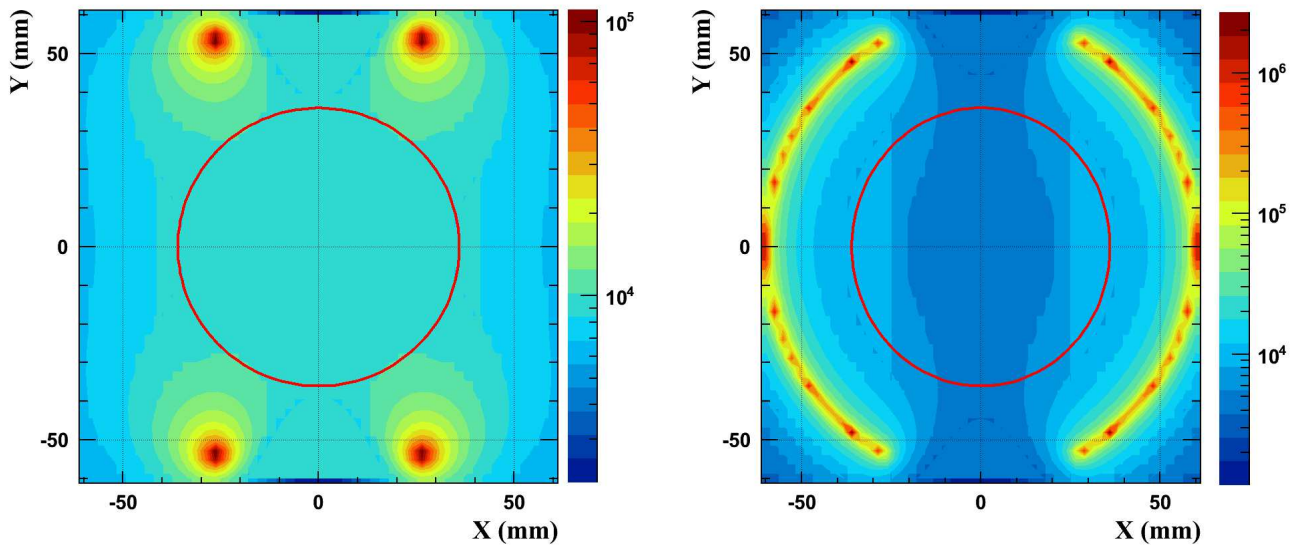


Figure 3.11: Field homogeneity in the xOy plane, at the center of the saddle coils (left picture) and at the edge of the saddle coils (right picture). The red circle represents the edge of the UCN guide.

To find this optimal place, the field homogeneity was calculated as a function of the aperture angle. The results are shown in Fig. 3.12. The optimum angle is $\alpha=128^\circ$.

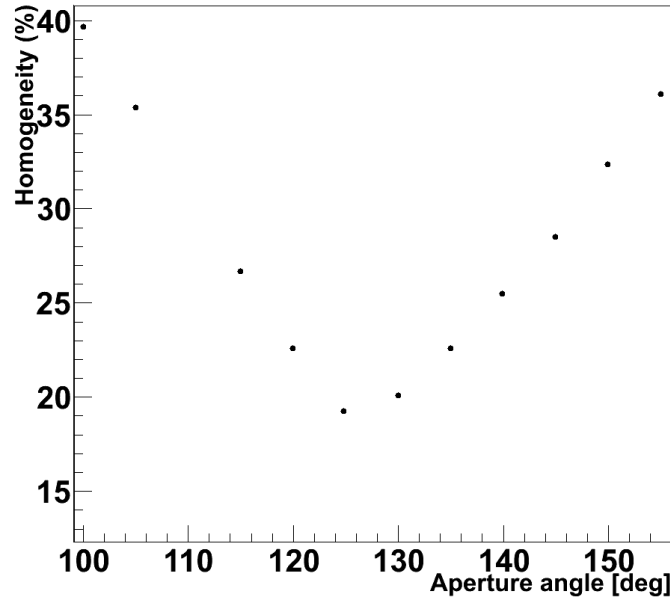


Figure 3.12: Field homogeneity at the center of the saddle coils as a function of the aperture angle of the coils. The largest field homogeneity (*i.e.* smallest quality factor) is found for $\alpha=128^\circ$

Now that the characteristics of the saddle coils are defined, the second system has to be developed. To fulfill all the points enumerated before, a solenoid system around the UCN guide was chosen. Indeed, solenoids give a good field homogeneity inside (point 5), have a cylindrical and low gradient field outside of the coil (point 4), create a mainly vertical field (point 1) and are simple and compact (point 7). The geometry and the placement of the solenoid system was chosen by looking how the adiabaticity parameter behaves close to the horizontal wires of the saddle coils. In this region (Fig. 3.13, left picture), the low adiabaticity region extends over a ten of centimeters. This observation fixes a lower limit on the size of the correction solenoid. Inside a solenoid, the field homogeneity depends on the ratio between the length of the solenoid and its radius. The smaller the radius, the larger the field homogeneity. The minimum allowed radius is 40 mm (external radius of the UCN guide). But we want to be able to move this coil to vary its relative position to the saddle coils. The solenoid is mounted on a Polymethyl methacrylate (Plexiglass) support which has to fit on the UCN guide. Then, its radius was enlarged to 56 mm. To optimize the adiabaticity parameter, we can force the UCN to precess faster by increasing the value of the magnetic field. The increase has to be local to avoid a large contribution of the solenoid field outside of the vertical guide, in the precession chamber. A possibility is to increase the solenoid winding density in the region of interest which is a few cm height where we cross the horizontal wires of the saddle coils. Due to building issues, it was chosen to add layers in the solenoid instead of increasing the winding density. This addition scales by 1.76 the field at the level of the horizontal wires, and only by 1.3 at 10 cm from the center. For compactness of the system, it was chosen to have a small length for the solenoid. The aim of this coil is to

correct the low region adiabaticity created by the saddle coils horizontal wires, above that, the spin is guided using the B_0 coil stray field.

Figure 3.13 shows the effect of the correction solenoids on the adiabaticity along the z axis. A factor of 10 is gained, k fulfills the requirements. One can also see the effect of the correction coil on the spin rotation speed. The spin rotates from the $-x$ to the $-z$ direction in less than 10 cm without the correction solenoid, and in 25 cm with the solenoid. Table 3.5 summarizes the specificities of the new coils.

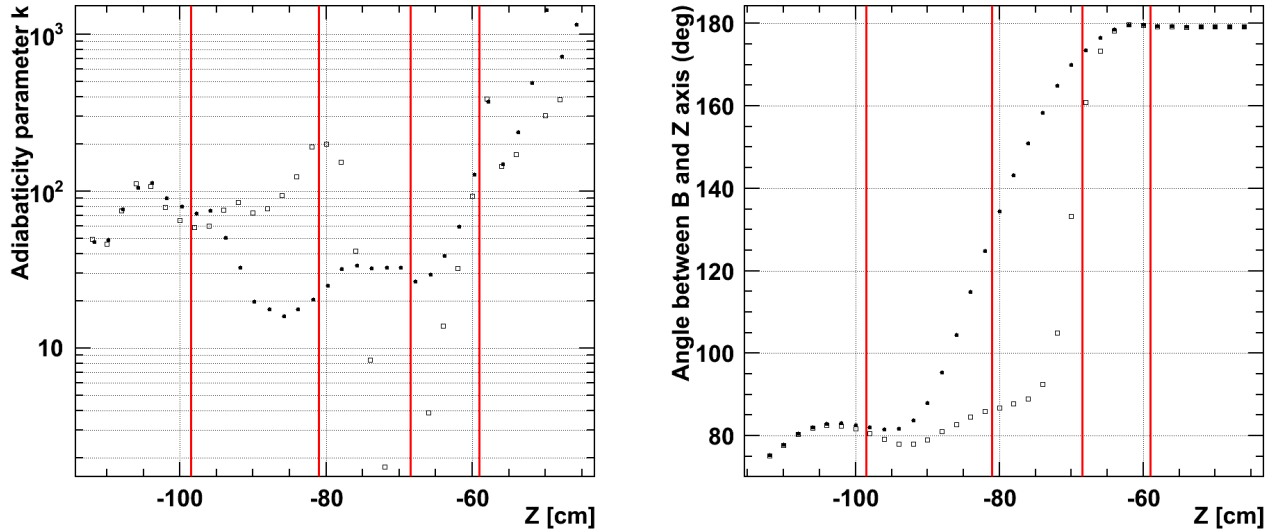


Figure 3.13: Left picture: Effect of the correction solenoid on the adiabaticity parameter k for a B_0 down configuration. k increases from 2 to more than 20 where the horizontal wire of the saddle coil crosses the vertical guide. Right picture: The effect can be understood easily by looking at the relative angle between the magnetic field and the z axis. Due to the correction solenoid, the magnetic field rotates more smoothly so that the neutron spin is able to follow it.

Table 3.5: Characteristics of the coils used for the vertical guide holding field.

coil	type	length (mm)	radius (mm)	nb of turns	current (mA)
Saddle	Saddle	450	60	20	30
CorSol1	Solenoid	150	56	300	2
CorSol2	Solenoid	50	56.5	100	2
CorSol3	Solenoid	25	57	50	2

3.4.2 Comparison with a first measurement

A preliminary magnetic field measurement was done to determine the relevance of the approximations done in RADIA. The measurement was done before the installation of the neutron

guides and the switchbox, which facilitated the procedure. A horizontal wooden plate with a square hole at its center was fixed below the magnetic shield where the switchbox is now located (Fig. 3.14, left picture). A graduated square-tipped plexiglass stick with a fixed 3 axis fluxgate was placed in the hole of the plate. In this way, the rotation of the probe is not possible. The probe and the stick are guided in an aluminium hollow tube fixed at the top of the magnetic shield through the vertical guide hole at its center. The plate and the stick are shown in Fig. 3.14. Then the stick is vertically moved inside the shielding layers. The field was recorded every cm from the center of the switchbox up to the bottom of the precession chamber.

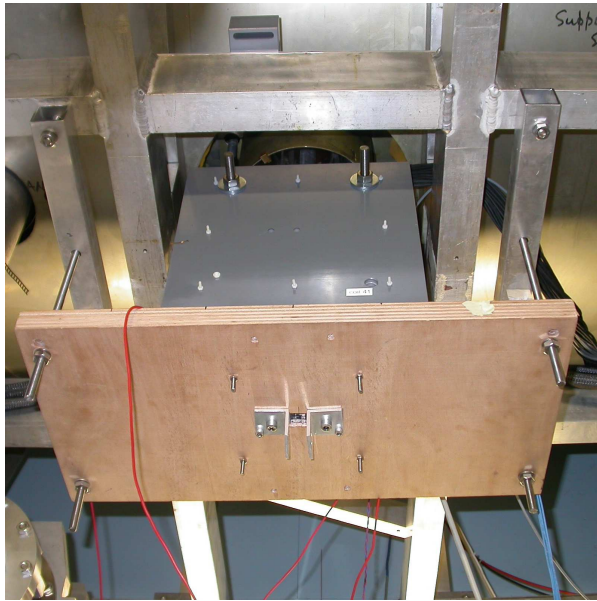


Figure 3.14: Picture of the wooden plate fixed below the magnetic shield (left side), and detail of this plate with the plexiglass stick in (right side).

The adiabaticity parameter can be calculated between two successive positions z_1 and z_2 using Eq. (3.12).

$$k = \frac{\gamma_n}{v_n} \frac{B_2^2 (z_2 - z_1)}{\sqrt{\sum_{i=x,y,z} \left(B_{i1} - B_{i2} - B_{i2} \frac{\sum_{j=x,y,z} B_{j2} (B_{j1} - B_{j2})}{B_2^2} \right)^2}} \quad (3.20)$$

Then the gradient of the transverse field components can be approximated between these two positions. The z step was chosen to have this approximation valid. A mapping at each centimeter is sufficient.

Two 40 cm long rectangular coils were placed inside the vertical small cylinder to compare the code and the mapped field. The results are shown in Fig. 3.15. The measurements and the calculation are in sufficient agreement considering the rough approximations made in this part.

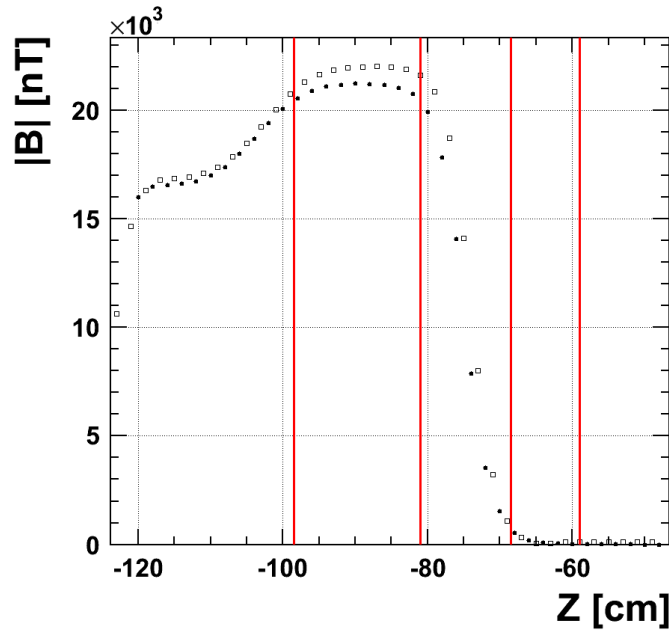


Figure 3.15: Comparison between the field computed with RADIA (empty squares) and the measured field (black dots). Inside the cylinder, the difference between measured and calculated field is about 5 %.

3.4.3 Simulations with Maentouch

A second computation code, called Maentouch, was used to perform the fine tuning of the guiding field coils. MAENTOUCH is a magnetic field calculation program written in C++ based on Root¹ libraries. The same philosophy as RADIA is used (*Boundary Integral Method*), but the procedure to calculate the magnetic field created by a magnetized cell is different. This makes the instabilities observed in RADIA to disappear. Further information concerning the calculations done with MAENTOUCH can be found in Ref. [81]. Before simulating the same full geometry as the one used in the RADIA, simulations were carried out to benchmark the two codes. The results are shown in Fig. 3.16. The difference between the two codes is less than 1 %, except for the y component which is not zero with the RADIA code.

Adiabaticity parameter calculation along the vertical guide

Simulations were done using the existing field sources and the ones simulated with RADIA. The aim was to have k larger than 12 inside the vertical guide. The parameters of the simulation are the followings:

- the Earth field is assumed completely compensated by the SFC coils (no contribution from Earth field). This approximation was done to simplify the geometry of the problem and implement symmetries.
- the holes inside the shielding layers were approximated by square shapes instead of round

¹data analysis toolkit provided by CERN

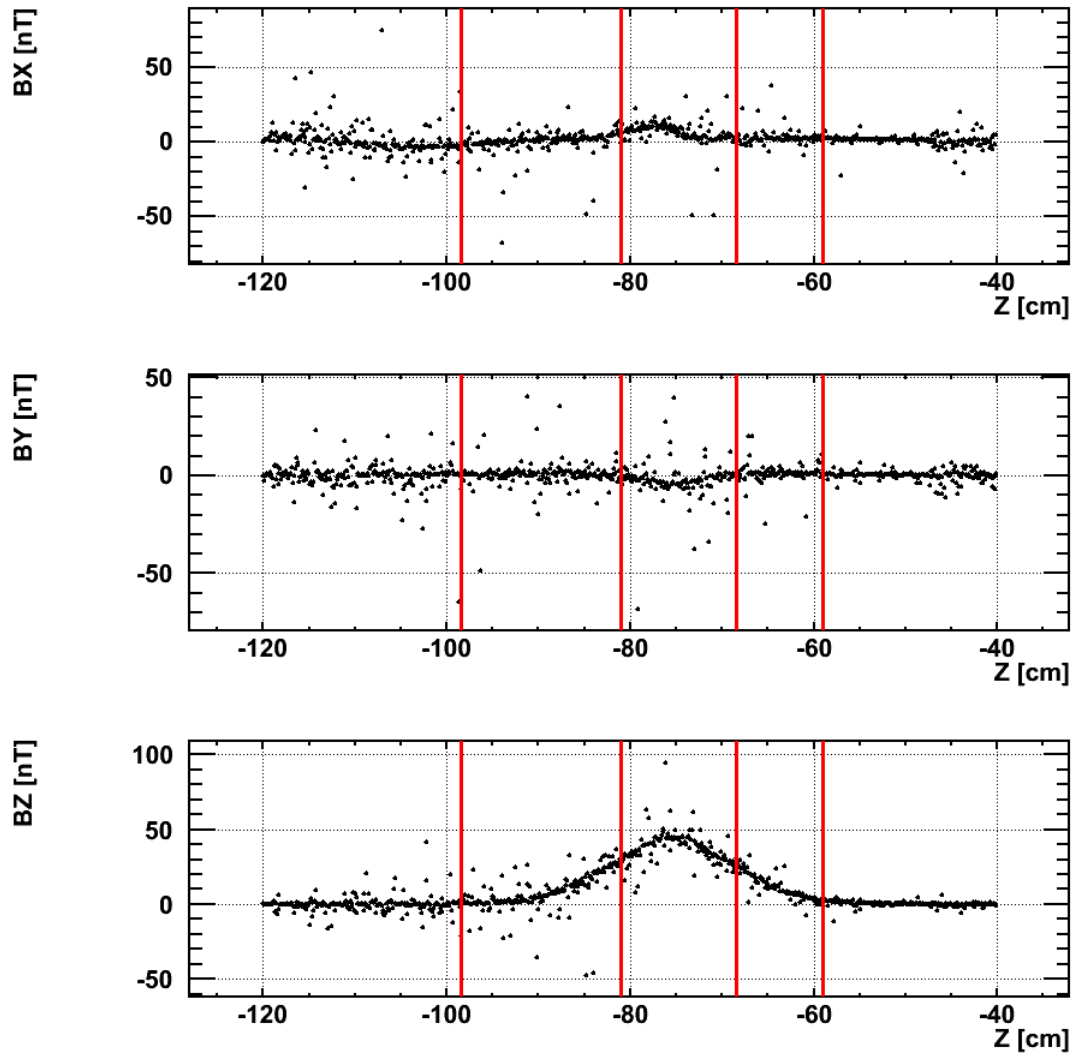


Figure 3.16: Difference of the results of Radia and Maentouch simulations, for the same system composed by a vertical Mu-metal cylinder with the saddle coils pair and the correction solenoid. The difference between the two codes is less than 1 %.

shapes. This was done to simplify the geometry, and to reduce the number of cells. The Mu-metal cylinder is still simulated as it was done with RADIA.

- because of their small contribution inside the vertical guide and to fit with the future measurements, the analyzer and polarizer were not simulated.
- the magnetic susceptibility of the Mu-metal was set to a constant value of $\chi=20000$.
- the system is assumed to have the xOz plane as a plane of symmetry in order to reduce the computation time.
- as a consequence of the previous point, solenoids are approximated by close circular parallel loops (a real solenoid, *i.e.* with a helical shape, breaks the xOz plane symmetry).
- the remnant magnetization was neglected.
- the only coils from the nEDM experiment simulated are the ones which have a real influence on the adiabaticity in the vertical guide: the B_0 coil and the UCN “Kamin” coil.

The complete simulated geometry is shown in Fig. 3.17.

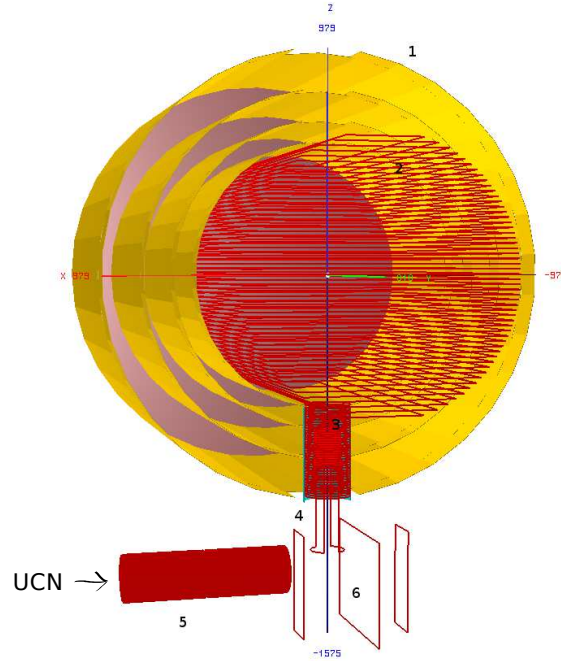


Figure 3.17: Geometry used in MAENTOUCH simulation. (1) Shielding layers. (2) $B_0 \cos\theta$ -like coil. (3) UCN “Kamin” coil. One can see the vertical Mu-metal cylinder behind the coil. (4) Saddle coil pair. (5) Horizontal solenoid. (6) Switch coils.

The field is mainly horizontal in the horizontal guide and mainly vertical inside the precession chamber. A saddle coil pair (number 5 in Fig. 3.19) going through the shield was simulated (field in the x direction) in addition with a solenoid which rotates the spin. A lower adiabaticity region is expected here. The results are shown in Fig. 3.18. The k parameter is larger than 12 everywhere.

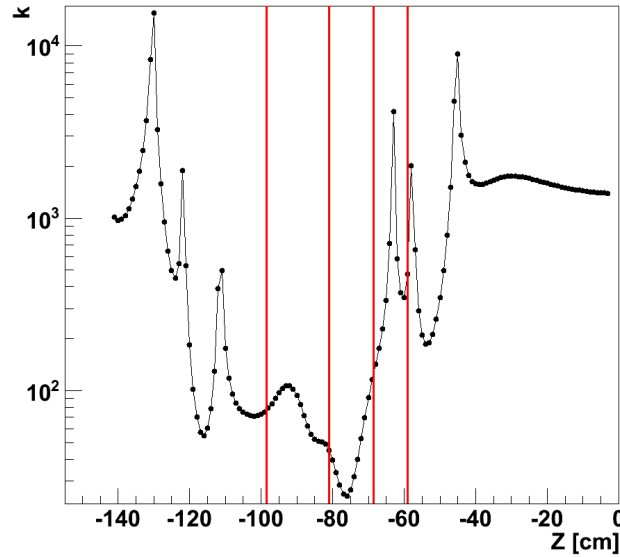


Figure 3.18: Simulated adiabaticity along the vertical guide (at the axis) using MAENTOUCH. The minimum value of the coefficient is larger than the requirement. It is located at the level of the horizontal wires of the saddle coils. The second area with a low adiabaticity factor is located at -120 cm. It corresponds to the horizontal wires of the switch coils. The peaks observed arise from the small gradient between two calculated points, so the adiabaticity can be huge. The critical regions are the ones with a low adiabaticity.

Summary of the new simulated coils

From the results of the simulation, it was decided to add three sets of coils: one on the horizontal guide, one around the switch box and one on the vertical guide. Two solenoids of 25 and 30 cm length, 8.3 cm diameter are used on the horizontal guide. Three rectangular coils are placed directly on the switch: two are 13×30 cm and the middle one is 35×30 cm. Above the switch, a saddle coil (45 cm length, 12.2 cm diameter) has been installed with a three layers correction solenoid. Each solenoid is centered at the end of the saddle coil, they have a diameter of 11.2, 11.3 and 11.4 cm. The total length for the longer one is 15 cm.

3.4.4 Vertical guide mapping

Before testing the new guiding field system with ultracold neutrons, it was decided to perform magnetic field mapping with the coils at their nominal positions. The aim of the measurement was to optimize the currents and positions of the guiding field coils. The adiabaticity parameter value has been calculated inside the vertical guide from the middle of the switchbox to the entrance of the vacuum chamber. The measurement was performed on axis and off axis, using a dedicated experimental setup. The next section describes this setup.

Experimental setup

The new magnetic field measurement is rather different than the first mapping. The sensor used is the same 3-axes fluxgate “Mag-03MC70” from Bartington [82] with a range of 70 μT

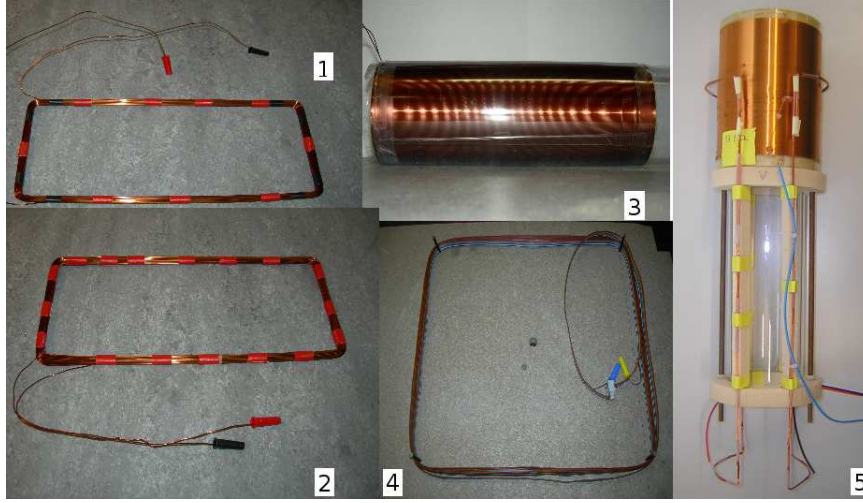


Figure 3.19: New coils setup. (1) First rectangular switch coil. (2) Second rectangular switch coil. (3) Horizontal solenoid. (4) Square switch coil. (5) Saddle coils pair with the correction solenoids.

(Fig. 3.20). A dedicated mapper was built at PSI. It consists in a vertical plexiglass hollow tube in which the probe is placed. The tube can rotate. It is useful for the determination of the probe offset (Sec. 3.4.4). It may be placed at the center of the UCN guide, or at 26 mm from the center for off axis measurements. Eight positions are possible for the off axis measurements, as shown in Fig. 3.21. The reference frame associated to the probe is aligned with the reference frame of the experiment: X axis: from the switchbox to the SC magnet, Y axis: from the removable endcap of the shield to the non-removable endcap of the shield, Z axis: from the switchbox to the precession chamber. A drawing of the mapper on and off axis is presented in Fig. 3.22. The vertical UCN guide was replaced by a dummy glass tube (to avoid damaging the coating). The top of the plexiglass tube is fixed to a polyethylene piece which has the same radius as the internal glass tube. Then the fluxgate can slide along the vertical axis. The system allows mapping the field between the switchbox and the vacuum chamber. The acquisition of the magnetic field is done by the Labview-written SFC coils controller. This allows storing the magnetic field and position at the proper time, chosen manually by the user.

Magnetic field corrections, errors estimation

As shown in Fig. 3.20, the three sensors are separated by a distance of 1.5 cm. The reference sensor for position was chosen to be the Y sensor (the top one). A correction on the position has to be done for the other probe sensors. The fields measured for B_X and B_Z at a height z do not correspond to the field at the real height z . The magnetic field was shifted according to these relations:

$$\begin{aligned} B_X^z &= B_X^{z+3} \\ B_Y^z &= B_Y^z \\ B_Z^z &= \frac{B_Z^{z+1} + B_Z^{z+2}}{2} \end{aligned} \tag{3.21}$$

We have now to calculate the uncertainty of the adiabaticity parameter k . This error depends

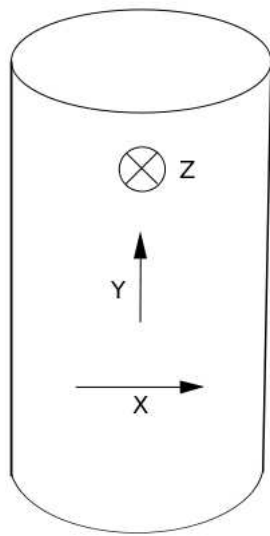


Figure 3.20: Scheme of the end of the 3-axis Bartington fluxgate. Each sensor is at 1.5 cm from the next one.

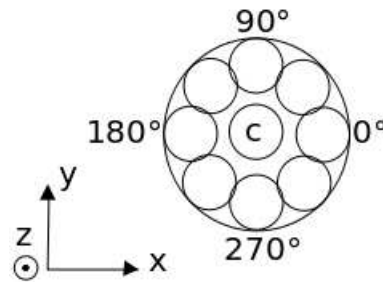


Figure 3.21: Scheme of the possible positions of the fluxgate in the vertical guide.

on errors on the magnetic field components. Three sources of error have been considered for the magnetic field: the error from the probe position in the mapper frame, the error due to the difference between the laboratory frame and the mapper frame and the error from the determination of the probe offsets. The first one includes the error of the sensors position in the fluxgate (± 0.3 mm) and the error of the fluxgate position in the mapper frame, which was estimated to $\delta z = 1$ mm. This error is predominant in high vertical gradient regions. Indeed, the error on the component i of the magnetic field due to the position is:

$$\delta B_{i,pos} = \left| \frac{\partial B_i}{\partial z} \right| \delta z \quad (3.22)$$

The second error comes from the difference between the mapper frame and the experiment frame. Assuming the fluxgate is vertical, an angle ϕ can exist in the xy plane and mix the X and Y components of the field (as shown in Fig. 3.23). Then the measured values are:

$$\begin{aligned} B_X^{meas} &= B_X^{real} \cos \phi + B_Y^{real} \sin \phi \\ B_Y^{meas} &= B_Y^{real} \cos \phi - B_X^{real} \sin \phi \end{aligned} \quad (3.23)$$

It was not possible to determine this angle because of the mapper geometry which unable us to determine the offset. ϕ is different for each measurement. Only an error can be estimated,

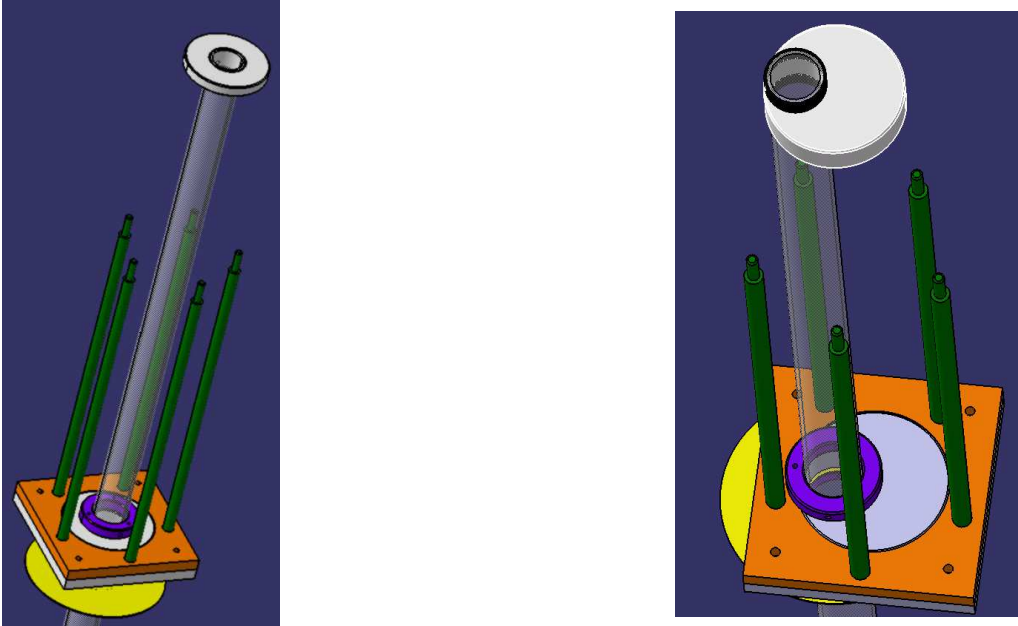


Figure 3.22: Drawing of the mapper used, in on axis configuration (left side), and off axis configuration (right side). The orange part is fixed to the switchbox with five aluminum bars. The plexiglass tube is going through the UCN dummy guide.

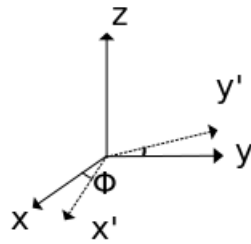


Figure 3.23: Definition of the mixing angle ϕ in the xy plane.

by measuring the field at the same location several times in a place where the X component is large comparing to the Y component. We found $\delta\phi = \pm 4^\circ$.

$$\delta B_{X,ang} = (B_X^{meas} B_Y^{meas}) \begin{pmatrix} \cos \delta\phi \\ \sin \delta\phi \end{pmatrix} \quad (3.24)$$

$$\delta B_{Y,ang} = (B_X^{meas} B_Y^{meas}) \begin{pmatrix} -\sin \delta\phi \\ \cos \delta\phi \end{pmatrix} \quad (3.25)$$

The last error comes from the determination of the fluxgates offsets due to temperature variations, mechanical stress or electric noise [83], and thus can vary with time. To determine the offsets on the X and Y sensors, the fluxgate was placed at the center of the vertical solenoid. Then the probe height was blocked. In the xy plane, the probe was rotated by 0, 90, 180, 270 and 360 degrees, using different currents in the vertical solenoid. In our case, when the fluxgate is placed inside a coil which produces a field B_C , the field read by the fluxgate (X and Y components) is:

$$B_M^0 = B_C + B_{off} + B_{res} \quad (3.26)$$

B_M^0 is the field read by the fluxgate at the position 0, B_{off} is the offset of the fluxgate and B_{res} is the residual field. If the fluxgate is turned by 180° , the read field is:

$$B_M^{180} = -B_C + B_{off} - B_{res} \quad (3.27)$$

Then, the offset can be determined:

$$B_{off} = \frac{B_M^0 + B_M^{180}}{2} \quad (3.28)$$

Rotations by 90° and 270° at different currents in the vertical solenoid were used to estimate an error on the offset (it is possible with two positions and three currents to have six values of the offset). It was found: $\delta B_X = 105 \pm 30$ nT and $\delta B_Y = 110 \pm 30$ nT. This procedure does not allow the determination of the offset on the Z component (the mapper allows us to turn only around the Z axis). To evaluate δB_Z , the fluxgate was removed from the mapper and placed into a magnetic shield horizontal cylinder. The Z component of the field was measured and then the Z probe was rotated by 180 degrees and placed at the same position (the aim is to do the change $Z \rightarrow -Z$). Then the previous procedure can be applied. The offset found was $\delta B_Z = 120 \pm 30$ nT. The error on any component of the field is:

$$\delta B_{off} = 30 \text{ nT} \quad (3.29)$$

The total error on each component is the sum of the three error sources:

$$\begin{aligned} \delta B_X &= 30 \text{ nT} + (B_X B_Y) \begin{pmatrix} \cos 4^\circ \\ \sin 4^\circ \end{pmatrix} + \left| \frac{\partial B_X}{\partial z} \right| \times 1 \text{ mm} \\ \delta B_Y &= 30 \text{ nT} + (B_X B_Y) \begin{pmatrix} -\sin 4^\circ \\ \cos 4^\circ \end{pmatrix} + \left| \frac{\partial B_Y}{\partial z} \right| \times 1 \text{ mm} \\ \delta B_Z &= 30 \text{ nT} + \left| \frac{\partial B_Z}{\partial z} \right| \times 1 \text{ mm} \end{aligned} \quad (3.30)$$

Then all these errors were propagated to the error on k using MATHEMATICA. A problem appears with this formulation for the large values of B_X and k (typically before entering in the shielding). k is large in the region where the gradient of the transversal component is small. The unknown ϕ angle leads to a larger error on B_X and B_Y , so a large error on the gradients too. As a consequence the error on k is larger than k itself. The reproducibility measurement was tested and, under the same running conditions, k is stable to about 25 % in the critical region. That is why the error bars on k in all the plots of this chapter were artificially set to 25 % in the divergence region. This does not happen in regions with small values of k , the uncertainty plotted in these regions are the one calculated from the errors on the magnetic field components.

Analysis

This section describes the results of the mapping. The aim of the mapping was to test several points (the ones described in Sec. 3.4.1). The best configuration chosen for the currents is:

- 50 mA for the horizontal solenoids
- 100 mA for the switch coils
- 30 mA for the vertical saddle coils
- 2 mA for the correction solenoid coil (depending polarity of B_0).
- 20 mA for the UCN Kamin coil (depending polarity of B_0).

Comparison between Maentouch simulations and measurements Measurements were done to confirm the approximations made in the simulations. A mapping was done at the center of the UCN guide. The results (components of the field) are shown in Fig. 3.24.

In the small adiabaticity region, the relative difference between measurements and simulation is less than 5 % for the Z component, and less than 2 % for the X component. The difference for the Y component may comes from how the simulated system was simplified and also from the alignment of the mapper. It was assumed that the xOz plane is a symmetry plane for the system (only half of the magnetized pieces are generated, in this case a factor 4 is gained in computation time). As a consequence, the B_y field in this plane is zero. Furthermore, it was assumed that the mapper reference frame was the same as the experiment reference frame, which is not completely right. Finally, this comparison was done assuming no other magnetic element than the shield and no initial magnetization of magnetic pieces. This assumption is not justified in reality, and was checked by doing a measurement of the remnant field. It has revealed a region where a 2000 nT magnetic field is present. This corresponds to some magnetized screws at the top of the switch. These screws were changed to non magnetic screws for measurement with UCN. The measured adiabaticity parameter was also compared to the simulated one, as shown in Fig. 3.25. In the small adiabaticity region, the simulation is consistent with the measurement.

Because of the poor homogeneity of the magnetic field inside the UCN guide (especially close to the horizontal wires of the saddle coils), simulations were also done off axis and compared with measurements. Two positions are shown in Fig. 3.26.

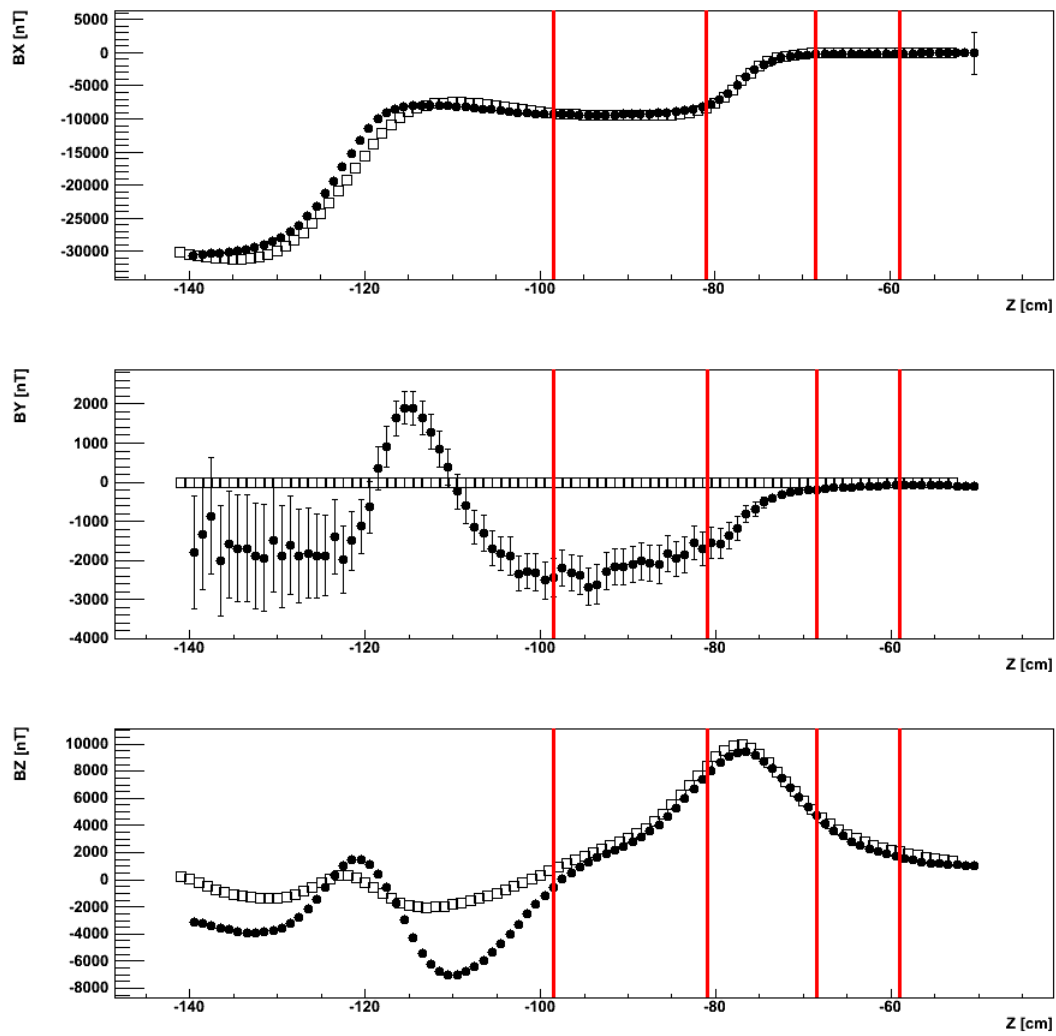


Figure 3.24: Comparison between a magnetic field mapping (black dots) and the simulation (empty squares) of the three components of the magnetic field.

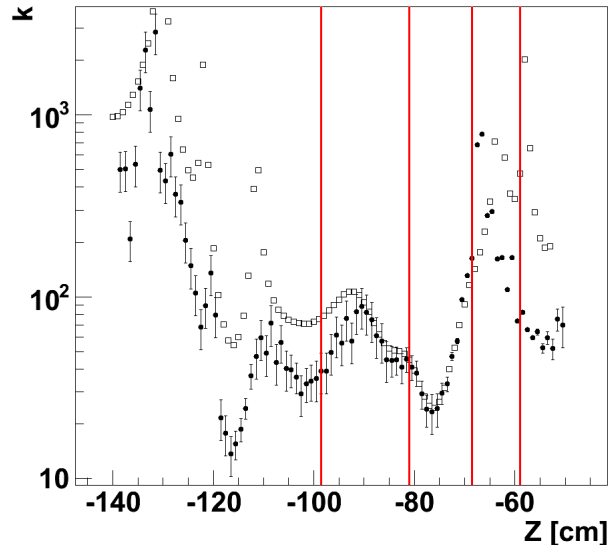


Figure 3.25: Comparison of the adiabaticity parameter between a magnetic field mapping (black dots) and the associated simulation (empty squares)

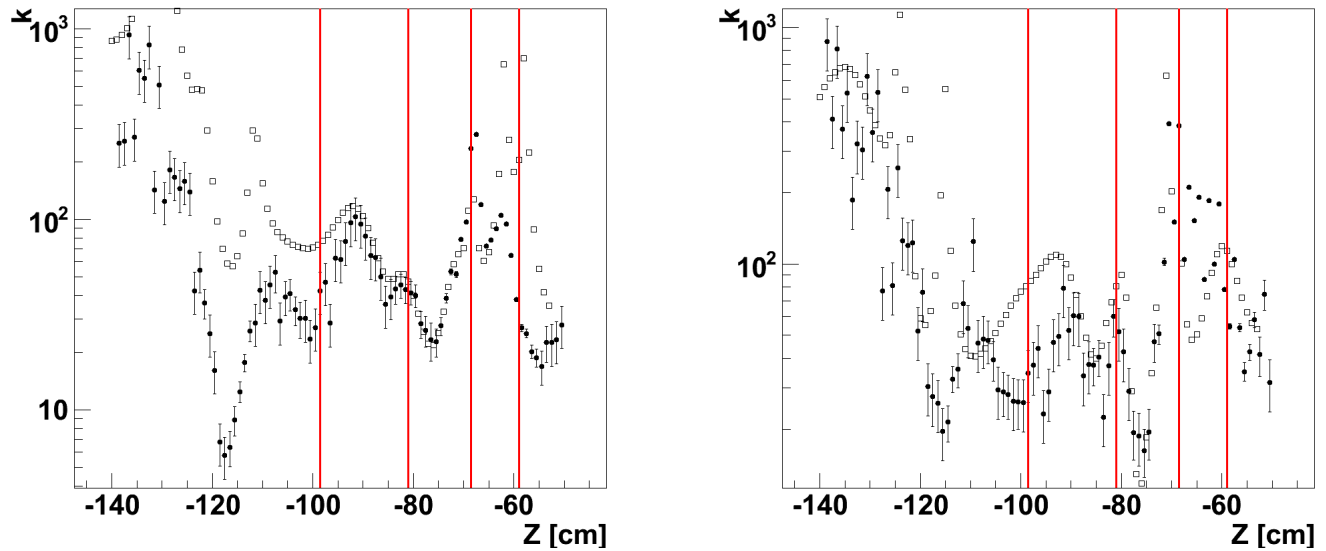


Figure 3.26: Comparison of the adiabaticity parameter between a magnetic field mapping (black dots) and the associated simulation (empty squares) for two off axis places: where the contribution of the field generated by the saddle coils is the smallest (left picture, position 90°) and where the contribution of the field generated by the saddle coils is the largest (right picture, position 180°)

Comparison B_0 up/down This point was tested by measuring the magnetic field for both B_0 field configurations. The results are shown in Fig. 3.27. Despite some differences, the small values of the adiabaticity parameter is larger than 12 in both cases, the two values are in agreement within the error bars. The system is efficient for both polarities of the B_0 coil. This point was tested with UCN and is discussed in Chap. 5.

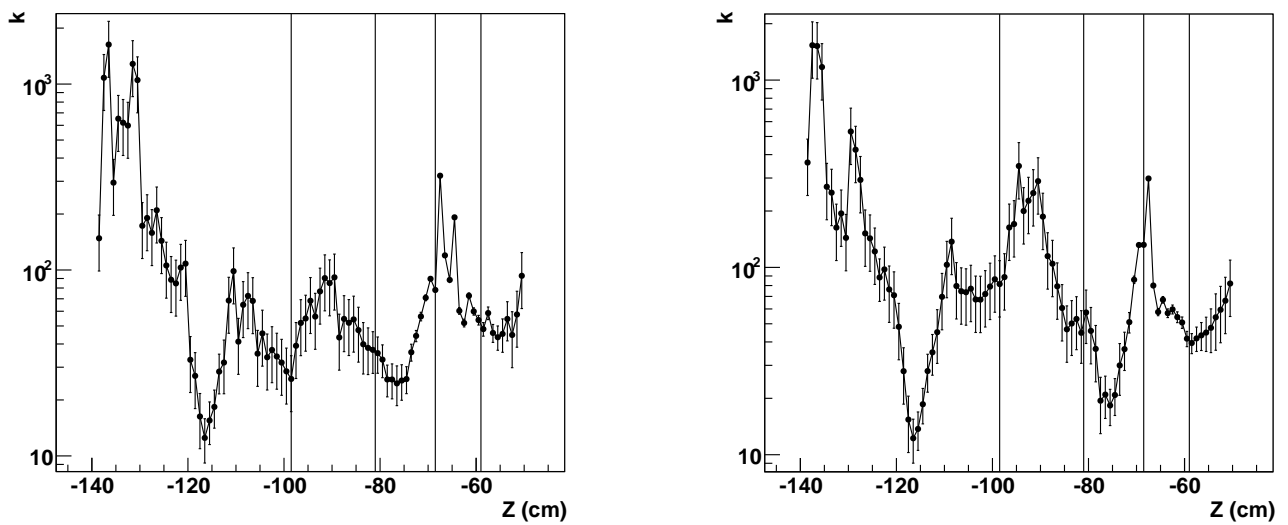


Figure 3.27: Adiabaticity plots for B_0 up (left) and B_0 down (right). The same behavior is observed for both polarities: the minimum value of k is the same.

Comparison on/off axis This point was studied by measuring the adiabaticity parameter at different places inside the vertical guide. The mapper allows to scan 9 different positions: at the center, and at a distance of 26 mm from the center at 8 different angles (in the xOy plane, the angle corresponds to 0° , 45° , 90° , 135° , 180° , 225° , 270° and 315°). Because of the symmetry of the problem, we are supposed to find the same minimal adiabaticity for two angles which are symmetric with respect to the xOz plane. This point was checked. The adiabaticity is the same according to the error. The two different angles are shown in Fig. 3.28.

The results are summarized in Table 3.6. All the values are larger than the required value 12.

Effect of the UCN chimney (UCK) coil This point was tested by varying the current inside the UCN chimney coil. In Fig. 3.29, the adiabaticity parameter k is larger than 10 everywhere if the UCN chimney coil is used with a current of 20 mA. Otherwise, the value is around 5 immediately after the internal layer of shielding (-58 cm). This could be corrected by the saddle coil by lifting it up by some cm or by using the UCK coil. The field of this coil helps improving the adiabaticity between the most internal layer of shielding and the one just after. The UCK coil is also used to correct the gradients inside the precession chamber. The use of this coil with the same polarity as the correction solenoid helps to correct gradients and improves the adiabaticity (next paragraph).

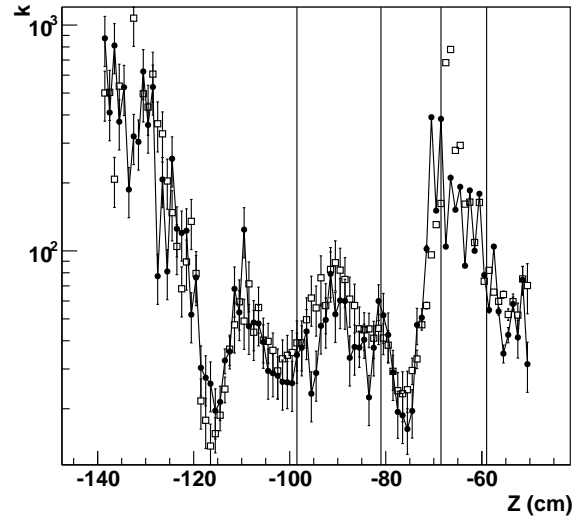


Figure 3.28: Adiabaticity parameter as a function of the vertical position z . Open squares correspond to measurements performed on axis, black dots to measurements performed off axis (26 mm from the center, angle: 315°).

Table 3.6: Minimum adiabaticity parameter in the expected low adiabaticity region.

Angle	Minimum k	error
Center	20	4.5
0°	23	4.4
90°	21.5	5
180°	23	3.8
270°	21	4
315°	18.4	4

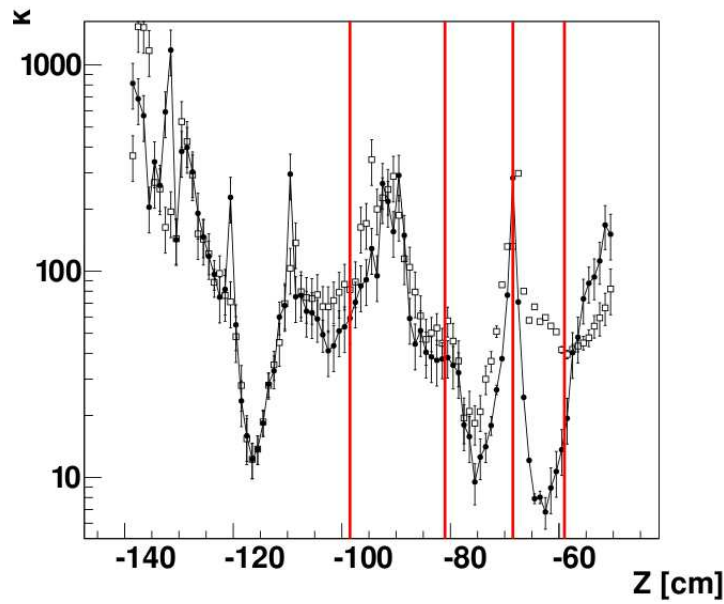


Figure 3.29: Effect of the UCK coil on the adiabaticity. Black dots: no UCK coil. Open squares: UCK coil at 20 mA. With a current of 20 mA, the adiabaticity near the internal shielding layer is larger by a factor of 10.

Effect of the stray field of the guiding field coils on the precession chamber This point was not tested during this measurement campaign because the Cs magnetometers were not available during the measurement and because the range of the mapper does not allow the mapping close to the precession chamber with the fluxgate. A former measurement was done with the rough mapper. It was possible to estimate the horizontal gradient created by the guiding field coils system. It was shown that the use of the correction solenoid along with the UCK coil in the same polarity reduces the gradient by a factor of 10. A precise measurement with Cs magnetometers was also done in March 2011. Two maps were done, with and without the guiding field coils. The difference of these two maps is shown in Fig. 3.30. The magnetic field modulus gradients can be read from this map. The GF coils are creating a maximum vertical gradient of 10 pT/cm and a maximum horizontal gradient of 5 pT/cm. These gradients can be compensated for by the trim coils.

Improvement of the influence of external fields A problem may occur close to the switch coils if the SFCs are used in the regular current configuration (Chap. 2). In that case, the field gradient is large close to the horizontal wires of the coils. As a result, the adiabaticity parameter is around 10 ± 4 depending where we are measuring. In order to improve the situation another magnetic field source may be added to increase the horizontal magnetic field at this place or alternatively the field created by the horizontal wires of the switch coils may be reduced. Two possibilities have been investigated: a boost in the $-X$ direction using the X coils of the SFC has been performed and a shield made of a Mu-metal cylinder has been set around the horizontal wire. At this place (close to the wires), the minimum value of k is 12. Using the SFCs, with a current of 10 A in the X coils, k rises to 19. With 15 A, k increases up to 40. Using the Mu metal cylinder, k rises to 30 in this area (Fig. 3.31). This possibility will be used, but a recent

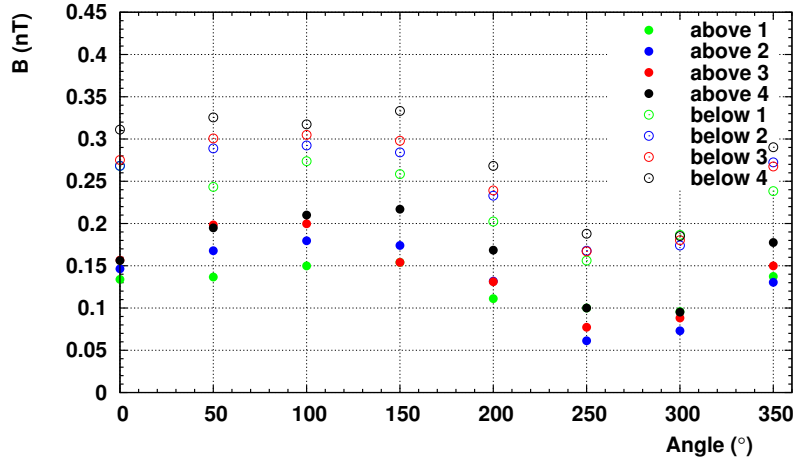


Figure 3.30: Stray field of the Guiding Field coils measured in the precession chamber using the Cs magnetometer. The full squares correspond to Cs magnetometers above the precession chamber, the empty squares to Cs magnetometers below the chamber. The abscissa axis is a rotation angle (the Cs magnetometers can rotate around the Z axis).

choice to change the analyzer to a more powerful one (Chap. 5) is reducing this effect. Indeed, a $30 \mu\text{T}$ mainly horizontal field is added at this position which decreases the angle between the magnetic field and the horizontal axis.

Another improvement was done after the mapping campaign. Even if the measured adiabaticity is above the requirement, it was not possible to measure very close to the edges of the vertical UCN guide (due to the thickness of the fluxgate). To avoid depolarization when UCN strikes the guide close to the wires, it was decided to increase the radius of the saddle coils within the shield. Figure 3.32 shows the new design. Furthermore, this design increases the adiabaticity to a minimal value of 20 within this region.

Figure 3.33 gives the comparison of the adiabaticity at the center of the vertical guide with the first setup and the improved setup (new analyzer associated to the modified saddle coil pair). The analyzer boosts the adiabaticity close to the horizontal wires of the rectangular coils, and the modified saddle coil pair increases the adiabaticity parameter in the small adiabaticity region by a factor of 2.

3.5 Conclusion

Magnetic field measurements were done to quantify the effect of the new guiding field coils, on axis and off axis and for the B_0 up and B_0 down configurations. Since the coils are close to the guide surface, more inhomogeneities were expected off axis than on axis as can be seen in Fig. 3.28. The adiabaticity parameter k is acceptable on and off axis if all the coils are used. As a summary, it was found that k is larger than 12 everywhere in the vertical guide whatever the B_0 field configuration (Fig. 3.27) which will be sufficient to maintain the UCN polarization from the SCM to the precession chamber. Furthermore, the system was upgraded with a modification of a coil and the addition of a new analyzer. The efficiency of the guiding field was tested with a MC code by the computation of the Bloch equations in Chap. 4, and by a measurement with

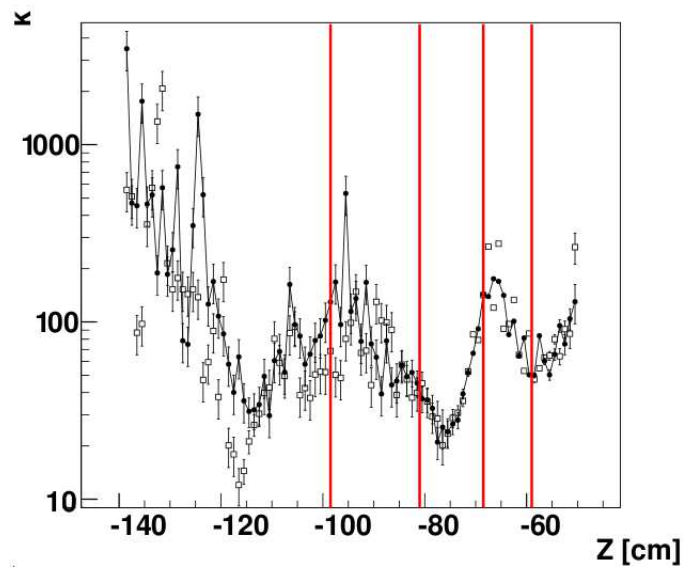


Figure 3.31: Effect of the Mu-metal cylinder placed around the horizontal wire of the switch coils. Black dots: no shield. Open squares: shield used. The adiabaticity parameter is three times higher when the shield is used.

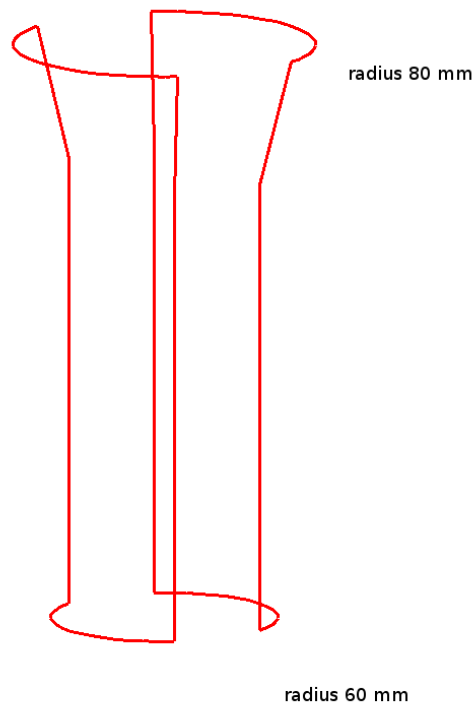


Figure 3.32: Design of the new saddle coil. The top radius was enlarged by 2 cm.

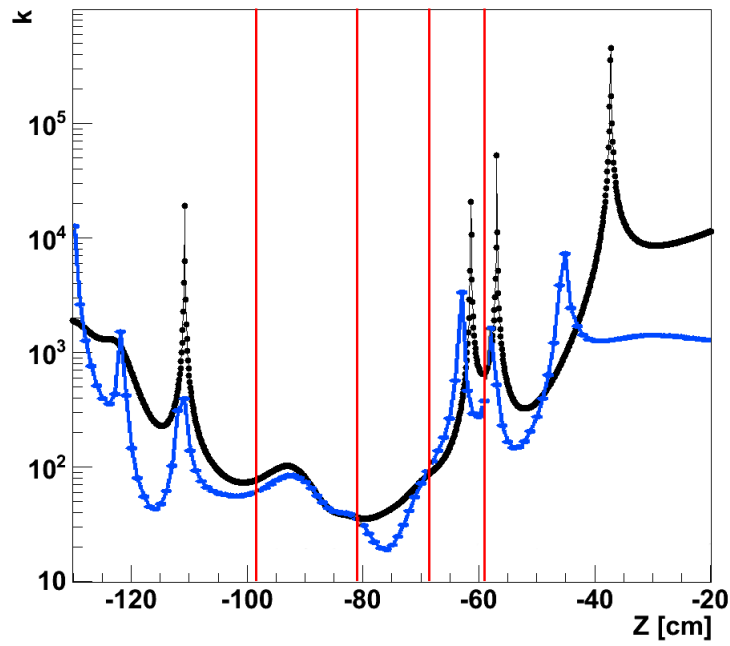


Figure 3.33: Adiabaticity parameter at the center of the vertical guide with the first setup (blue line) and the improved setup (new analyzer associated to the modified saddle coil pair, black line).

UCN in Chap. 5.

CHAPTER

4

UCN losses and depolarization

4.1 Introduction

This chapter focuses on simulations carried out to estimate the depolarization rate and UCN losses within the apparatus, for the different phases of a measurement cycle. Because of the complex geometry of the apparatus and that the details of the forces applied to the neutrons (strong, magnetic) are not known, analytic calculations of the depolarization process are not possible. A dedicated Monte Carlo code has been developed and used for this purpose. This chapter will first describe the code and the different input parameters of the simulation. Then, results on the UCN transport, storage and depolarization will be discussed.

4.2 The Monte Carlo simulation

The Monte Carlo (MC) code used in this chapter is named GEANT4-UCN [84], it is an extension of the GEANT4 [85, 86] simulation package developed at Cern. GEANT4 is well adapted to complex geometries, but it was mainly developed for high energy physics (at the MeV and GeV scales). Additional features have been added in order to use it for the UCN energy scale (neV). They are implemented in the GEANT4-UCN code. A list of them is presented in the next paragraph.

4.2.1 Physical context of the UCN simulation

In the GEANT4-UCN code, a new particle, called “UCN”, has been defined. It has the same mass and lifetime as the GEANT4 neutron, and is affected by gravity. In GEANT4-UCN, gravity is represented as a constant and homogeneous electric field since the physical process of gravitation does not exist in GEANT4. The value of the gravity potential is set to 102 neV.m^{-1} .

Treatment of wall collisions

Furthermore, neutron scattering processes are implemented. As described in Sec. 1.2.2, the reflection and transmission coefficients are calculated according to Eq. (1.17). For this process, the relevant parameters are the Fermi potential V_F and the kinetic energy. The UCN which are lost during a reflection are described with a probability that depends on the kinetic energy, according to Eq. (1.19). In that case, the relevant parameter is η , the ratio between the imaginary part W and the real part V of the Fermi potential:

$$\eta = \frac{W}{V} \quad (4.1)$$

The loss probability per bounce $\mu(E_\perp)$ given in Eq. (1.19) can be rewritten as a function of η :

$$\mu(E_\perp) = 2\eta \sqrt{\frac{E_\perp}{V - E_\perp}} \quad (4.2)$$

In case of transmission the relevant parameter is the absorption cross section of thermal neutrons σ_{abs}^{th} [87]. The cross section is energy dependent [88] and is rescaled to UCN energies following the $1/v$ law:

$$\sigma_{abs}^{UCN} = \sqrt{\frac{E_{th}}{E_{UCN}}} \sigma_{abs}^{th} \quad (4.3)$$

The UCN reflection is either specular or diffuse. For the specular reflection the incident angle is equal to the angle of reflection. For the diffuse reflection, the “reflected” angle is distributed over the optical Lambert’s law. The amount of diffuse reflection is given by the diffuse reflection probability p_{diff} . Usual values are between 1 and 10%. The most common way to study the depolarizations due to wall collisions is the probabilistic approach. A probability β of spin flip per bounce is defined. This parameter is an input to the simulation.

The UCN spin treatment

Two different means were used in order to study the depolarization processes of the UCN. The depolarization due to wall collisions was studied using a flag (up or down, $S = \pm 1$). Thus, when a neutron is depolarized during a wall collision, the flag is reversed. For the depolarization calculations due to the magnetic field inhomogeneities, the spin is simulated using a 3 dimensional vector $\vec{S} \equiv (S_x, S_y, S_z)$ and the Bloch equations are integrated (Sec. 4.5).

4.2.2 Materials properties

Most of the materials used in the nEDM experiment (and therefore in the simulation) have a large Fermi potential and low depolarization and losses probabilities. Their physical properties are summarized in Table 4.1. The insulating ring is made of polystyrene with a deuterated PolyStyrene (dPS) coating. The two electrodes are made of aluminium and coated with Diamond-Like Carbon (DLC). The UCN guides are glass tubes with a coating of a nickel-molybdenum alloy (85% Ni, 15% Mo). The analyzing foil is an aluminium substrate with a deposited layer of iron. Finally, the detector is a glass scintillator doped with ^6Li . A value of $1 \cdot 10^{-6}$ for β means that the coefficient is not known for this material. This is the case of the iron and the ^6Li scintillator. This value is chosen because it is a typically measured value for other materials. A probability of diffuse reflection of 10% is chosen for the chamber and 1% for the guides.

Table 4.1: Physical properties of the materials used in the simulation.

Material	V_F (neV)	β ($\times 10^{-6}$)	η ($\times 10^{-5}$)	p_{diff} (%)	σ_{abs}^{th} (barn)
dPS	162	0.7	4.5	10	0.0047
DLC	260	3	18	10	0.0049
NiMo (85/15)	220	2.5	7.7	1	4.49
Al	54	10	2.25	1	0.231
Fe	210	1	8.5	1	2.56
^6Li scintillator	84.8	1	10	1	14.7

4.3 Input parameters

4.3.1 The simulated experimental setup

The geometry from the tank up to the detector has been reproduced within the GEANT4 simulation. Figure 4.1 depicts the geometry. This includes:

- the UCN storage tank near the source.
- the 190 mm diameter glass guides used for the UCN transport from the tank up to the experiment.
- the SC polarizer.
- the guide adapter from 190 mm down to 80 mm.
- the 80 mm diameter glass guides including the bent guide used within the switch for filling.
- the precession chamber (insulating ring and the two electrodes).
- the UCN shutter of the precession chamber.
- the analyzing foil.
- the UCN detector.

Nevertheless, some approximations were done in order to simplify the simulations. The UCN tank has been considered as a rectangular box instead of its real complex geometry. The source guides are only assumed to be made of glass with a NiMo coating, *i.e.* the stainless steel tubes have been replaced by glass tubes. The 190-80 mm adapter was simulated using a cone instead of its real shape.

4.4 Depolarization due to wall collisions

Each phase of the experiment: filling, storage and emptying, was simulated. Simulations were done in order to estimate the depolarizations due to wall collisions, and the performance of the chamber to store UCN.

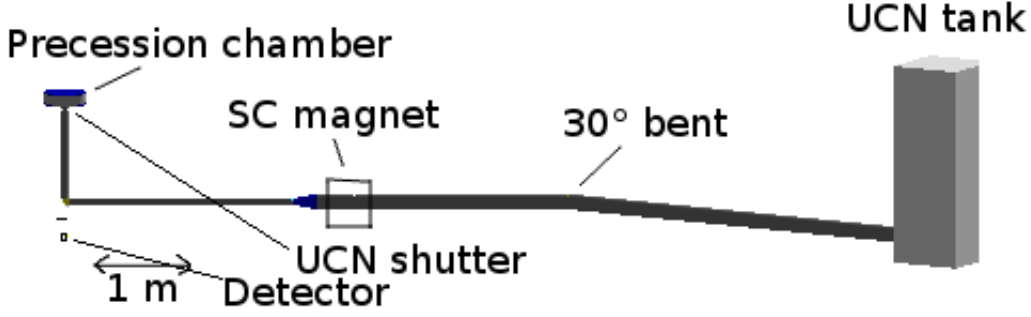


Figure 4.1: Scheme of the geometry used in the MC simulation.

4.4.1 Filling phase

The apparatus is filled with UCN during a time τ_{fill} which depends on the performance of the system to store UCN and do not depolarize them (explanations are given in Sec. 5.6.2). According to previous simulations from Ref. [89], the filling time was set to 40 s. UCN are generated at the bottom of the tank at $t = 0$, and the UCN shutter is closed at $t = \tau_{fill}$.

UCN velocity and position distributions

A first simulation was performed with the UCN generated within the UCN tank, and then propagated up to the apparatus. From an initial number of 10000 UCN, only 2 were stored within the precession chamber at $t = \tau_{fill}$. Most of them were staying within the UCN tank leading to a large and useless computation time. In order to increase the number of stored UCN while reducing the computation time, UCN were generated at the horizontal guide just before the 30° bent. In this way, the volume accessible to the UCN is reduced by 90 %. UCN were generated uniformly from a section of the UCN guide. Since no velocity measurement was performed with the apparatus at PSI, it was not possible to use an experimental velocity distribution as an input parameter of the simulation. The neutron velocity spectrum within the UCN tank can be generated by using the velocity spectrum of very-cold neutrons as input [89]. In this case, a large amount neutrons have velocities above the critical velocity of the tank. The main limitation on the UCN velocity spectrum comes from the walls of the tank and the UCN guides. The velocity component parallel to the UCN guide is generated on a Gaussian centered on the critical velocity of the UCN guide. A cut-off is applied above the critical velocity in order to not generate UCN which will not be storable. UCN were propagated within a 3740 mm guide which is the distance between the 30° bent and the entrance of the switchbox. It was shown that no UCN with an initial axial velocity larger than 8.5 m/s were detected, slightly higher than the critical velocity of the guide (6.5 m/s). This gives a limit on the applied cut-off. UCN are generated in the direction of the apparatus in order to increase the statistics. The two other velocity components, due to the geometry of the guides, are generated over a Gaussian restricted by the Fermi potential of the guide. The distribution of the velocities is shown in Fig. 4.2.

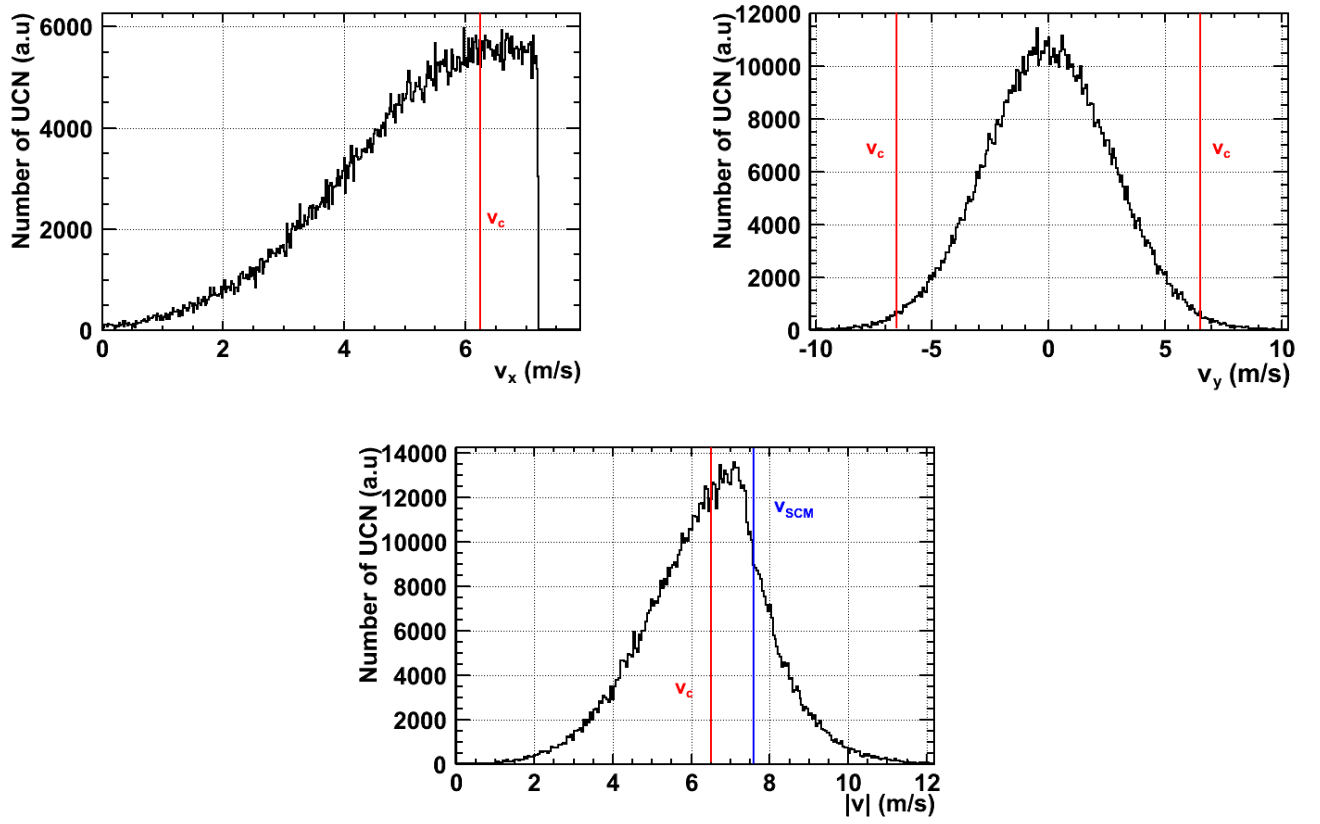


Figure 4.2: Initial velocity distribution of UCN for the filling phase. Left up panel: axial component. Right up panel: transversal component. Down panel: modulus. The critical velocity of the NiMo v_c and the equivalent velocity to the SCM magnetic field v_{SCM} are depicted.

Polarization efficiency

The shutter of the UCN tank is simulated by a perfect absorber. Thus, the UCN which are going toward the UCN tank are removed from the simulation. The polarizer is simulated by a step potential for which the height depends on the spin state (Sec. 1.2.2). The initial beam is fully depolarized. Then the number of UCN with a spin state that cross the polarizer potential (called hereafter “right spin state”) and UCN with a spin state which is not supposed to cross the polarizer potential (called hereafter “wrong spin state”) are counted at the entrance of the switchbox. The polarization efficiency of the SCM is defined as:

$$P = \frac{N_r - N_w}{N_r + N_w} \quad (4.4)$$

where N_r denotes the number of right spin state counted neutrons and N_w the number of wrong spin state counted neutrons. This efficiency is found to be:

$$P > 97.5\% \quad (4.5)$$

The loss of efficiency is due to wrong spin UCN which energy is larger than the potential step of the magnet. This number is the most pessimistic value which can be obtained. Indeed, the velocity spectrum was cleaned only within the horizontal guide before arriving on the switch, at a distance of 3740 mm. The softening of the spectrum within the UCN tank and the first guide were not considered. Figure 4.3 shows the velocity spectrum for the detected UCN and for the UCN with wrong spin state component (red curve). As expected, this component corresponds to UCN with an energy larger than the potential step of the polarizer.

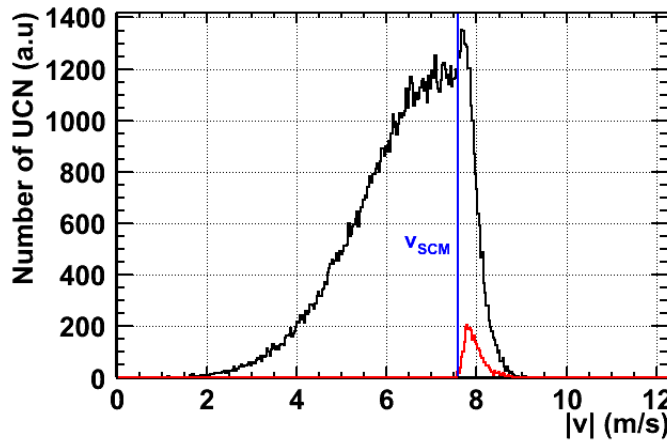


Figure 4.3: Velocity distribution at the entrance of the switchbox. The black line depicts the full UCN beam, and the red line the non-polarized fraction.

Depolarizations due to wall collisions during the filling phase

The number of UCN depolarized during the filling phase has been estimated taking into account only the depolarization process due to wall collisions. From a sample of 100000 UCN, the spins of 57 UCN were flipped during filling. The results are summarized in Table 4.2.

Table 4.2: Summary of the depolarization estimates during the filling phase after a time τ_{fill} .

initial UCN	Spin flip UCN	UCN in the apparatus at $t = \tau_{fill}$	UCN in the chamber at $t = \tau_{fill}$	Spin flip UCN in the apparatus at $t = \tau_{fill}$
100000	57 ± 8	50 ± 7	34 ± 6	0

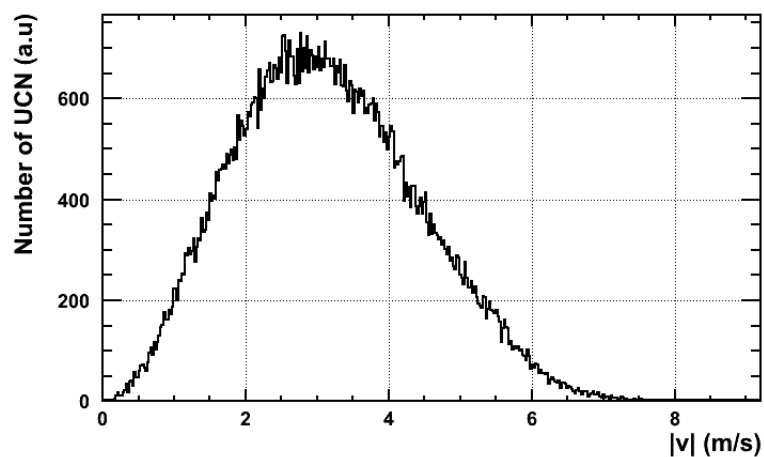
The errors are statistical. Errors on the values of β were not taken into account. $0.06 \pm 0.01\%$ of the UCN are flipped.

4.4.2 Storage phase

Once the UCN shutter is closed, UCN are stored within the chamber for a precession time T . During this phase, the depolarization probability due to wall collision has been extracted.

Velocity and position distributions

The velocity distribution used in this part comes from a previous work [90] which used a similar geometry as input. Such a distribution was chosen due to the small statistics obtained at the end of the filling phase. In order to increase statistics, the distribution corresponds to a softened spectrum, *i.e.* obtained after a storage time of 100 s. Indeed, UCN with energy larger than the Fermi potential are mostly lost in the first seconds of the storage period [91]. The three velocity components were assumed to be Gaussian. UCN are generated uniformly within the volume of the chamber, the density gradient induced by gravity was not taken into account. The distribution of the velocity modulus is shown in Fig. 4.4.

**Figure 4.4:** Initial velocity distribution for the storage and emptying phases.

UCN losses

UCN were stored during different storage times, and the number of UCN within the chamber as a function of time has been studied. The three sources of UCN losses (reflection losses, transmission and beta decay) were included. The results are shown in Fig. 4.5.

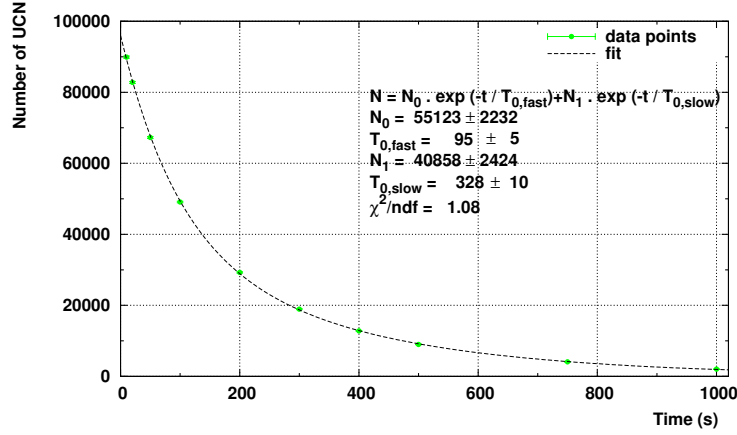


Figure 4.5: Number of UCN within the chamber as a function of the storage time T .

A fit with two exponentials was used. The first exponential describes the fast UCN component with energies close to the wall Fermi potential and the second exponential accounts for the slower component. The two T_0 times obtained are: $T_{0,fast}=95\pm5$ s and $T_{0,slow}=328\pm10$ s. These values are in the same range as the measured ones (Sec. 5.6.3: $T_{0,fast}=53\pm21$ s and $T_{0,slow}=180\pm55$ s). The difference may be explained by the used velocity spectrum in the simulation which was already softened. This leads to a larger simulated $T_{0,fast}$ time. Furthermore, impurities and leaks were not included, which leads to a larger simulated $T_{0,slow}$ time.

Depolarizations due to wall collisions

During the storage phase, the spin of 148 UCN were flipped for a total of 49100 UCN still in the chamber. The results are summarized in Table 4.3.

Table 4.3: Summary of the depolarization estimates during the storage phase ($t = 100$ s).

initial UCN	Spin flip UCN	UCN in the chamber at $t=100$ s	Spin flip UCN in the chamber at $t=100$ s
100000	176 ± 13	49100 ± 220	148 ± 12

This corresponds to $0.30\pm0.03\%$ spin flipped UCN for this phase.

4.4.3 Emptying phase

After a storage time T , the UCN shutter is opened and the UCN are counted for 40 s (typical counting time).

Velocity and position distributions

The velocity and position distributions of the storage phase were also used for the emptying phase.

Depolarizations due to wall collisions

During this phase, the spin of 74 UCN were flipped, for a total of 63266 detected UCN. The results are shown in Table 4.4.

Table 4.4: Summary of the depolarization estimates during the emptying phase.

initial UCN	Spin flip UCN	Detected UCN	Detected Spin flip UCN
100000	117±11	63266±252	74±9

This corresponds to $0.12 \pm 0.02\%$ spin flipped UCN for this phase.

4.4.4 Conclusion

A small amount of UCN (less than 0.3%) are depolarized during each phase. Summing the depolarizations occurring during the three phases, the asymmetry due to depolarizations on wall collisions was estimated to be:

$$\mathcal{A} = 99.2 \pm 0.1\%. \quad (4.6)$$

Regarding the measured experimental values [61] ($\mathcal{A} \approx 85\%$), we can consider that the depolarizations due to collisions are negligible.

4.5 Depolarization due to field inhomogeneities

4.5.1 Formalism of the method

Spin precession calculations have been performed in order to estimate the UCN depolarizations due to magnetic field inhomogeneities. As described in Chap. 1, the spin precession of a particle within a magnetic field can be described with the Bloch Equations:

$$\frac{d\vec{P}}{dt} = \gamma_n \vec{P} \times \vec{B} \quad (4.7)$$

The magnetic field has been calculated using the MAENTOUCH code (Chap. 3). The optimal guiding field configuration is chosen. UCN trajectories have been simulated within the apparatus with the GEANT4-UCN code. Then the spin precession has been calculated along the trajectories knowing the calculated magnetic field. The Bloch equations have been integrated for 100000 UCN along their trajectories. Finally, the mean polarization has been extracted.

The optimization of the integration of the Bloch equations have been performed using the formalism developed by Seeger and Daemen [92]. The spin \vec{P} is decomposed into two vectors

$\vec{\alpha}$ (parallel to \vec{B}) and $\vec{\beta}$ (orthogonal to \vec{B}). Only the spin component $\vec{\beta}$ undergoes precession. Then the z axis is chosen to be aligned along \vec{B} . In this case, the precession problem is reduced to a calculation in the xOy plane. Then the equations are integrated along the trajectory of the UCN using an adaptive step size fourth-order Runge-Kutta procedure [93].

The initial velocity and position distributions used in this paragraph are defined in Sec. 4.4.2. The three components of the magnetic field calculated with MAENTOUCH are known along the neutron path at the mm level. Each point at z constant is fitted by harmonic polynomials. Thus, a function is generated for each z . The tolerated error between the calculated points and the fit is 10^{-5} . Then the magnetic field between each z is interpolated linearly. The magnetic field can be known everywhere within the setup.

4.5.2 Depolarizations calculation

The depolarization rate due to magnetic field inhomogeneities was determined for two cases: the first one is by having fully polarized UCN with the “right” polarization within the apparatus. Then these UCN are analyzed when they strike the analyzing foil. The other configuration is by having UCN with the “wrong” polarization. These UCN bump onto the analyzing foil and are more easily depolarized. Figure 4.6 shows the results at the time $t = 40$ s.

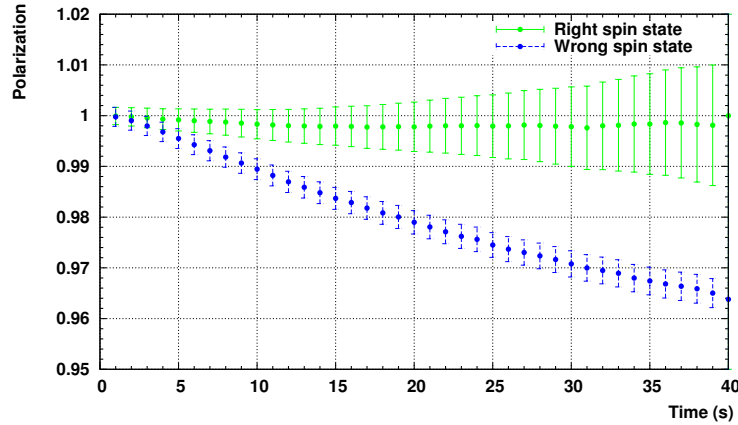


Figure 4.6: Depolarization of the wrong and right spin states UCN as a function of time.

After $t = 40$ s, a 4% depolarization due to magnetic field inhomogeneities is observed.

4.6 The longitudinal depolarization time T_1

As described in Chap. 1, the longitudinal depolarization time T_1 is an important parameter of the nEDM experiment. It governs the depolarization rate of the UCN with a spin component along the main magnetic field direction (Oz). T_1 characterizes two processes: depolarization from the wall collisions $T_{1,wall}$ and from magnetic field gradients $T_{1,grad}$:

$$T_1 = \left(\frac{1}{T_{1,wall}} + \frac{1}{T_{1,grad}} \right)^{-1} \quad (4.8)$$

Since the magnetic field in the chamber is very homogeneous (gradient lower than 1 nT/m), the second contribution is expected to be small. It will be estimated in Sec. 4.6.2 using perturbation theory [94].

4.6.1 Contribution on T_1 due to the wall collisions

Preliminary calculation

A preliminary calculation was done in order to estimate the relaxation time T_1 . We first consider the UCN as a polarized gas. Gravity is assumed to have no influence for this first result, but second order effects must be taken into account [95]. The Clausius result [96] is used to determine the UCN mean free path l within the chamber:

$$l = \frac{4V}{\sum_i S_i} \quad (4.9)$$

with V the volume of the chamber, and S_i the surface of the wall i .

UCN strike the walls of the chamber with a frequency:

$$f_i = \frac{\bar{v}}{l} \frac{S_i}{\sum_i S_i} = \frac{\bar{v}}{4V} S_i \quad (4.10)$$

\bar{v} is the mean velocity of the UCN.

The relaxation time T_1 is inversely proportional to the product of this frequency and depolarization probability per bounce β :

$$T_1 = \left(\sum_i f_i \beta_i \right)^{-1} \quad (4.11)$$

Finally, from Eq. (4.9), (4.10) and (4.11) we get:

$$T_1 = \frac{4V}{\bar{v} \sum_i S_i \beta_i} \quad (4.12)$$

For a mean UCN velocity of 3.15 m/s, a cell diameter of 470 mm and a cell height of 120 mm and depolarization probabilities as given in Table 4.3, we get: $T_1 = 30000 \pm 2000$ s. The error is estimated from the errors on the β coefficients found in the literature.

Monte Carlo simulation

A more realistic simulation was performed in order to determine T_1 . UCN are stored within the precession chamber, and the asymmetry is calculated for different storage times. The initial conditions are the same as defined in Sec. 4.4.2. The results are shown in Fig. 4.7.

From a fit of the simulated data we obtain: $T_1 = 23000 \pm 789$ s (the error is only statistical). Experimentally we found (Sec. 5.6.6) $T_1 = 2281 \pm 266$ s. This is a factor 10 smaller than the simulated value. This difference can be due to the cleanness of the surfaces. Indeed, a possible mechanism of the depolarizations due to wall collisions is by incoherent scattering of the UCN on impurities such as H atoms [97]. The β parameters come from dedicated measurements in which the cleanness of the surfaces was a critical point. It is not known in our case.

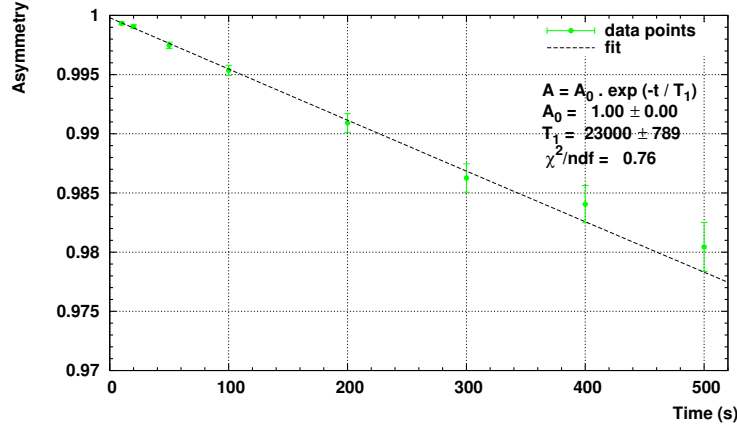


Figure 4.7: Evolution of the asymmetry for different storage times.

4.6.2 Dependence of T_1 with magnetic field gradients, Redfield Theory

The relaxation theory developed by Redfield [94] is used in this paragraph. The used formalism was previously used for Hg co-magnetometers by Pignol and Roccia [98], and is now used for UCN. The autocorrelation function R_b of the magnetic field is used to determine the depolarization rate. The autocorrelation function of an observable i is given by:

$$R_i(\tau) = \langle i(0)i(\tau) \rangle \quad (4.13)$$

with τ the correlation time and $\langle \rangle$ denotes a volume average.

Two magnetic fields are used: the main magnetic field B_0 , and a perturbative magnetic field b assumed to be small compared to the main field, and with a null mean value $\langle b \rangle = 0$. The depolarization comes from this perturbative field.

According to Slichter [99], the longitudinal and transversal depolarization times are functions of the autocorrelation function of the magnetic field b :

$$T_1 = \left(\gamma^2 \int_0^\infty d\tau \cos(\omega_L \tau) (R_{b_x}(\tau) + R_{b_y}(\tau)) \right)^{-1} \quad (4.14)$$

$$T_2 = \left(\frac{1}{2T_1} + \gamma^2 \int_0^\infty d\tau \cos(\omega_L \tau) R_{b_z}(\tau) \right)^{-1} \quad (4.15)$$

with γ the gyromagnetic ratio, ω_L the Larmor frequency and τ the correlation time. This approach is valid only if the perturbative field $b \ll B_0$, and if the correlation time is smaller than the observation time (convergence of the autocorrelation function).

At the first order, the magnetic field components are defined by:

$$\begin{pmatrix} b_x \\ b_y \\ b_z \end{pmatrix} = \begin{pmatrix} \alpha & \beta & \gamma \\ \delta & \epsilon & \zeta \\ \eta & \theta & \iota \end{pmatrix} \begin{pmatrix} x \\ y \\ z \end{pmatrix} \quad (4.16)$$

The static Maxwell equation $\nabla \times \vec{b} = 0$ imposes the gradient matrix to be symmetrical:

$$\begin{pmatrix} b_x \\ b_y \\ b_z \end{pmatrix} = \begin{pmatrix} \alpha & \beta & \gamma \\ \beta & \epsilon & \zeta \\ \gamma & \zeta & \iota \end{pmatrix} \begin{pmatrix} x \\ y \\ z \end{pmatrix} \quad (4.17)$$

We are now considering a uniform vertical gradient G , which means $\beta = \gamma = \zeta = 0$. Furthermore, Gauss's law for magnetism gives $\alpha + \epsilon + \iota = 0$. In our case, $\iota = G$ and, due to cylindrical shape of the chamber: $\alpha = \epsilon = -G/2$.

$$\begin{pmatrix} b_x \\ b_y \\ b_z \end{pmatrix} = G \begin{pmatrix} -\frac{1}{2} & 0 & 0 \\ 0 & -\frac{1}{2} & 0 \\ 0 & 0 & 1 \end{pmatrix} \begin{pmatrix} x \\ y \\ z \end{pmatrix} \quad (4.18)$$

This corresponds to a “trumpet-like” shape for the magnetic field, shown in Fig. 4.8. It is a typical model used in the literature [100]. Using this shape for the field, one can write the T_1

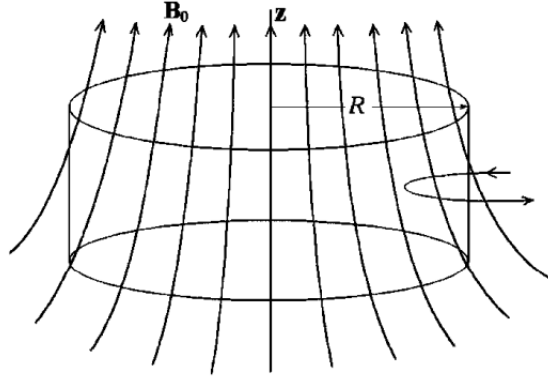


Figure 4.8: The “trumpet-like” magnetic field (vertical gradient). Picture taken from [100].

and T_2 times as a function of the position autocorrelation function. Then we have:

$$T_1 = \left(\frac{\gamma^2}{2} G^2 FT_x \right)^{-1} \quad (4.19)$$

$$T_2 = \left(\gamma^2 G^2 \left(FT_z + \frac{FT_x}{4} \right) \right)^{-1} \quad (4.20)$$

where FT_i is the Fourier transform of the position autocorrelation function (i is x , y or z):

$$FT_i = \int_0^\infty d\tau \cos(\omega_L \tau) R_i(\tau) \quad (4.21)$$

GEANT4-UCN was used to generate UCN trajectories within the precession chamber. Each hit point on the chamber's walls is stored, and trajectories between two successive hit point are

interpolated using a parabola. Since diffuse reflections change the trajectories, the autocorrelation functions have been calculated with different diffuse reflection probabilities. The results are shown in Fig. 4.9.

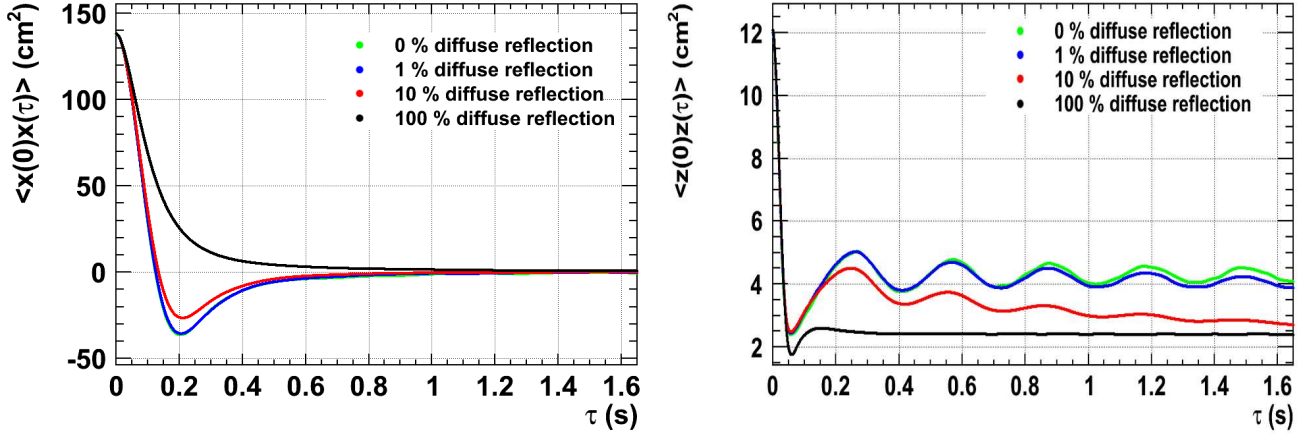


Figure 4.9: Left panel: Position autocorrelation function for the x and y components. Right panel: Position autocorrelation function for the z component. The curves correspond to different diffuse reflection probabilities as indicated.

The values of the autocorrelation function at $\tau = 0$ correspond to the mean values $\langle x^2 \rangle$ and $\langle z^2 \rangle$. These values are related to the geometry of the chamber. We have:

$$\begin{cases} \langle x^2 \rangle = \frac{1}{x_{max}} \int_0^{x_{max}} x^2 dx = \frac{2}{\pi D^2} \int_0^{D/2} r^2 2\pi r dr = \frac{D^2}{16} \\ \langle z^2 \rangle = \frac{1}{H} \int_{-H/2}^{H/2} z^2 dz = \frac{H^2}{12} \end{cases} \quad (4.22)$$

$$(4.23)$$

In our configuration, $D=47$ cm and $H=12$ cm, which leads to $\langle x^2 \rangle = 138.06$ cm² and $\langle z^2 \rangle = 12$ cm². One can also see that the autocorrelation function does not converge for the z component, due to gravity. The perturbative approach is not valid anymore in that case, which means the T_2 time cannot be estimated with this theory. Then the Fourier transform FT_x is calculated. The results are shown in Fig. 4.10.

Using Eq. (4.19), the value of the T_1 time has been calculated. The results are shown in Fig. 4.11.

The results show that the diffuse reflection probability does not change the dependence of T_1 with the vertical gradient G . For typical gradients in the precession chamber of about 1 nT/m, the $T_{1,grad}$ term is larger than 7×10^7 s.

4.7 Conclusion

The mechanisms through which UCN can be depolarized within the nEDM apparatus have been studied. The two main phenomena are depolarization due to wall collisions and depolarization

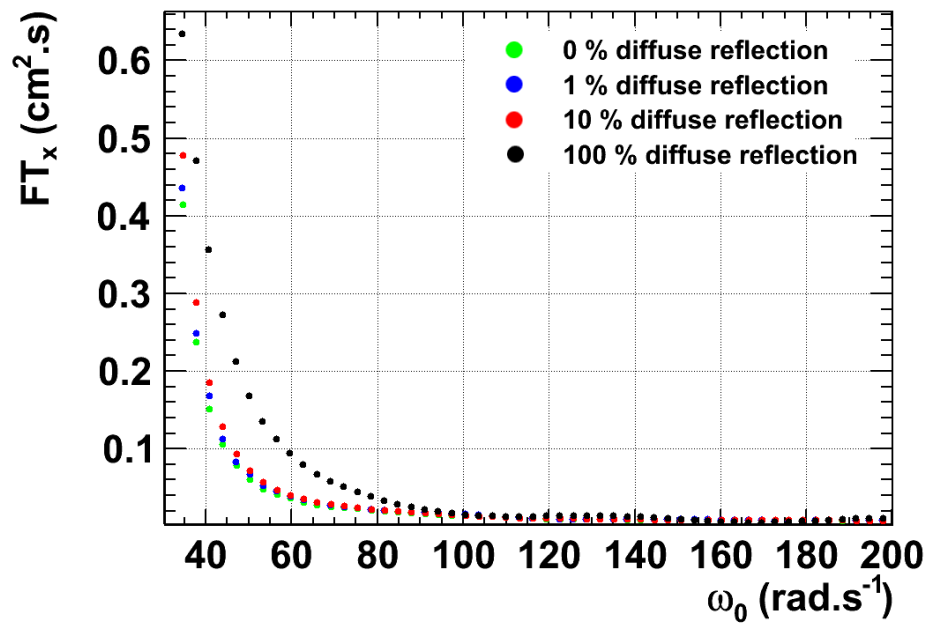


Figure 4.10: Fourier transform of the x position autocorrelation function. The points correspond to different diffuse reflection probabilities as indicated.

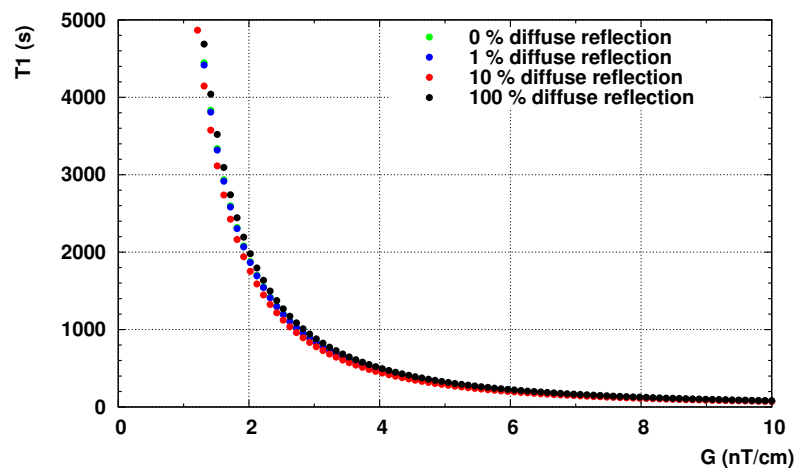


Figure 4.11: Dependence of the longitudinal depolarization time T_1 as a function of the vertical magnetic field gradient. The points correspond to different diffuse reflection probabilities as indicated.

due to magnetic field inhomogeneities. The first point was determined using the GEANT4-UCN Monte-Carlo code. Using a probabilistic model, it has been shown that the collisions are responsible for a loss in asymmetry of $0.8 \pm 0.1\%$. The same Monte-Carlo code was used to determine the efficiency of the superconducting polarizer. It has been found that the efficiency of polarization is higher than 97.5% but the result is strongly dependent on the initial velocity spectrum. Measurements of the UCN velocity distributions are required to confirm this result. The second depolarization process was simulated by the integration of the Bloch equation for neutrons within the nEDM apparatus from the precession chamber to the detector. The ambient magnetic field was calculated with MAENTOUCH (Chap. 3). The wrong spin state UCN are stored in the vertical guide and in the precession chamber during emptying. This results in a depolarization reduction of 4% for an emptying time of 40 s. The asymmetry at the end of a typical 180 s cycle (*i.e.* 40 s filling, 100 s storage, 40 s emptying) is:

$$\mathcal{A} = 94.4 \pm 1.6\%. \quad (4.24)$$

We have shown that the characteristic time T_1 can be determined using simulations. The main contribution in the reduction of T_1 arises from collisions with the walls. It was also possible to determine the contribution which comes from the magnetic field gradients by the estimation of the autocorrelation function of the x position of UCN. In spite of the fact that the T_1 contribution due to magnetic field gradients is negligible, the formalism used gave a new way to calculate relaxation times. The results of these simulations will be compared to experimental measurements described in the next chapter.

CHAPTER

5

Study of the UCN polarization analysis, performance of the apparatus

This chapter describes the polarizing-analyzing system of the nEDM experiment, first as it was at ILL during Phase I, and then as it is at PSI during Phase II. Both systems are compared. The second one was tested and characterized using the new UCN source at PSI.

5.1 Polarization principle

As explained in Chap. 1, the UCN are polarized using a transmission technique: a UCN is either transmitted or rejected during its travel in a high magnetic field region or the crossing of a magnetized material. In both cases, the interaction potential seen by the UCN is spin dependent:

$$V = V_F + V_m = V_F \mp \mu_n B \quad (5.1)$$

where V_F is the Fermi potential and V_m the magnetic potential, directly proportional to the magnetic field. Two systems can be used to perform this potential. The first one is the most common polarizing system used for ultracold neutrons. It consists of a thin layer of magnetized material (typically iron) coated on a substrate. The second one, less conventional, uses an external high magnetic field source. We firstly discuss the foils.

5.2 Polarizing or analyzing foils

The polarizing foils used up to now consist of some hundred nm thin iron layer deposited on an aluminium substrate. Aluminium is used because the substrate must be non magnetic, it should have a low Fermi potential and should absorb as less UCN as possible. Furthermore, it must be

robust enough to resist to the forces exerted during the pumping of the system. This fixes the thickness of the substrate, to a few tens of μm . A thin layer (some tens of nm) of aluminium is added on the iron layer in order to protect it. Then, the foil is placed in between permanent magnets which magnetize it up to saturation. The magnetic field close to the foil is around 90 mT in our system. The magnetization of several foils were measured as a function of the applied magnetic field. Foils with the iron deposited by an evaporation process in the presence of a magnetic field (“Caen foils”) and foils with the iron deposited by a sputtering process (“PSI foils”) were tested. The results are shown in Fig. 5.1. The “PSI foils” appear to be better because a smallest applied magnetic field is needed to reach a close to 100 % magnetization. This kind of foil will be used as UCN spin analyzer. The foil used in this chapter is a 1000 nm sputtered deposited iron layer on a 10 μm thick aluminium substrate. A 60 nm thick aluminium layer is added on the iron layer.

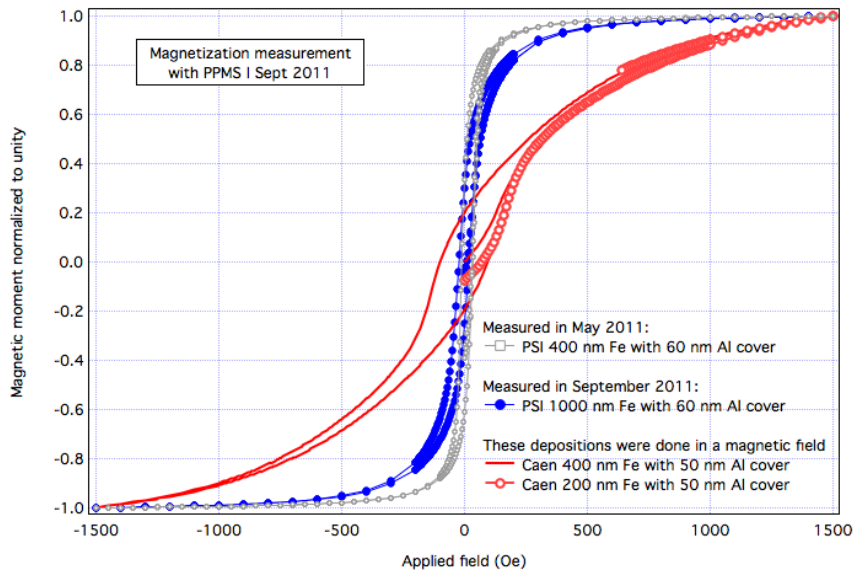


Figure 5.1: Foil magnetizations as a function of the applied magnetic field. Picture taken from [101].

With such a foil, the expected analyzing efficiency is around 88 to 92 % [4, 61] due to depolarizing processes which occur while the UCN interacts with the foil. Furthermore, UCN may be absorbed in the iron layer and in the aluminium substrate, this decreases the UCN density.

During the first phase at ILL, the polarization and analysis were done with thin foils only. This means UCN had to cross the foil at least twice to be detected: once during the filling of the precession chamber (polarizing), and once during the emptying of the chamber (analyzing). This leads to losses and depolarizations twice as large compared to a single passage. A maximum polarization of 85 % was reached [61].

5.3 The new UCN polarizer

A new polarizing system was designed to avoid depolarizations and losses which occur when UCN are going through the polarizing foil. An alternative is to replace the magnetic material

by a high magnetic field. Nevertheless, the magnetic field must be larger than the one within a foil system to compensate for the absence of Fermi potential. Assuming a 2 T inner magnetic field (*i.e.* a 120 neV potential) and a Fermi potential of 210 neV for the polarizing foil, results in a 330 neV potential, which corresponds to a 5.47 T magnetic field. Such a high magnetic field can be created by a superconducting coil.

5.3.1 Description of the magnet

The polarizer used is a horizontal-bore superconducting coil. A maximum magnetic field of 5 T was chosen (instead of the 5.47 T) because no UCN with an energy higher than 300 neV (which corresponds to a 5 T magnetic field) are expected [89]. Indeed, the Fermi potential of the UCN guides (which is around 230 neV) cleans the UCN spectrum from the UCN source to the polarizer (13 m in between). The magnet is shown in Fig. 5.2.



Figure 5.2: Picture of the superconducting polarizer.

The polarizer was built before this thesis by American Magnetics Inc. The requirements of the new polarizer were:

- an horizontal magnetic field of 5 T at the magnet center
- a cylindrical geometry of the magnetic field (with respect to the geometry of the UCN guides)
- a radial component of the magnetic field as small as possible
- a low stray field to avoid disturbing the magnetic field within the precession chamber

The two first requirements are fulfilled by the geometry of the superconducting coil, which is a solenoid. The two last requirements are fulfilled due to an active shield: other solenoids with larger radii and reversed polarity are added to decrease the radial component of the field. A calculated magnetic field map is given in Fig. 5.3. The adiabaticity parameter (Chap. 3) was

calculated within this magnetic field. A minimal value of 20000 was found (were the radial component of the field increases, close to the active shielding coils at $z=20$ cm and $r=9$ cm), which fulfills the adiabaticity conditions.

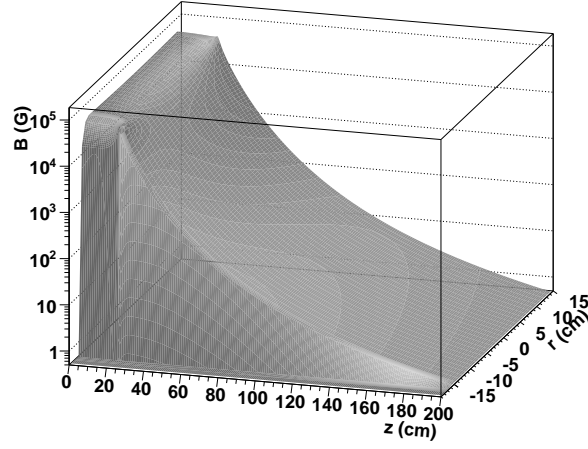


Figure 5.3: Theoretical magnetic field profile created by the SC magnet polarizer. $z=0$ and $r=0$ denote the center of the magnet.

These values are acceptable and sufficient if the magnetic field created by the magnet is the same as the calculated values. A magnetic field characterization was done to check this assumption.

5.3.2 Characterization

The superconducting solenoid was mapped to estimate the reliability of the calculated field maps given by the constructor. The mapping was done at three different main positions. Different instruments (with different ranges) were used for each position:

- central magnetic field using a Hall probe
- stray field using a magnetic transducer
- far stray field using a fluxgate

The magnet was not installed on the beamline during these measurements.

The aim of the first measurement was to check the maximum magnetic field at the center of the SC magnet. We used a Lakeshore Hall probe model 410 [102] for this purpose. Unfortunately, this sensor cannot measure a magnetic field larger than 2 T. The probe was placed at the center of the magnet, and the current was ramped. The magnetic field was measured for several values of the current. For a solenoid without any ferromagnetic material, there is a linear relation between the applied current and the created magnetic field. For this magnet, the constructor gave a “coil constant” of $0.413 \text{ kG} \cdot \text{A}^{-1}$. Measurements were done for 8 different currents, and the results are shown in Fig. 5.4. The error on the measurement is the combination of the error which comes from the probe itself (0.1 %) and from the error on the probe position. Since

the probe did not move during the full measurement, the error is rather small (less than a millimeter). Then the maximal value of the magnet was extrapolated from this plot. We have:

$$B_{zmax} = 50.00 \pm 0.06 \text{ kG} \quad (5.2)$$

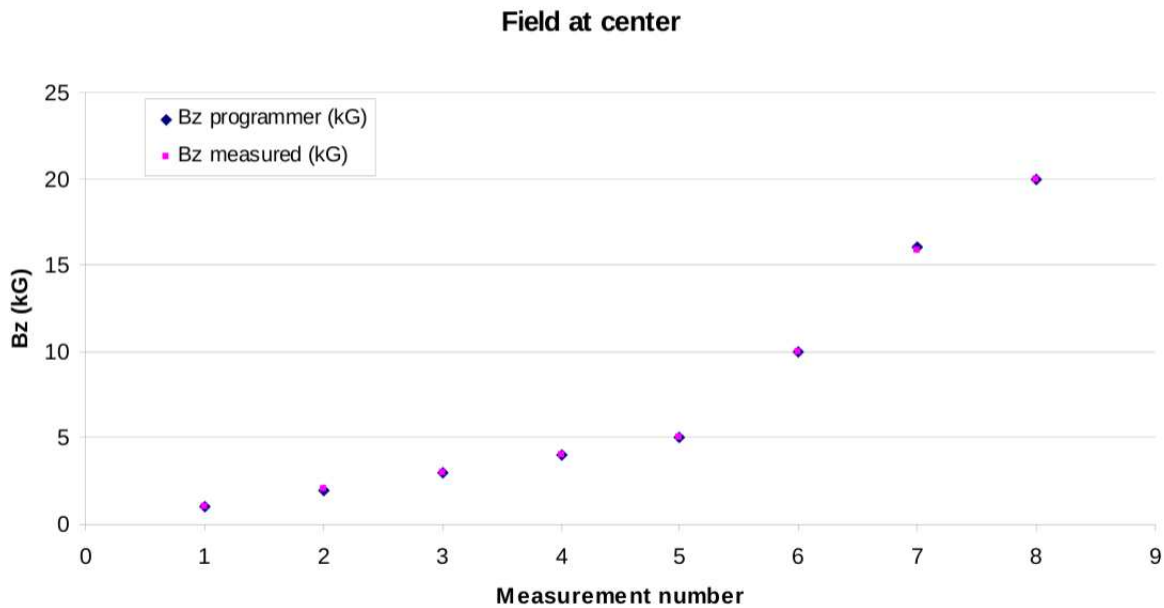


Figure 5.4: Magnetic field at the center of the SC magnet. Measured and calculated magnetic fields are given. Error bars for the measured points are smaller than the points.

The aim of the second series of measurements was to check the magnetic field created by the SC magnet along the horizontal guide. A 2D magnetic transducer from Senis [103] was used for this purpose. This device was calibrated just before the measurement. In these conditions, the error from the device is around 0.01 %. The main source of error comes from the transducer position. A 2D mapper was used. The x and y components were controlled with an accuracy of around 1 mm, but not the z component (roughly 1 cm, depending on the distance). The error related to the position was estimated by doing reproducibility measurements. The results for the measurements on axis are given in Fig. 5.5. Calculated and measured values are compatible within the errors.

Finally, the far stray field of the SC magnet was measured to determine its influence on the magnetic shield and the precession chamber. A Bartington fluxgate (the same as used in Chap. 3) was used for this purpose. The error on the measurement mainly arises from the error on position and angle of the fluxgate. Reproducibility measurements were done to estimate this error. A mean ambient field (measured with the magnet off) was subtracted as a background field. Three measurement points were chosen:

- two positions where the first layer of shielding is located.
- the center of the precession chamber.

The results are summarized in Table 5.1. The radial component of the measured magnetic field is in agreement with the theoretical one, but not the axial component. However, the measurements

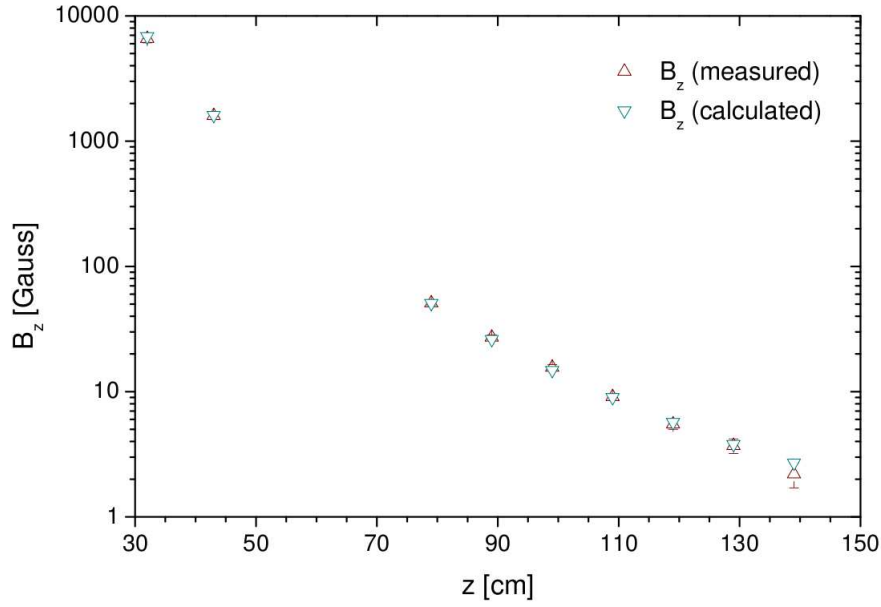


Figure 5.5: Measured and calculated axial magnetic field on axis. $z = 0$ denotes the center of the magnet.

were done in a rather bad magnetic environment, which can explain the difference. Despite these results, the magnetic field is small enough to be compensated for by the SFC system.

Table 5.1: Far stray field created by the SC magnet measured with a fluxgate.

Z (cm)	r (cm)	B_{ztheo} (μ T)	B_{zmeas} (μ T)	B_{rtheo} (μ T)	B_{rmeas} (μ T)
180	100	14.34	22 ± 1	28.12	29 ± 1.5
180	122	6.47	9.9 ± 0.8	21.46	21 ± 1
312	124	4.65	5.6 ± 0.4	3.85	3.5 ± 0.4

As a conclusion, the magnetic field created by the new polarizer is in agreement with the requirements. The SC magnet can be used with ultracold neutrons.

5.4 Spin reversal : the adiabatic spin flipper

This section describes the adiabatic spin flippers used in our setup. A new one was designed and simulated to fit with the new polarizer. It was then tested at ILL.

5.4.1 Principle

The adiabatic spin flipper is used to reverse the UCN spin. It is based on an adiabatic passage of neutrons through a magnetic resonance. Two elements are needed for this passage:

- an inhomogeneous static magnetic field (B_0) with a gradient along a defined direction.

- a radio frequency magnetic field (B_1) perpendicular to the static gradient.

The B_1 magnetic field is rotating with a frequency ω . Initially, the UCN spin is assumed parallel to the static field. A new frame F_1 is chosen: it moves with the neutron and turns around the B_0 field direction with a frequency ω . So in the frame F_1 , the effective magnetic field experienced by the neutron is:

$$\vec{B}_{eff} = (B_0 - \omega/\gamma)\vec{b}_0 + B_1\vec{b}_1 \quad (5.3)$$

with γ the gyromagnetic ratio of the neutron, \vec{b}_0 the unitary vector along B_0 and \vec{b}_1 the unitary vector along B_1 . At the resonance point, the Larmor frequency is equal to the frequency of the rotating B_1 field. Then we have:

$$B_0 = \omega/\gamma \quad (5.4)$$

This means that the effective magnetic field experienced by the UCN is only along \vec{b}_1 :

$$\vec{B}_{eff} = B_1\vec{b}_1 \quad (5.5)$$

At this point, the neutron spin precesses perpendicularly to the static field. Then the UCN leaves the resonance point, and its spin is antiparallel to the static field B_0 at the end of the process. The spin follows \vec{B}_{eff} adiabatically. The evolution of the spin is shown in Fig. 5.6.

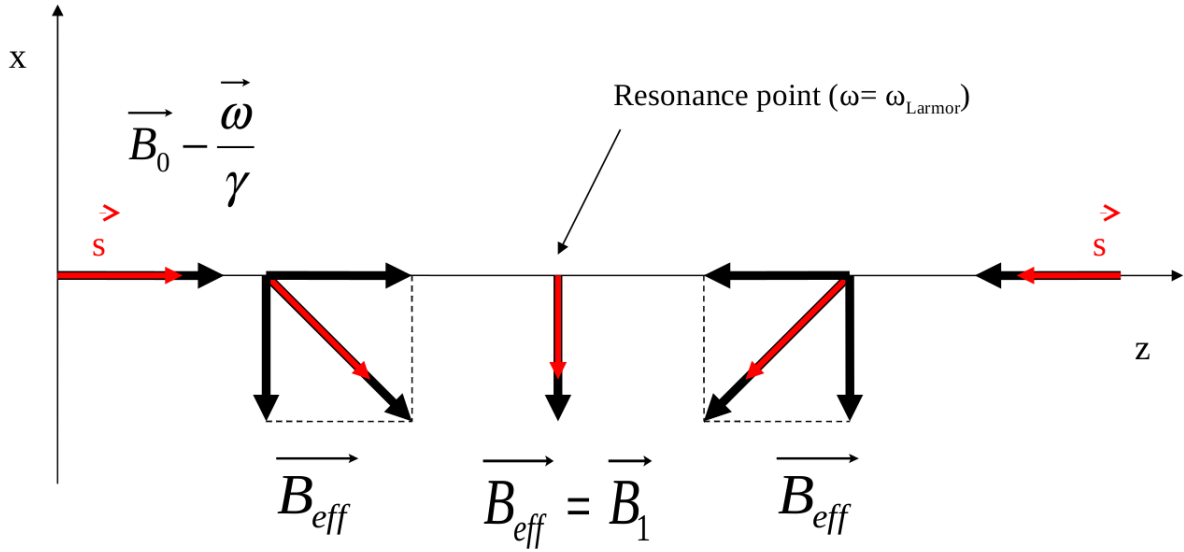


Figure 5.6: Evolution of the spin during the spin flip process. In this scheme, the B_0 field is along the z axis, and the B_1 field along the x axis.

In the reference frame F_1 , the equation of motion for the spin \vec{S} is:

$$\frac{d\vec{S}}{dt} = \gamma\vec{S} \times \vec{B}_{eff} \quad (5.6)$$

A second frame F_2 is defined such that the z axis stays along \vec{B}_{eff} and rotates in F_1 with an angular velocity $\vec{\Omega}$. In this frame, Eq. (5.6) becomes:

$$\frac{d\vec{S}}{dt} = \vec{S} \times (\gamma\vec{B}_{eff} + \vec{\Omega}) \quad (5.7)$$

This equation is similar to Eq. (3.3). In the same way, an adiabaticity parameter can be defined as the ratio of the Larmor frequency γB_{eff} and the magnitude of the angular velocity Ω . If this parameter is larger than one, the adiabaticity condition is fulfilled, and a spin flip efficiency close to 100 % can be reached [104]. The parameter k can be written as a function of the static and RF magnetic fields:

$$k = \frac{\gamma B_1^2}{v |dB_0/dz|} \quad (5.8)$$

with v the velocity of the UCN and $|dB_0/dz|$ the static gradient.

5.4.2 Adaptions for the new experiment

We have seen that the radio frequency magnetic field of the spin flipper must be perpendicular to the static field.

In the classical adiabatic spin flipper arrangement used up to now with UCN [48], the direction of the static field was perpendicular to the beam axis, while the RF field was parallel. Since the SC magnet polarizer, which will be used at the PSI UCN beamline, defines the quantization axis parallel to the beam and because of very strict space constraints for the nEDM apparatus, it will be more convenient to follow the technique with the directions of the static and RF fields exchanged. This has previously been used as reported in Ref. [105]. The radio frequency field will be created by a rectangular coil pair which ensures a homogeneous radial magnetic field at its center. A calculation of the magnetic field which can be created by such a rectangular coil pair was done using the RADIA [75] computation code (Sec. 3.4.1).

The coils were placed in Helmholtz configuration. Figure 5.7 shows the field profile of such a coil pair exhibiting a magnetic field of 140 μT at the center. Here 15 turns per coil and a current of 2 A were used).

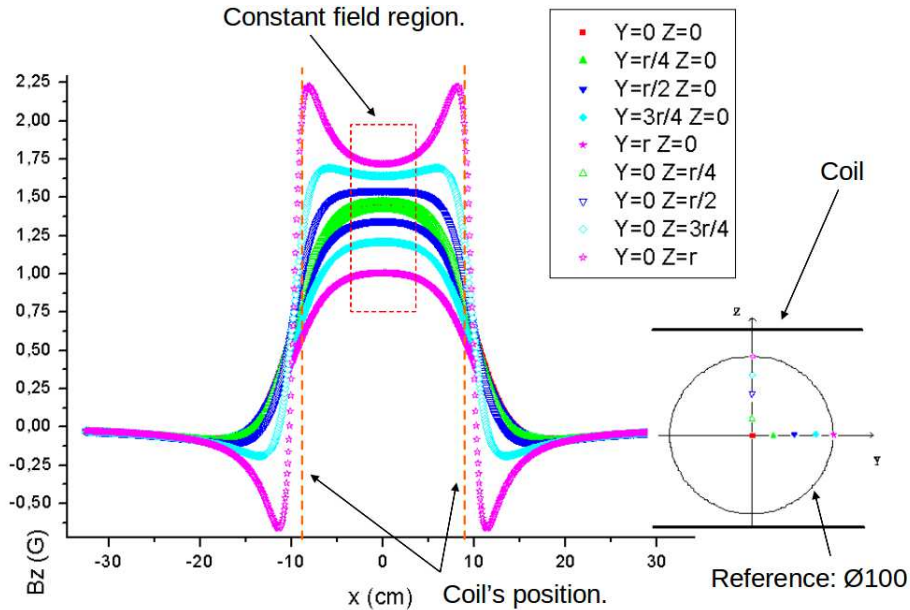


Figure 5.7: Field created by the RF coil. $X=Y=Z=0$ is the center of the coil. r is an arbitrary distance of 50 mm.

The homogeneity is defined as:

$$H = \left| \frac{B_{z,max} - B_{z,min}}{B_{z,max}} \right| \text{ with } z = \text{constant} \quad (5.9)$$

Since the inner diameter of the UCN guide is 73 mm, the homogeneity at the center ($z = 0$) of the coil is less than 15 %.

Finally, the dimensions chosen are shown in Fig. 5.8. These dimensions (195×130 mm) are compatible with the requirements so that the flipper can be installed on the nEDM apparatus.

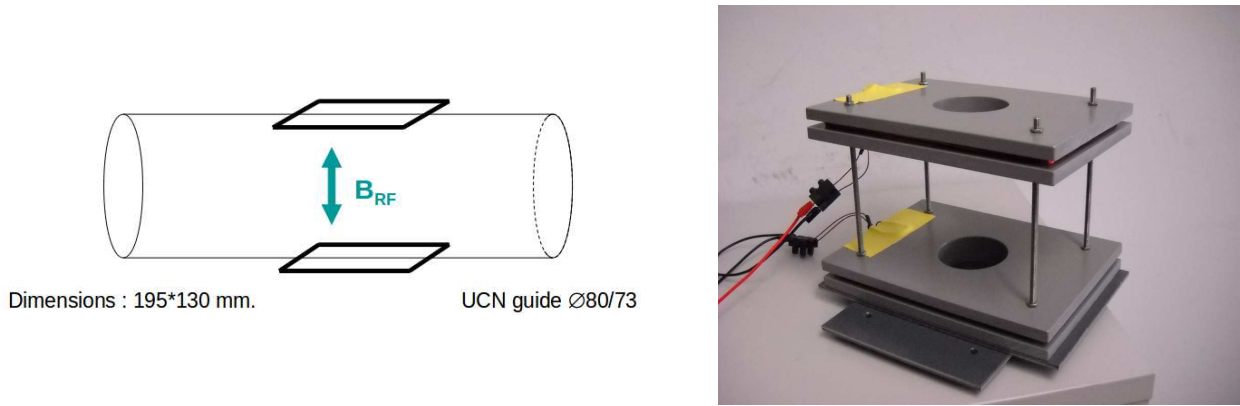


Figure 5.8: Left panel: Scheme of the RF coil. Right panel: Flipper Coil.

Since the SC magnet was not ready to be used when the spin flipper was designed, a set of coils was simulated with RADIA to try to reproduce the stray field of the polarizer. Due to geometry constraints, the chosen resonance point will be between 700 and 1500 μT . This corresponds to a flipper position just outside of the Thermohouse (Chap. 2). The set of coils have to reproduce the magnetic field between these two values. Since the polarizer generates a cylindrical magnetic field, the set of coils will be solenoids. Their radius must be large enough to allow the passage of the RF coils inside. A set of three coils was chosen. A comparison between the magnetic field created by this set and the one created by the SC magnet is shown in Fig. 5.9. The differences are smaller than 5 %. The geometry of the new static field coils is shown in Fig. 5.10.

5.4.3 Experimental setup

The new spin flipper was tested at ILL to determine its efficiency. The aim of the measurement was to:

- carry out tests in which the static field of the ASF was designed to reproduce conditions at the nEDM experiment (stray field of the SC magnet).
- scan the static and RF magnetic field parameter space of the adiabatic spin flipper to work with UCN, and measure the flipping efficiency very accurately with the best configuration.

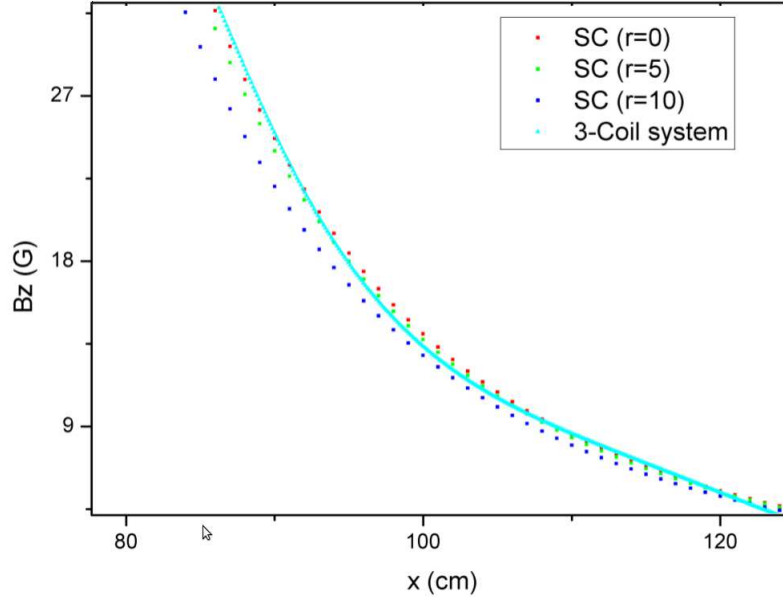


Figure 5.9: Axial magnetic field created by the SCM compared to the one created by the gradient coils. r is in cm. $x=0$ is the center of the SC magnet.

An efficiency measurement requires the same experimental set up as for the determination of the polarization of a UCN beam, except that two flippers are needed. Indeed, the efficiency is a function of four measurements, depending whether the flippers were on or off. We have [106]:

$$\left\{ \begin{array}{l} f1 = \frac{N_{11} - N_{10}}{N_{00} - N_{01}} \end{array} \right. \quad (5.10)$$

$$\left\{ \begin{array}{l} f2 = \frac{N_{11} - N_{01}}{N_{00} - N_{10}} \end{array} \right. \quad (5.11)$$

with N_{00} the number of UCN counted with both flippers off, N_{10} the number of UCN counted with flipper 1 on, N_{01} the number of UCN counted with flipper 2 on, and N_{11} the number of UCN counted with both flippers on. f is a number between 1 and -1 . For a value of 1, the spin of the full beam is flipped. A value of -1 means no effect of the spin flipper, and a value 0 means a complete depolarization of the beam. Equations (5.10) and (5.11) assume that the number of counts N_{ij} has been normalized to the measuring time and incoming beam intensity. A UCN ^3He counter located upstream was used to measure the incoming UCN flux. The experimental setup is sketched in Fig. 5.11 and Fig. 5.12 shows a picture of the experiment. In order to determine the efficiencies of the spin flippers, two identical SF were used [107]. Permanent magnets magnetize close to the saturation the polarizer and analyzer foils (iron on aluminium). The quantization direction was perpendicular to the beam axis. The UCN guide section between the polarizer and analyzer foils is a quartz tube.

The data acquisition system gives us the dead time and the counting rate, which is used to correct the number of UCN for the dead time. Measurements are normalized by the monitor. The error on each measurement quoted here below is statistical.

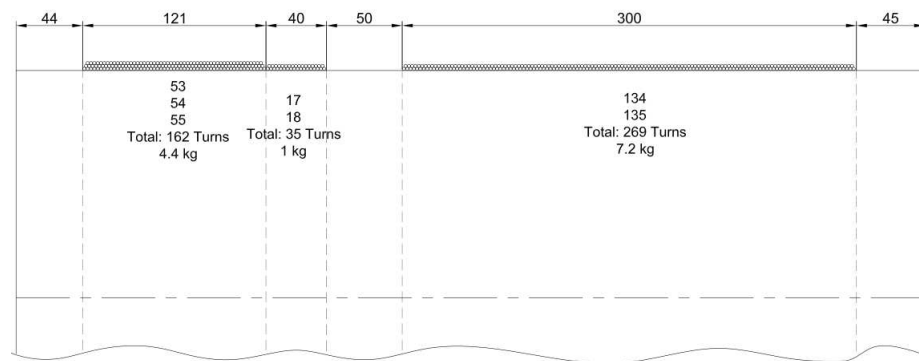


Figure 5.10: The static gradient coils scheme (cut). Their length allow us to use the resonance point for the spin flipper between 700 and 1500 μT as expected. The radius is 150 mm, and the current used in each coil is (from left to right): 5.33 A, 2.22 A, 0.6 A

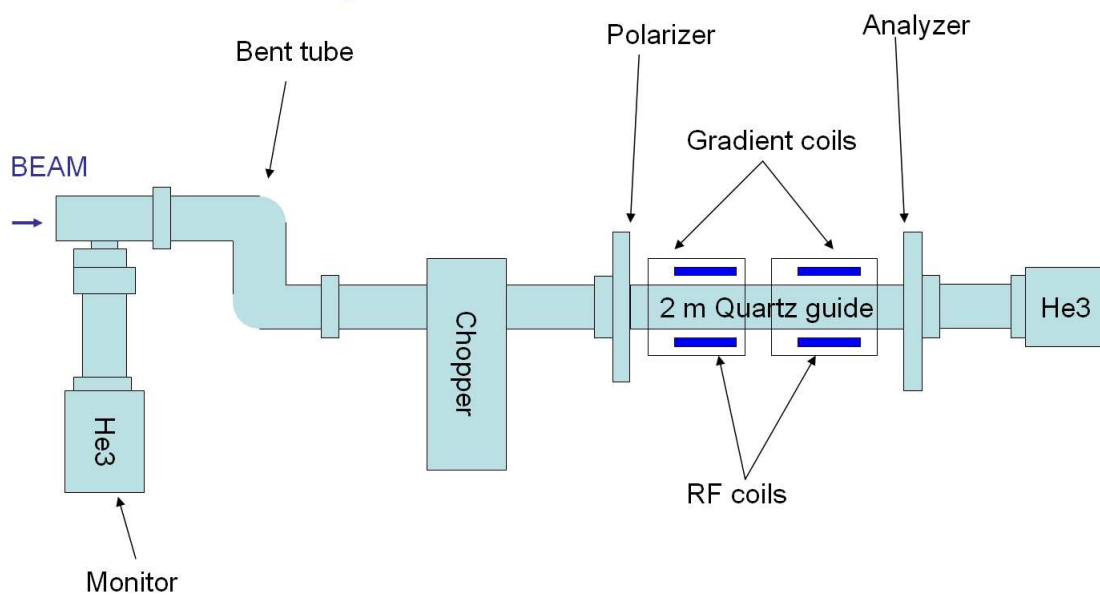


Figure 5.11: Scheme of the experiment. The chopper was not used in this measurement.

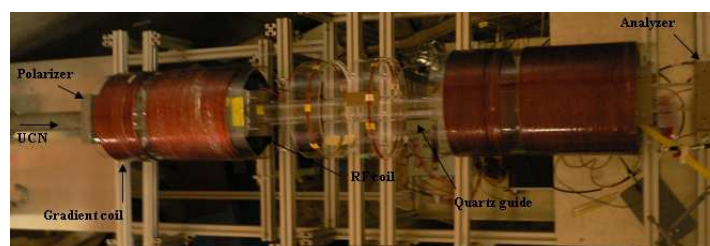


Figure 5.12: Photo of the experiment. The corrections coils (thin solenoids between the two gradient coils) are not used since the Earth field is large enough to keep the polarization between the two gradient coils.

5.4.4 Analysis

Scanning parameters

A set of four measurements of N_{ij} were done for four different resonance points (from 1500 to 750 μT). It was possible to reach 100 % efficiency within the errors for each resonance point. At 750 μT (*i.e.* a resonance frequency of about 22.5 kHz), a scan of frequencies was done. Due to the length of the flipper, several frequencies can be used. The results are shown in Table 5.2.

Table 5.2: Scanning in frequency for the RF coil. The resonance frequency is 22.5 kHz. At 20 and 25 kHz the efficiency is also 100 %.

Frequency (kHz)	Efficiency reached
10	0.063 ± 0.003
15	0.983 ± 0.003
20	0.998 ± 0.003
22.5	1.000 ± 0.003
25	1.001 ± 0.003
30	0.992 ± 0.003

The amplitude of the RF field was scanned at a fixed resonance frequency of 22.5 kHz. Assuming a maximum UCN velocity of 10 m.s^{-1} , it was possible to calculate the adiabaticity parameter for each value of the RF field. Luschikov and Taran [104] have calculated the efficiency of spin flippers as a function of the adiabaticity parameter in the ideal case of a linear static field gradient. A comparison with experimental data was done. The results are shown in Fig. 5.13. Theory and experiment are in agreement.

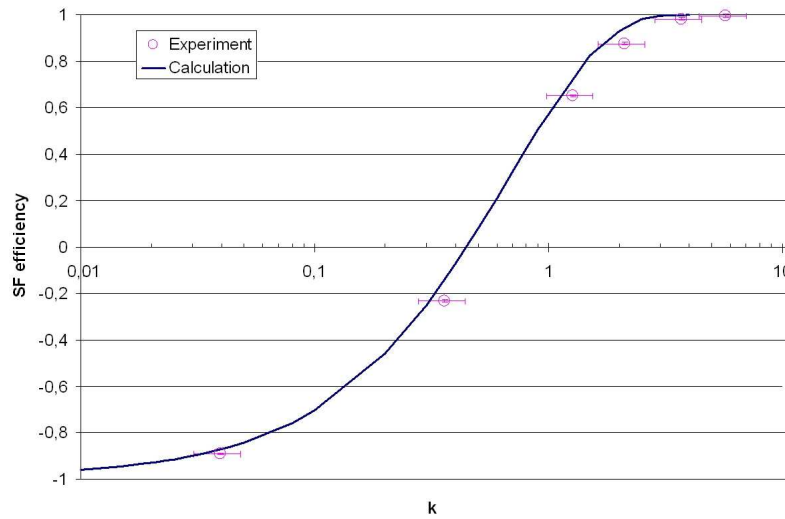


Figure 5.13: Comparison between theoretical dependence of the spin flipper efficiency with the adiabaticity parameter (line) and experimental results (dots).

Optimization of f

Once a good configuration was found, statistics was accumulated to reduce the error on the efficiency. The chosen parameters for this purpose were the following:

- resonance magnetic field: $750 \mu\text{T}$
- static field gradient: $30 \mu\text{T.cm}^{-1}$
- RF frequency: 22.5 kHz
- RF field: $1200 \mu\text{T}$

This leads to an adiabaticity parameter of 32, enough to reach a 100% efficiency. 25 sets of four measurements were done. For each set, the spin flipper efficiency was calculated. The results are depicted in Fig. 5.14. The final spin flipper efficiency is extracted from a linear fit:

$$f = 1.0003 \pm 0.0008 \quad (5.12)$$

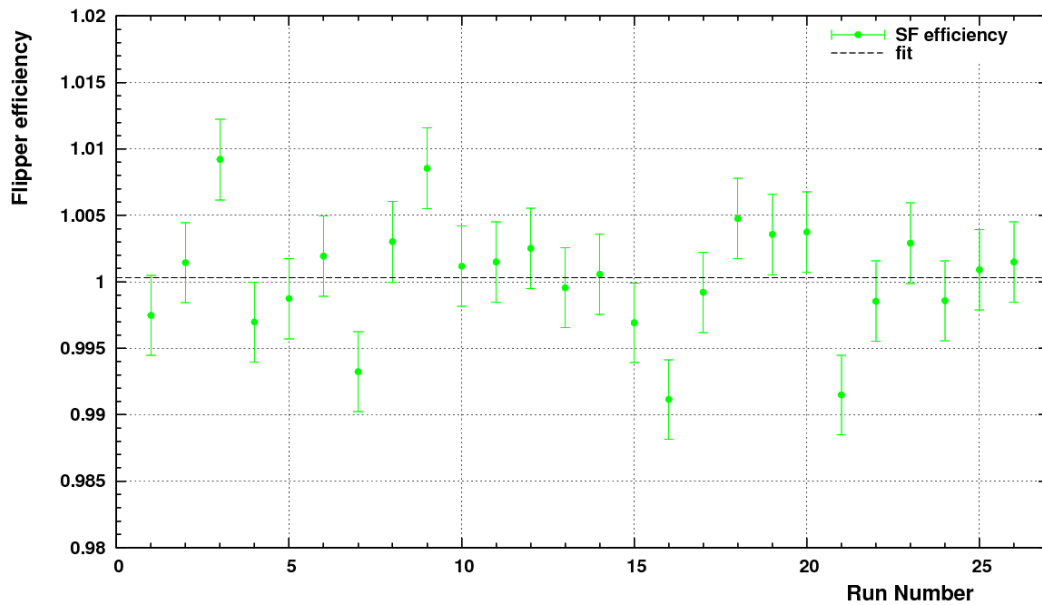


Figure 5.14: Spin flipper efficiency for 25 identical measurements.

Determination of the spin flipper efficiency at PSI.

The same setup as described in Sec. 5.5.1 was used to determine the efficiency of the two spin flippers at PSI. The first one (named SF1 in Fig. 5.15) is the one tested at ILL. The second flipper (SF2) is a solenoid like coil placed above the polarizing foil, and it uses the stray field of the analyzing magnets as the static field. Spin flippers similar to this one were already tested [90], and give an efficiency close to 100 %. The results of the measurement along with the spin flippers parameters are summarized in Table 5.3.

Table 5.3: Characteristics of the two spin flippers used and their measured efficiencies

Spin-flipper	SF1	SF2
Type	Rectangular coil pair	Solenoid
Power	External wave generator	DAQ board
Amplifier	Home made	Home made
Resonance point (G)	8.5	8
Static gradient (G/cm)	0.3	1.5
RF frequency (kHz)	25.5	25
RF amplitude (G)	0.65	2
Adiabaticity condition	Fulfilled	Fulfilled
Efficiency (%)	100.4±0.3	99.3±0.3

5.5 Efficiency of the polarization analysis

The polarization of a UCN beam can be classically described by a 3 dimensional vector:

$$\vec{P} \equiv (P_x, P_y, P_z) \quad (5.13)$$

In the nEDM experiment, the magnetic field of the polarizer and the analyzer are along the $-x$ direction. In this chapter, P denotes the polarizing efficiency, and A the analyzing efficiency. These efficiencies are related to the chosen quantization axis: $P = P_{-x}$.

The polarization of the UCN beam is defined as the asymmetry between the number of counted spin up neutrons and spin down neutrons:

$$A \times P = \frac{N_{up} - N_{down}}{N_{up} + N_{down}} \quad (5.14)$$

The polarizer allows only one spin state to pass through, so that the spin has to be flipped to allow the detection of the other spin state. This is done with an adiabatic spin flipper [48]. The process is explained in the next section of this chapter. Equation 5.14 assumes a 100 % efficient spin flipper. For a real spin flipper with an efficiency f , the polarization is:

$$A \times P = \frac{N_0 - N_1}{f \times N_0 + N_1} \quad (5.15)$$

where N_0 denotes the number of UCN counted with spin flipper off, and N_1 the number of UCN counted with spin flipper on.

5.5.1 Experimental setup, measurements

The determination of the polarizing-analyzing efficiency was done using the nEDM apparatus at PSI. The UCN switch (Sec. 2.2.2) was placed in the “monitoring” position. In this way, UCN are going from the source directly to the detector (they are not stored in the precession chamber). UCN pass first through the SCM magnetic field. They travel then inside the horizontal UCN guide where their spin is maintained with the guiding field coils (with their nominal currents,

see Table 5.4). Then they pass within the switch, and the spin state is analyzed (using the foil described above) and the UCN are detected with the NANOSC detector. A scheme of the experimental setup is shown in Fig. 5.15.

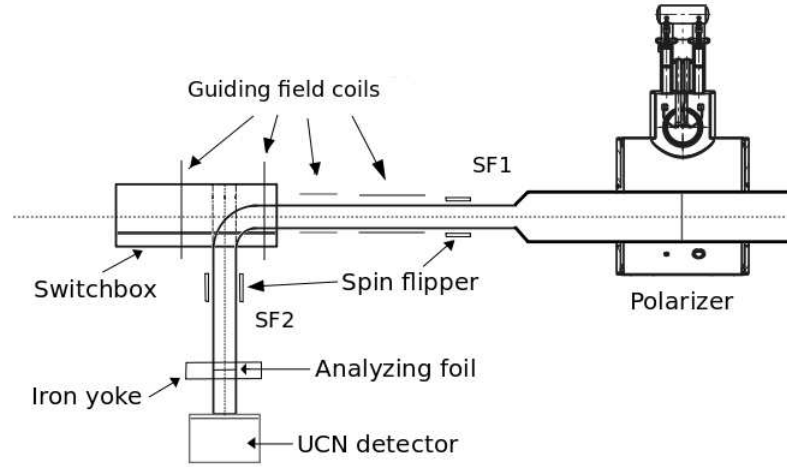


Figure 5.15: Experimental setup for the polarizing-analyzing efficiency determination. Only the SF1 spin flipper is used for this part.

Following Eq. (5.15) two measurements are needed to determine the degree of polarization of the beam. The acquisition system allows us to know the time when UCN are detected. In this way, a time of flight spectrum can be generated, and cuts in time can be applied. Typical TOF spectra with and without the spin flipper are shown in Fig. 5.16.

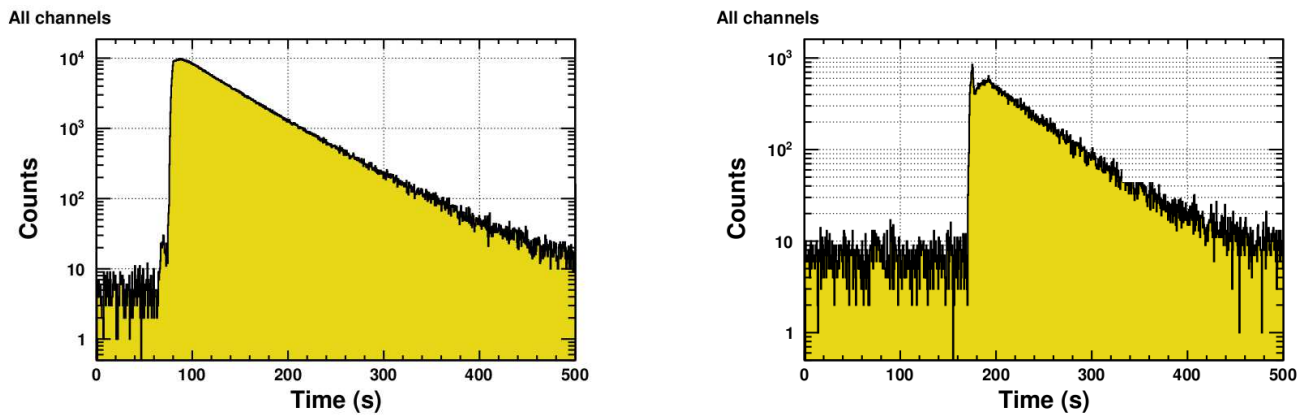


Figure 5.16: Left panel: Time of flight spectrum without spin flipper. Right panel: Time of flight spectrum with spin flipper. The intensity of the beam is divided by a factor of about 15.

The NANOSC detector is sensitive to γ rays. A cut in the charge spectrum was performed to remove this contribution. The cut is done at channel 5000. With this cut, only 0.05 % of the counted events come from γ [108] as shown in Fig. 5.17.

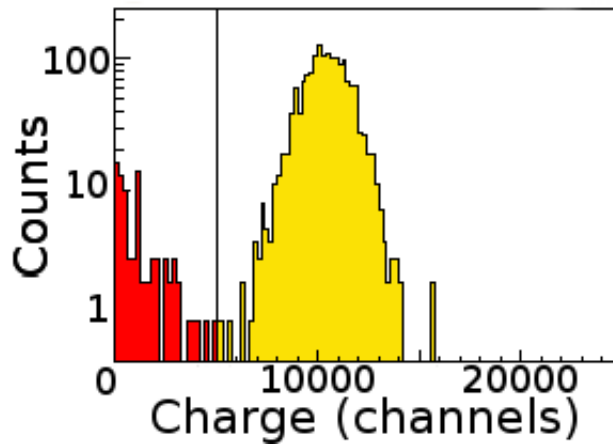


Figure 5.17: UCN charge spectrum. The cut at channel 5000 is shown. The UCN contribution is denoted in yellow, and the γ -noise contribution is denoted in red.

Table 5.4: Guiding field coils and their applied currents

Channel	name	coil	current (mA)
1	UCK	UCn Kamin (chimney) coil	-20
2	HGSW	Horizontal Guide SWitch side solenoid	-100
3	HGSC	Horizontal Guide SC magnet side solenoid	-60
4	CSWC	Central SWitch Coil	-60
5	VGSA	Vertical Guide Saddle coil	40
6	VGSO	Vertical Guide SOlenoid	2
7	-	spare (not used)	0
8	SR (1 & 2)	Switch Rectangular coils	-60

5.5.2 Extraction of the polarization

Once the two measurements are done, the product $A \times P$ can be calculated. Measurements were done three times to check the reproducibility. The measurements were not monitored, this choice is explained in Appendix A.1. The error on the product $A \times P$ is calculated from the statistical errors on N_0 and N_1 , and also the error on f (detailed in the next section). We have deduced:

$$A \times P = 88.5 \pm 0.3\% \quad (5.16)$$

A value of about 100 % was expected for P , and 92 % for A . Similar measurements were done again, but where the current within the SC magnet was decreased. Four different magnetic fields were tested. The results are shown in Table 5.5.

We can see that within the errors the asymmetry is the same for 5 and 4.5 T, what would indicate that the efficiency of the SC magnet is close to 100 %. Nevertheless, only a precise characterization of the analyzing foil will confirm this hypothesis.

Table 5.5: Value of the asymmetry as a function of the polarizer magnetic field.

B (T)	PA (%)
5	88.5 ± 0.3
4.5	88.2 ± 0.3
4	87.7 ± 0.3
3.5	86.1 ± 0.3

5.6 UCN within the precession chamber

Once the polarizing, analyzing and spin flipper efficiencies were determined, the characterization of the full apparatus can be done. UCN are now going within the precession chamber. Several parameters that are useful for the optimization of an nEDM measurement will be determined and optimized. The default configuration of the B_0 coil is “up” in this section.

5.6.1 Experimental setup

The measurements described here use the same experimental setup, namely the nEDM apparatus. Each cycle can be divided in different sequences:

- the proton beam strikes the spallation target. A fraction of the created neutrons are downscattered to UCN using the solid deuterium moderator.
- UCN enter the apparatus and the precession chamber is filled during a time τ_{fill} .
- the chamber shutter is closed and UCN are stored within the precession chamber during a time T_0 . During this time, the UCN switch rotates from the “filling” position to the “emptying” position. It also passes through the “monitoring” position, and stay in this position during 8 seconds. UCN from the horizontal guide are counted, this allows us to monitor the UCN flux from a run to another.
- the shutter is opened and UCN are counted during a time τ_{count}

The time at which each UCN is detected is stored. The described sequence can be visualized in a time spectrum. An example is given in Fig. 5.18.

5.6.2 Filling of the apparatus with UCN

The first parameter which has to be optimized when UCN are filling the chamber is the filling time. Without any depolarizing process, the maximum number of stored spin up UCN (N_{max}) can be reached asymptotically because absorption and losses processes limit the density within the chamber. The number of stored UCN as a function of time can be written as:

$$N_{uparrow}(t) = N_{max}(1 - e^{-t/\tau_{fillnodepol}}) \quad (5.17)$$

Depolarization processes can however occur during the storage. The decrease is exponential:

$$N_{uparrow}(t) = N_{max}e^{-t/\tau_{depol}} \quad (5.18)$$

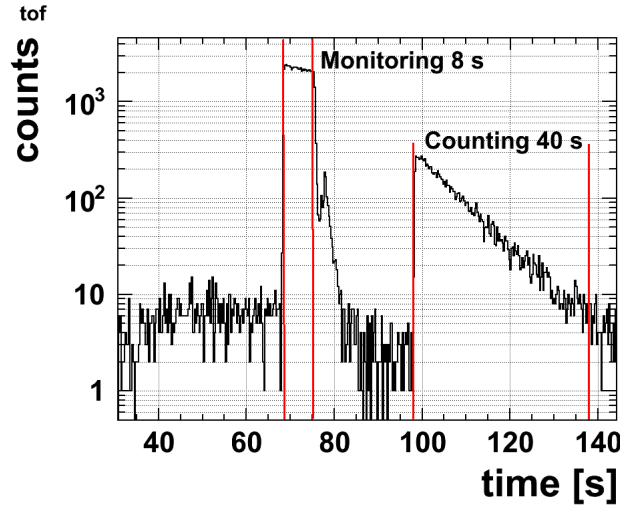


Figure 5.18: Example of a time sequence. The monitoring and counting periods are indicated.

Finally, the number of UCN as a function of time within the precession chamber is the combination of two effects:

$$N_{uparrow}(t) = N_{max}(1 - e^{-(t-t_0)/\tau_{fillnodepol}})e^{-(t-t_0)/\tau_{depol}} \quad (5.19)$$

where t_0 is an offset in time. Several cycles were done with different filling times. Since the number of UCN counted during the “monitoring” is a function of the filling time, data were not normalized. But each run was measured twice to check reproducibility. The storage time was 15 s and the counting time was 40 s. The errors are only statistical. The results are shown in Fig. 5.19. The best filling time is the one where the number of counted UCN is maximal. We find: $\tau_{fill} = 31 \pm 1$ s.

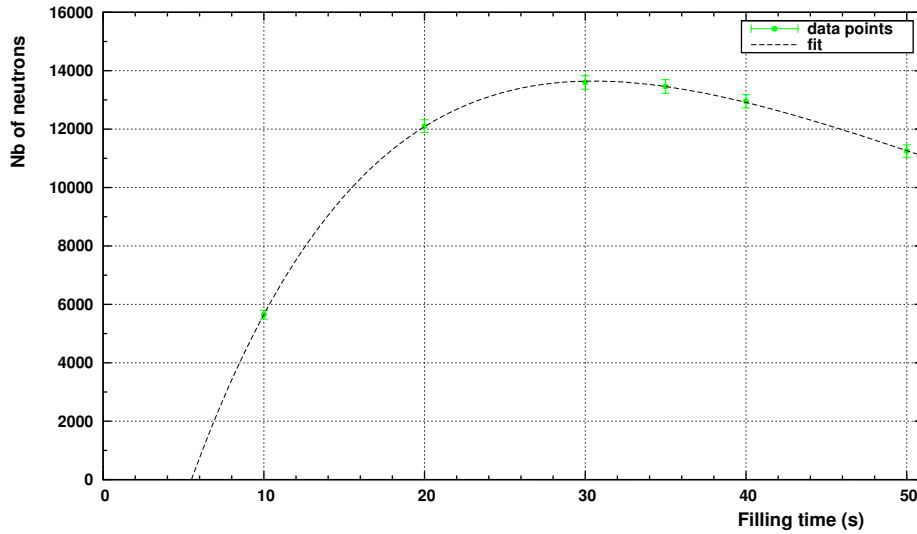


Figure 5.19: Evolution of the number of counted UCN as a function of the filling time.

5.6.3 Storage of the UCN

UCN cannot be stored for a very long time within the chamber since their number will decrease exponentially:

$$N(t) = N_0 e^{-t/\tau_{glob}} \quad (5.20)$$

where N_0 is the initial number of stored UCN, and τ_{glob} the global storage time. This time results from the contribution of two terms: the neutron lifetime τ_n and the storage time T_0 :

$$\tau_{glob} = \left(\frac{1}{\tau_n} + \frac{1}{T_0} \right)^{-1} \quad (5.21)$$

T_0 is the parameter we want to determine. It has two main contributions: the losses due to the absorption in the chamber walls and the losses due to the leaks since the chamber is not a perfectly tight system:

$$T_0 = \left(\frac{1}{\tau_{walls}} + \frac{1}{\tau_{leaks}} \right)^{-1} \quad (5.22)$$

The main contribution comes from the absorption. Different cycles were done with different storage times. The filling time was fixed to 35 s and the counting time to 40 s. Data were normalized using the measurements made when the switch was in the “monitoring” position. The errors are only statistical. The results are shown in Fig. 5.20. A fit with a single exponential gives poor results ($\chi^2/\text{dof}=150$). Therefore two exponentials were used, which can be explained by two populations of UCN : the one called “fast”, with an energy close to the Fermi potential of the walls, and which lives less than the other population of UCN, called “slow”. The two T_0 times are: $T_{0,fast}=53\pm21$ s and $T_{0,slow}=180\pm55$ s. These times are not strictly storage times since only τ_{glob} can be measured. Nevertheless, the measured times are small with respect to the neutron lifetime (Chap. 1) which is the other contribution to τ_{glob} . We can then consider the measured times as T_0 .

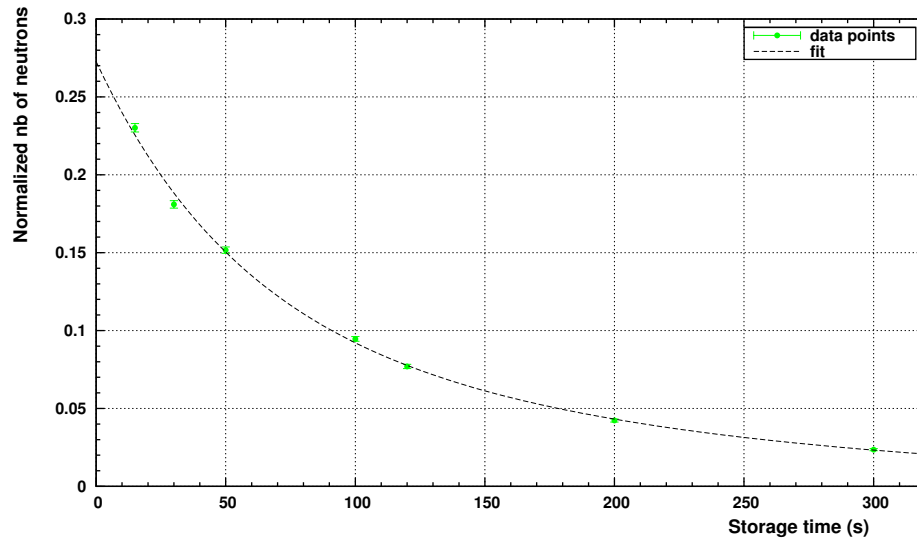


Figure 5.20: Evolution of the number of counted UCN as a function of the storage time. The depicted fit is the sum of two exponentials.

5.6.4 Depolarization within the vertical guide

Once the filling and storage times were determined, the asymmetry was measured. This parameter provides control of a well polarized UCN beam, and a proper preservation of the polarization during UCN motion within the experiment. It is defined as:

$$\mathcal{A} = \frac{N_{up} - N_{down}}{N_{up} + N_{down}} = \frac{N_{SF2,off} - N_{SF2,on}}{N_{SF2,off} + N_{SF2,on}} \quad (5.23)$$

Two measurements are needed to determine the asymmetry. They were done using a filling time of 30 s, a storage time of 40 s and a counting time of 45 s. Data were normalized using the measurements made when the switch was in the “monitoring” position. The errors are statistical. We have: $\mathcal{A} = 73 \pm 0.6\%$. The value was expected to be close to the $A \times P$ term measured before (88.5%), which is not the case. UCN are depolarized in the apparatus. The same measurement was done but with different counting times. the results are shown in Fig. 5.21. The asymmetry decreases exponentially with a depolarization time $\tau_{depol} = 10.8 \pm 0.2$ s. This time is small compared to the used counting/emptying time of about 40 s. It is a problem for the experiment and the cause of such a poor polarization maintenance must be found. This can be due to:

- a bad guiding field
- a magnetic anomaly within the precession chamber
- the collisions on the polarizing foil which can depolarize the UCN

The guiding field was checked first.

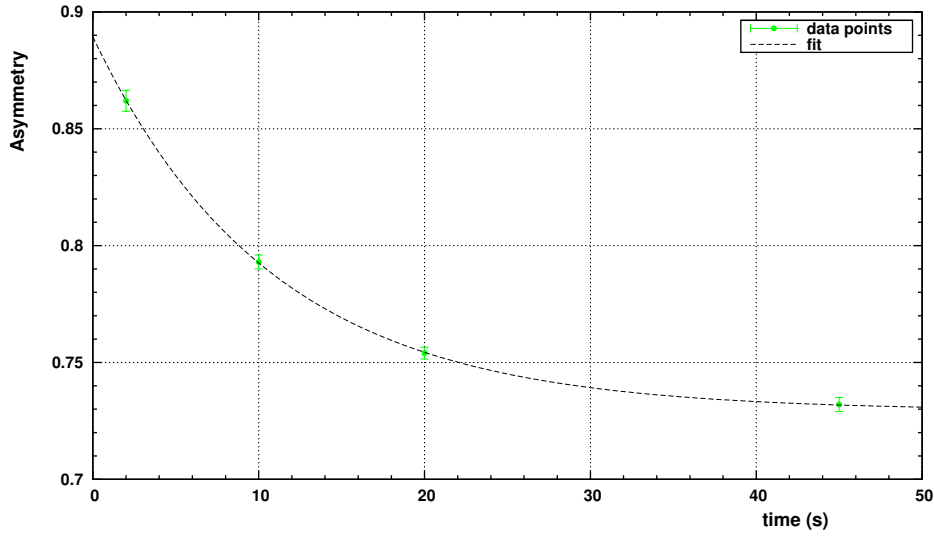


Figure 5.21: Decreasing of the measured asymmetry as a function of the counting time.

5.6.5 Guiding field coils tests

Different guiding field settings were tested and the results are summarized in Table 5.6.

Table 5.6: Summary of the GF tests. The current configuration corresponds to the currents used in each guiding field coil as described in Table 5.4.

Current configuration	Asymmetry \mathcal{A} (%)	tested coil(s)	remark
-20 -100 -60 -60 -40 2 0 -60	73.0 ± 0.6		Default currents
-40 -100 -60 -60 -40 2 0 -60	72.6 ± 0.6	UCK	
-20 0 0 -60 -40 2 0 -60	71.1 ± 0.6	HGSW and HGSC	
-20 -100 60 -60 -40 2 0 -60	55.2 ± 0.8	HGSW and HGSC	
-20 -100 -60 0 -40 2 0 0	69.3 ± 0.7	CSWC and SR	
-20 -100 -60 -60 40 2 0 -60	72.7 ± 0.6	VGSA	
-20 -100 -60 -60 0 2 0 -60	72.7 ± 0.6	VGSA	
-20 -100 -60 -60 60 2 0 -60	71.3 ± 0.6	VGSA	
-20 -100 -60 -60 -40 4 0 -60	73.2 ± 0.6	VGSO	
-20 -100 -60 -60 -40 -2 0 -60	1.6 ± 0.9	VGSO	
0 0 0 0 0 0 0 0	31.7 ± 0.9		
-20 0 0 0 0 0 0 0	71.9 ± 0.6		
0 0 0 0 0 0 0 0	32.3 ± 0.9		B_0 down
0 0 0 0 0 0 0 0	46.3 ± 0.8		B_0 down, no SFC
20 0 0 0 0 0 0 0	70.8 ± 0.6		B_0 down, no SFC

The vertical saddle coil do not improve the polarization, the asymmetry is the same with or without the coil. Finally, the vertical guide correction solenoid gives the same results as the UCK coil: an increase of the current does not improve the asymmetry, but a reverse polarity creates a zero field region, which depolarizes the beam.

With the default current configuration, the measured asymmetry is $\mathcal{A}=73.0\pm0.6\%$. For comparison, a measurement with all currents set to zero gives $\mathcal{A}=31.7\pm0.9\%$. The beam is not fully depolarized because of the stray fields of the analyzer and polarizer. Then the UCK coil was switched to its default current, and the measured asymmetry is: $\mathcal{A}=71.9\pm0.6\%$. The full guiding field system improves the asymmetry by less than 1% compared to the use of the UCK coil only. Finally, it was decided to go back to an ILL configuration where the spin polarization was maintained due to the Earth magnetic field and the field of the analyzer (*i.e.* no guiding coils where used). The SFC coils were switched off in order to not compensate the Earth field, and we get: $\mathcal{A}=70.8\pm0.6\%$. This indicates that an additional depolarization problem (compared to ILL) occurs and cannot be removed by the use of the current guiding field coils.

There are two possibilities to explain the bad polarization maintaining:

- magnetic problems within the vertical guide
- a bad quality of the analyzing foil, which would induce a large depolarization probability.

The second point is certainly more likely, and would explain the $A \times P$ value of 88.5%. Finally, the uselessness of the added coils around the switch and within the vertical guide is certainly due to the large value of the stray field of the analyzer magnets, which is enough to perform an adiabatic transition between the switch and the entrance of the UCK coil. It has lately been decided to use these magnets.

5.6.6 Estimation of the longitudinal depolarization time T_1

Finally, as a conclusion of these measurements, the longitudinal depolarization time T_1 was determined. The evolution of the asymmetry was measured for different storage times. The filling time was fixed and measurements were normalized using the count recorded at the “monitoring” position. Results are shown in Fig. 5.22. We found: $T_1 = 2281 \pm 266$ s. Thus the unexpected depolarization losses comes from the analyzing foil, which has to be changed.

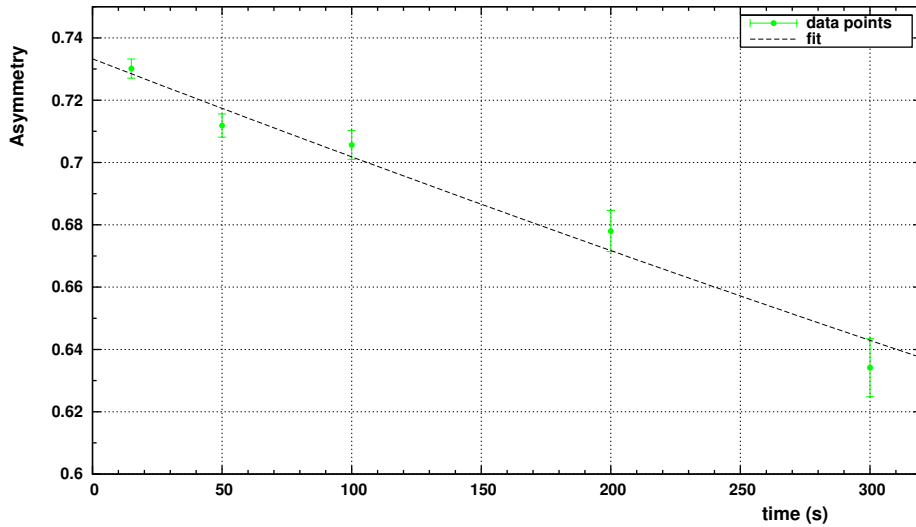


Figure 5.22: Evolution of the asymmetry as a function of the storage time.

5.7 Conclusion

We have seen in this chapter that a superconducting solenoid can be used as an efficient polarizer of ultracold neutrons. The new geometry needed a new system for spin reversal. This system was designed, built and characterized with success. An efficiency consistent with 100% was determined. The guiding field coils system described in Chap. 3 was tested with UCN and several coils are finally not needed to keep the polarization. The performances of the apparatus are lower than expected. This is especially true for the maintenance of the polarization within the vertical guide. This can be due to the analyzing foil which was not characterized with UCN before. A comparison between the measured parameters during phase I and phase II are given in Table 5.7.

Table 5.7: Comparisons of several parameters of the experiment as they were during phase I and as they are now during phase II

Parameter	Value during phase I (from Ref. [4, 61, 90])	Value during phase II (this thesis)
τ_{fill}	40 s	31 ± 1 s
τ_{depol}	unknown	10.8 ± 0.2 s
$A \times P$	more than 85%	$88.5 \pm 0.3\%$
SF1	around 99%	$100.03 \pm 0.08\%$
SF2	around 99%	$99.3 \pm 0.3\%$
\mathcal{A} (45s counting)	unknown	$73.0 \pm 0.3\%$
\mathcal{A} (20s counting)	around 85%	$75.4 \pm 0.5\%$
$T_{0,fast}$	32 ± 1 s	53 ± 21 s
$T_{0,slow}$	226 ± 2 s	180 ± 55 s
T_1	897 ± 39 s	2281 ± 266 s

Conclusions

This work aimed to provide an optimized polarization, a guiding field and an analyzing system for the apparatus used during the Phase II of the measurement. Estimation and measurement of characteristic times of the experiment such as the filling time, the storage time and the longitudinal depolarization times were also performed.

A new guiding field system made of seven coils was designed using two magnetic field simulation codes. The study of the adiabaticity parameter k has been performed for this purpose. The new system was successfully tested and installed at PSI. The magnetic field was mapped with different current configurations. Simulation and measurements are in agreement, and a working configuration was found. The minimal value of k is 20 at the center of the vertical UCN guide, which assure that the polarization is larger than 99.5% in the precession chamber. The system was tested with UCN, and it was shown that some coils can be omitted.

The magnetic field of the superconducting polarizer magnet was mapped. The magnetic field was in agreement with the theoretical field values given by the constructor. Then the SCM was installed on the UCN beamline in 2010. It was simulated using a MC simulation code, and a lower limit of its polarization efficiency was found to be 97.5%. It was not possible to determine directly the efficiency of the polarizer, because the iron foil used as analyzer was not characterized yet. The measured combined polarizing-analyzing efficiency was found to be 88.5 ± 0.3 %, which is below the expected value. Nevertheless, recent fitting of experimental data have shown that its real efficiency is in agreement with the value of 99.9% [89].

A new spin flipper was designed, simulated, built and placed just downstream to the SC magnet. A dedicated beam time was requested and granted at ILL to characterize the spin flipper and to determine its best working parameters. Its efficiency was measured and is in accordance with 100 %. The same performances were measured at PSI with the OILL apparatus.

Losses and depolarizations were simulated using a dedicated MC code. Two storage times of $T_{0,fast}=95\pm5$ s and $T_{0,slow}=328\pm10$ s were determined. They are higher than the experimental values $T_{0,fast}=53\pm21$ s and $T_{0,slow}=180\pm55$ s. This can be due to the UCN tightness of the system which is not as perfect as in the simulations, and also the surface cleanness of the apparatus. Nevertheless, the measured storage time is not a limiting factor for the experiment.

Calculation has shown that the depolarization due to wall collisions for a full experimental cycle is less than 1%. The depolarization due to magnetic field inhomogeneities was obtained via the integration of the Bloch equations during the emptying phase. The percentage of depolarization is less than 4 %. The T_1 depolarization time was estimated to be around 20000 s using two simulations. As expected, the contribution due to magnetic field inhomogeneities was found to be negligible compared to the part due to wall collisions. The measured value is about 2000 s, *i.e* ten times lower. As for the T_0 times, this difference may come from the cleanness of the electrodes.

Finally, the asymmetry was measured after a full measurement cycle without RF field. The measured value for a counting time of 45 s is $73.0 \pm 0.3\%$. This value may be improved by changing the analyzing system. Dedicated measurements must be done in order to optimize the efficiency. Then the polarization-analysis system will be competitive for a new measurement of the electric dipole moment at PSI.

Bibliography

- [1] A. Sakharov, JETP Letters **5**, 24 (1967).
- [2] M. Pospelov and A. Ritz, Annals Phys. **318**, 119 (2005).
- [3] C. A. Baker et al., Phys. Rev. Lett. **97**, 131801 (2006).
- [4] S. Roccia, *La co-magnétométrie mercure pour la mesure du moment électrique dipolaire du neutron. Optimisation et application au test de l'invariance de Lorentz*, PhD thesis, Université Joseph Fourier, Grenoble, 2009.
- [5] E. M. Purcell and N. F. Ramsey, Phys. Rev. **78**, 807 (1950).
- [6] E. M. Purcell and N. F. Ramsey, Phys. Rev. **78**, 695 (1950).
- [7] W. W. Havens, I. I. Rabi, and L. J. Rainwater, Phys. Rev. **72**, 634 (1947).
- [8] J. H. Smith, E. M. Purcell, and N. F. Ramsey, Phys. Rev. **108**, 120 (1957).
- [9] W. B. Dress, P. D. Miller, J. M. Pendlebury, P. Perrin, and N. F. Ramsey, Phys. Rev. D **15**, 9 (1977).
- [10] I. Altarev et al., Nuclear Physics A **341**, 269 (1980).
- [11] I. B. Khriplovich and S. K. Lamoreaux, *CP violation without strangeness*, Springer-Verlag, Berlin, Heidelberg and New York, 1997.
- [12] M. Pospelov and A. Ritz, Nuclear Physics B **558**, 243 (1999).
- [13] J. Ellis and M. K. Gaillard, Nuclear Physics B **150**, 141 (1979).
- [14] V. Baluni, Phys. Rev. D **19**, 2227 (1979).
- [15] M. Dine, arXiv :hep-ph/0011376v2, 2000.

- [16] R. D. Peccei and H. R. Quinn, Phys. Rev. Lett. **38**, 1440 (1977).
- [17] E. P. Shabalin, Sov. J. Nucl. Phys. **28**, 75 (1978).
- [18] D. V. Nanopoulos et al., Phys. Lett. B **87**, 53 (1979).
- [19] G. Taubes, Science **278**, 226 (1997).
- [20] S. Dodelson, *Modern Cosmology*, Academic Publisher, San Diego, 2003.
- [21] H. E. Haber and G. L. Kane, Phys. Rep. **117**, 75 (1985).
- [22] S. Baek and P. Ko, arXiv :hep-ph/9909433v1, 1999.
- [23] L. I. Schiff, Phys. Rev. **132**, 2194 (1963).
- [24] B. C. Regan, E. D. Commins, C. J. Schmidt, and D. DeMille, Phys. Rev. Lett. **88**, 071805 (2002).
- [25] V. F. Dmitriev and R. A. Sen'kov, Phys. Rev. Lett. **91**, 212303 (2003).
- [26] J. Angel, P. Sandars, and M. Tinker, Physics Letters A **25**, 160 (1967).
- [27] P. D. Miller et al., Phys. Rev. Lett. **19**, 381 (1967).
- [28] C. G. Shull and R. Nathans, Phys. Rev. Lett. **19**, 384 (1967).
- [29] W. B. Dress et al., Phys. Rev. **170**, 1200 (1968).
- [30] J. K. Baird et al., Phys. Rev. **179**, 1285 (1969).
- [31] W. B. Dress et al., Phys. Rev. D **7**, 3147 (1973).
- [32] I. S. Altarev et al., Phys. Lett. B **102**, 13 (1981).
- [33] J. M. Pendlebury et al., Phys. Lett. B **137**, 327 (1984).
- [34] I. S. Altarev et al., JETP Lett. **44**, 360 (1986).
- [35] K. F. Smith et al., Phys. Lett. B **108**, 191 (1990).
- [36] I. S. Altarev et al., Phys. Lett. B **276**, 242 (1991).
- [37] I. S. Altarev et al., Phys. Atom. Nucl. **59**, 1152 (1996).
- [38] P. G. Harris et al., Phys. Rev. Lett. **82**, 904 (1999).
- [39] J. Chadwick, Proc. Roy. Soc. A **136**, 692 (1932).
- [40] E. Fermi, Ricerca scientifica **7**, 13 (1936).
- [41] E. Fermi and L. Marshall, Phys. Rev. **71**, 666 (1947).
- [42] Y. B. Zeldovich, Sov. Phys.-JETP **36**, 1952 (1959).

- [43] A. P. Serebrov et al., Phys. Rev. C **78**, 035505 (2008).
- [44] R. Golub, D. Richardson, and S. K. Lamoreaux, *Ultra-cold Neutrons*, Adam Hilger, Bristol, Philadelphia and New York, 1991.
- [45] V. K. Ignatovich, *The Physics of Ultracold Neutrons*, The Clarendon Press, Oxford, 1990.
- [46] P. J. Mohr, B. N. Taylor, and D. B. Newell, Rev. Mod. Phys. **80**, 633 (2008).
- [47] F. Bloch, Phys. Rev. **70**, 460 (1946).
- [48] A. I. Egorov et al., Yad. Fiz. **19**, 300 (1974).
- [49] A. P. Serebrov et al., J. Res. Natl. Inst. Stand. Technol. **110**, 185 (2005).
- [50] J. Baumann, R. Gähler, J. Kalus, and W. Mampe, Phys. Rev. D **37**, 3107 (1988).
- [51] V. Fedorov, I. Kuznetsov, E. Lapin, S. Semenikhin, and V. Voronin, Nucl. Instr. and Meth. A **593**, 505 (2008).
- [52] C. Plonka-Spehr et al., Nucl. Instr. and Meth. A **618**, 239 (2010).
- [53] A. Alexandru and F. Lee, arXiv :0911.2520v1, 2009.
- [54] R. Hildebrandt, H. Griesshammer, and T. Hemmert, The European Physical Journal A - Hadrons and Nuclei **46**, 111 (2010).
- [55] C. A. Baker et al., Phys. Lett. A **308**, 67 (2003).
- [56] R. Golub and J. M. Pendlebury, Physics Letters A **62**, 337 (1977).
- [57] H. Yoshiki et al., Phys. Rev. Lett. **68**, 1323 (1992).
- [58] Description of the proton cyclotron at PSI, <http://abe.web.psi.ch/accelerators/ringcyc.php>.
- [59] A. Anghel et al., Nucl. Instr. and Meth. A **611**, 272 (2009).
- [60] P. G. Harris et al., Nucl. Instr. and Meth. A **440**, 479 (2000).
- [61] A. Knecht, *Toward a new measurement of the neutron electric dipole moment*, PhD thesis, Universität Zürich, 2009.
- [62] B. Blau et al., Physics Procedia, not yet published.
- [63] L. Göttl, Private communication.
- [64] L. Göttl, *Measurements and Procedures for the Construction and Characterization of Ultra-Cold Neutron Guides*, Master's thesis, Universität Heidelberg, 2008.
- [65] J. Zenner, PhD thesis, Johannes Gutenberg-Universität Mainz, 2012, in preparation.
- [66] K. Bodek et al., Nucl. Instr. and Meth. A **597**, 222 (2008).

- [67] G. Ban et al., Nucl. Instr. and Meth. A **611**, 280 (2009).
- [68] G. Ban et al., Phys. Rev. **110**, 283 (2005).
- [69] K. Green et al., Nucl. Instr. and Meth. A **404**, 381 (1998).
- [70] M. Horras, *A highly sensitive Hg magnetometer for the nEDM experiment*, PhD thesis, ETH Zürich, 2012, in preparation.
- [71] M. Fertl, PhD thesis, ETH Zürich, 2012, in preparation.
- [72] B. Franke, PhD thesis, ETH Zürich, 2013, in preparation.
- [73] R. R. Newton and C. Kittel, Phys. Rev. **74**, 1604 (1948).
- [74] V. V. Vladimirov, Sov. Phys. JETP **12**, 740 (1960).
- [75] O. Chubar, P. Elleaume, and J. Chavanne, Radia, magnetic field computation code, <http://www.esrf.eu/Accelerators/Groups/InsertionDevices/Software/Radia>.
- [76] G. Quémener, Maentouch, private communication.
- [77] P. Elleaume, O. Chubar, and J. Chavanne, proc. of the PAC97 Conference, 3509 (1997).
- [78] Wolfram mathematica, <http://www.wolfram.com/mathematica/>.
- [79] H. Hanssum, J. Phys. D: Appl. Phys. **17**, 18 (1984).
- [80] C. E. G. Salmon et al., Brazilian Journal of Physics **36**, 6 (2006).
- [81] G. Quémener, Notes on field computation using the homemade program MAENTOUCH, 2007.
- [82] Bartington instruments, <http://www.bartington.com>.
- [83] A. Moldovanu et al., Sensors and Actuators A: Physical **59**, 113 (1997), 1st European magnetic sensors and actuators conference.
- [84] F. Atchison et al., Nucl. Instr. and Meth. A **552**, 513 (2005).
- [85] S. Agostinelli et al., Nucl. Instr. and Meth. A **506**, 250 (2003).
- [86] J. Allison et al., IEEE Trans. on Nucl. Sci. **53**, 270 (2006).
- [87] A. J. Dianoux and G. Lander, *Neutron Data Booklet*, OCP Science, Institut Laue-Langevin, Grenoble, 2003.
- [88] C. H. Westcott, W. H. Walker, and T. K. Alexander, Proc. 2nd Intern. Conf. Peaceful uses atomic energy Geneva (3rd ed.), 70 (1958).
- [89] G. Zsigmond, Private communication.

- [90] G. Rogel, *Développement de détecteurs de neutrons ultra-froids et d'un système d'analyse de polarisation pour la mesure du moment électrique dipolaire du neutron*, PhD thesis, Université de Caen Basse-Normandie, 2009.
- [91] D. J. R. May, *A High Precision Comparison Of The Gyromagnetic Ratios Of The ^{199}Hg Atom And The Neutron*, PhD thesis, University of Sussex, 1998.
- [92] P. Seeger and L. Daemen, Nucl. Instr. and Meth. A **457**, 338 (2001).
- [93] W. H. Press, S. A. Teutolsky, W. T. Vetterling, and B. P. Flannery, *Numerical recipes in C*, Cambridge University Press, Cambridge, New York, Port Chester, Melbourne and Sydney, 1997.
- [94] A. G. Redfield, IBM J. Res. Develop. **19** (1957).
- [95] J. Pendlebury and D. Richardson, Nucl. Instr. and Meth. A **337**, 504 (1994).
- [96] R. J. E. Clausius, *Die mechanische Wärmetheorie, Band III*, Adamant Media Corporation, New York, 2001.
- [97] P. Fierlinger, *Loss and depolarization studies of ultracold neutrons stored using Diamond-like carbon*, PhD thesis, Universität Zürich, 2005.
- [98] G. Pignol and S. Roccia, Phys. Rev. A **85**, 042105 (2012).
- [99] C. P. Slichter, *Principles of Magnetic Resonance*, Springer-Verlag, Berlin, Heidelberg and New York, 1990.
- [100] J. M. Pendlebury et al., Phys. Rev. A **70**, 032102 (2004).
- [101] Z. Chowdhuri, Private communication.
- [102] Lakeshore instruments, <http://www.lakeshore.com>.
- [103] Senis GmbH, magnetic and current measurement, <http://www.senis.ch>.
- [104] V. I. Luschikov and Y. V. Taran, Nucl. Instr. and Meth. **228**, 159 (1984).
- [105] H. Weinfurter and G. Badurek, Nucl. Instr. and Meth. A **275**, 233 (1989).
- [106] A. P. Serebrov et al., Nucl. Instr. and Meth. A **357**, 503 (1995).
- [107] R. Herdin et al., Nucl. Instr. and Meth. **148**, 353 (1978).
- [108] T. Lefort, Private communication.

APPENDIX

A

Appendix

.1 The monitoring using an external detector

There are two ways to monitor the UCN flux during the experiment:

- by using the Cascade U detector connected to the West-2 beamline.
- by using the monitoring position of the switch during storage of UCN.

The flux stability was tested by comparing the number of detected neutrons recorded during 31 successive runs. These runs had the same filling times ($t=35$ s). For all the runs, the average number of neutrons and the standard deviation was calculated. We have:

- monitor West-2: $N=131124\pm6245$ (standard deviation of 4.8%)
- switch monitoring position: $N=69877\pm1486$ (standard deviation of 2.1%)

The switch monitoring position gives a lower standard deviation. The correlation between the two monitors was studied by plotting N_{west2} as a function of N_{switch} . The mean value of the ratio of the two monitors and the standard deviation were calculated. We get: $N_{\text{west2}}/N_{\text{switch}}=1.876\pm0.076$ (deviation of 4%). The correlation plot is shown in Fig. 1.

We can see that the correlation between the monitor West-2 and the monitoring switch position is not clear. When it is possible, we decided to use the switch monitor instead of the West-2 monitor, it is closest to the experiment and uses the same energy range UCN as in the experiment (UCN placed at the bottom of the tank are going in the EDM apparatus, and UCN at the top of the tank are going in the West-2 beamline). Furthermore, the results obtained with the cascade-U detector are not self consistent (for instance a spin flipper efficiency $>100\%$).

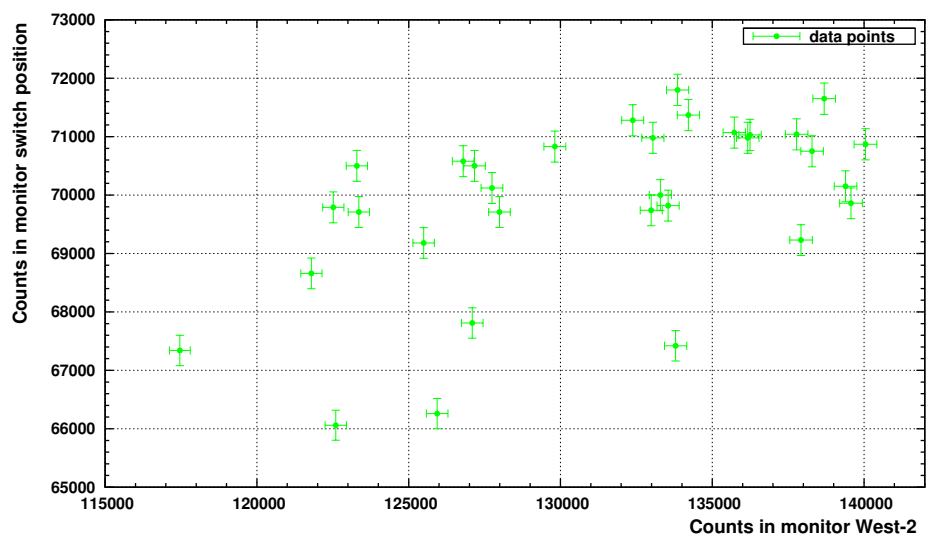


Figure 1: Correlations between the number of counted neutrons using the West-2 Cascade-U monitor and the “monitoring” position of the Switch.

List of Tables

1.1	UCN and interaction strengths.	31
1.2	Fermi potentials, critical velocities and losses factor (Sec. 1.2.2) of materials used in UCN physics.	32
1.3	Summary of UCN sources around the world.	37
2.1	Measured shielding factor at PSI	48
3.1	Mapping of the analyzer stray field modulus compared to the simulated one in RADIA. $z = 0$ corresponds to the center of the return yoke. The z direction is the same as the experiment	57
3.2	Dimensions and positions of the 6 SFC coils used in the RADIA simulation. All the distances are given in cm. The offsets are the differences between the position of the coil pairs center and the experiment reference frame origin.	59
3.3	Adiabaticity parameter as a function of the gap between the two solenoids.	60
3.4	Characteristics of the coils used for the horizontal spin guiding system.	61
3.5	Characteristics of the coils used for the vertical guide holding field.	66
3.6	Minimum adiabaticity parameter in the expected low adiabaticity region.	80
4.1	Physical properties of the materials used in the simulation.	87
4.2	Summary of the depolarization estimates during the filling phase after a time τ_{fill}	91
4.3	Summary of the depolarization estimates during the storage phase ($t = 100$ s).	92
4.4	Summary of the depolarization estimates during the emptying phase.	93
5.1	Far stray field created by the SC magnet measured with a fluxgate.	106
5.2	Scanning in frequency for the RF coil. The resonance frequency is 22.5 kHz. At 20 and 25 kHz the efficiency is also 100 %.	112
5.3	Characteristics of the two spin flippers used and their measured efficiencies	114
5.4	Guiding field coils and their applied currents	116
5.5	Value of the asymmetry as a function of the polarizer magnetic field.	117

5.6	Summary of the GF tests. The current configuration corresponds to the currents used in each guiding field coil as described in Table 5.4.	121
5.7	Comparisons of several parameters of the experiment as they were during phase I and as they are now during phase II	123

List of Figures

1.1	Évolution de la limite sur la valeur du moment dipolaire électrique du neutron. .	6
2.1	Schéma de l'expérience nEDM à PSI.	11
3.1	Principe de polarisation de neutrons à travers une feuille de fer. Le potentiel vu par le neutron dépend de son spin.	14
3.2	Evolution du spin durant le processus de renversement de spin. Le champ magnétique B_0 est selon l'axe z , et le champ RF B_1 selon l'axe x	16
3.3	Appareillage OILL en configuration pour la mesure d'efficacité de polarisation. .	17
1.1	Scheme showing the CP and T violation of a particle with an electric dipole moment.	26
1.2	Constraints imposed by the neutron, thallium and mercury EDM on the two phases θ_A and θ_μ . Picture taken from [2]	27
1.3	Evolution on the nEDM limit with time [3, 6, 8–10, 27–38].	29
1.4	Expected reachable sensitivities for the six nEDM experiments: PNPI collaboration (ILL, Gatchina), nEDM collaboration (PSI), Japan-Canada collaboration (RCNP, TRIUMF), CryoEDM (ILL), Munich experiment (TUM) and US collaboration (LANL)	29
1.5	Potential step with incident, transmitted and reflected waves.	33
1.6	Reflection and transmission coefficients for a UCN incident with a perpendicular energy E upon a Fermi potential V	33
1.7	Feynman diagram of the neutron beta decay.	34
1.8	Principle of the polarization using a magnetic field. The potential experienced by the neutron depends on its spin (spin and magnetic moment of the neutron are anti-aligned).	36

1.9	Velocity distributions for 300 K neutrons (D ₂ O moderator), 20 K neutrons (L D ₂ moderator) and 5 K neutrons (S D ₂ moderator). A minimal part of the distribution are UCN, even with a very cold moderator (about 10^{-11} for 300 K, 10^{-9} for 20 K and 10^{-8} for 5 K).	37
1.10	The PSI UCN source.	38
2.1	Energy levels of a neutron in the presence of collinear magnetic and electric fields.	40
2.2	Ramsey Curve measured by the Sussex/RAL/ILL collaboration, and taken from [60].	41
2.3	A global scheme of the OILL apparatus at PSI. More details are given in the text.	43
2.4	The UCN switchbox.	45
2.5	The multi-detector Nanosc.	46
2.6	Drawing of the B_0 coil. This geometry is used for magnetic field simulations (Chap. 3)	48
2.7	The trim coils.	49
2.8	Drawing of the SFC coils	50
3.1	Evolution of P_z after a $\pi/2$ rotation of the magnetic field as a function of the adiabaticity parameter.	53
3.2	Modulus of the magnetic field at the center of the vertical guide as a function of the height for a B_0 down configuration. (0 cm corresponds to the center of the precession chamber) Black dots are from a measurement performed at PSI with SFC ON. Empty squares were done at ILL and comes from [4]. Red lines corresponds to the positions of the four shielding layers. No trim coils were used.	55
3.3	Scheme showing the nEDM experiment and main magnetic field sources. The arrows are the direction of the magnetic field. Red ellipses corresponds to regions where low field is expected. The experiment reference frame is also depicted.	55
3.4	Adiabaticity parameter k along the vertical guide at PSI with no trim coils. The values of k are definitely bellow the requirement.	56
3.5	Axial stray field of the superconducting magnet. Black dots represents the field at the center of the UCN guide, empty squares the field at the edges of the UCN guide and the red line is the fit. $x = 0$ corresponds to the center of the SC magnet.	58
3.6	The analyzer and its RADIA model. The four magnets are in blue, the return yoke is in red). RADIA parameters were adjusted to fit with the real analyzer field (Table 3.1).	59
3.7	Simulated field along the horizontal guide with guiding coils added (red line) and without (black line). A $60 \mu\text{T}$ holding field was assumed. The zero here is the crossing point between horizontal and vertical guide.	60
3.8	Rotation of the field close to the horizontal wire of the rectangular coil (the coil is in the yOz plane, the plane of the plot, xOz , is a plane of symmetry for the coil). The red circle denotes the cross section of the horizontal wire.	62
3.9	Scheme of a saddle coil pair with its tunable parameters: the length L , the radius R and the aperture angle α .	63
3.10	Homogeneity at the center of the saddle coils (black dots) and at the edge of the saddle coils (empty squares). The optimum radius is 90 mm.	64

3.11	Field homogeneity in the xOy plane, at the center of the saddle coils (left picture) and at the edge of the saddle coils (right picture). The red circle represents the edge of the UCN guide.	64
3.12	Field homogeneity at the center of the saddle coils as a function of the aperture angle of the coils. The largest field homogeneity (<i>i.e.</i> smallest quality factor) is found for $\alpha=128^\circ$	65
3.13	Left picture: Effect of the correction solenoid on the adiabaticity parameter k for a B_0 down configuration. k increases from 2 to more than 20 where the horizontal wire of the saddle coil crosses the vertical guide. Right picture: The effect can be understood easily by looking at the relative angle between the magnetic field and the z axis. Due to the correction solenoid, the magnetic field rotates more smoothly so that the neutron spin is able to follow it.	66
3.14	Picture of the wooden plate fixed below the magnetic shield (left side), and detail of this plate with the plexiglass stick in (right side).	67
3.15	Comparison between the field computed with RADIA (empty squares) and the measured field (black dots). Inside the cylinder, the difference between measured and calculated field is about 5 %.	68
3.16	Difference of the results of Radia and Maentouch simulations, for the same system composed by a vertical Mu-metal cylinder with the saddle coils pair and the correction solenoid. The difference between the two codes is less than 1 %. . . .	69
3.17	Geometry used in MAENTOUCH simulation. (1) Shielding layers. (2) $B_0 \cos\theta$ -like coil. (3) UCN “Kamin” coil. One can see the vertical Mu-metal cylinder behind the coil. (4) Saddle coil pair. (5) Horizontal solenoid. (6) Switch coils. . .	70
3.18	Simulated adiabaticity along the vertical guide (at the axis) using MAENTOUCH. The minimum value of the coefficient is larger than the requirement. It is located at the level of the horizontal wires of the saddle coils. The second area with a low adiabaticity factor is located at -120 cm. It corresponds to the horizontal wires of the switch coils. The peaks observed arise from the small gradient between two calculated points, so the adiabaticity can be huge. The critical regions are the ones with a low adiabaticity.	71
3.19	New coils setup. (1) First rectangular switch coil. (2) Second rectangular switch coil. (3) Horizontal solenoid. (4) Square switch coil. (5) Saddle coils pair with the correction solenoids.	72
3.20	Scheme of the end of the 3-axis Bartington fluxgate. Each sensor is at 1.5 cm from the next one.	73
3.21	Scheme of the possible positions of the fluxgate in the vertical guide.	73
3.22	Drawing of the mapper used, in on axis configuration (left side), and off axis configuration (right side). The orange part is fixed to the switchbox with five aluminum bars. The plexiglass tube is going through the UCN dummy guide. . .	74
3.23	Definition of the mixing angle ϕ in the xy plane.	74
3.24	Comparison between a magnetic field mapping (black dots) and the simulation (empty squares) of the three components of the magnetic field.	77
3.25	Comparison of the adiabaticity parameter between a magnetic field mapping (black dots) and the associated simulation (empty squares)	78

3.26	Comparison of the adiabaticity parameter between a magnetic field mapping (black dots) and the associated simulation (empty squares) for two off axis places: where the contribution of the field generated by the saddle coils is the smallest (left picture, position 90°) and where the contribution of the field generated by the saddle coils is the largest (right picture, position 180°)	78
3.27	Adiabaticity plots for B_0 up (left) and B_0 down (right). The same behavior is observed for both polarities: the minimum value of k is the same.	79
3.28	Adiabaticity parameter as a function of the vertical position z . Open squares correspond to measurements performed on axis, black dots to measurements performed off axis (26 mm from the center, angle: 315°).	80
3.29	Effect of the UCK coil on the adiabaticity. Black dots: no UCK coil. Open squares: UCK coil at 20 mA. With a current of 20 mA, the adiabaticity near the internal shielding layer is larger by a factor of 10.	81
3.30	Stray field of the Guiding Field coils measured in the precession chamber using the Cs magnetometer. The full squares correspond to Cs magnetometers above the precession chamber, the empty squares to Cs magnetometers below the chamber. The abscissa axis is a rotation angle (the Cs magnetometers can rotate around the Z axis).	82
3.31	Effect of the Mu-metal cylinder placed around the horizontal wire of the switch coils. Black dots: no shield. Open squares: shield used. The adiabaticity parameter is three times higher when the shield is used.	83
3.32	Design of the new saddle coil. The top radius was enlarged by 2 cm.	83
3.33	Adiabaticity parameter at the center of the vertical guide with the first setup (blue line) and the improved setup (new analyzer associated to the modified saddle coil pair, black line).	84
4.1	Scheme of the geometry used in the MC simulation.	88
4.2	Geant4 initial velocity distributions.	89
4.3	Velocity distribution at the entrance of the switchbox. The black line depicts the full UCN beam, and the red line the non-polarized fraction.	90
4.4	Initial velocity distribution for the storage and emptying phases.	91
4.5	Number of UCN within the chamber as a function of the storage time T	92
4.6	Depolarization of the wrong and right spin states UCN as a function of time.	94
4.7	Evolution of the asymmetry for different storage times.	96
4.8	The “trumpet-like” magnetic field (vertical gradient). Picture taken from [100].	97
4.9	Position autocorrelation functions.	98
4.10	Fourier transform of the x position autocorrelation function. The points correspond to different diffuse reflection probabilities as indicated.	99
4.11	Dependence of the longitudinal depolarization time T_1 as a function of the vertical magnetic field gradient. The points correspond to different diffuse reflection probabilities as indicated.	99
5.1	Foil magnetizations as a function of the applied magnetic field. Picture taken from [101].	102
5.2	Picture of the superconducting polarizer.	103

5.3	Theoretical magnetic field profile created by the SC magnet polarizer. $z=0$ and $r=0$ denote the center of the magnet.	104
5.4	Magnetic field at the center of the SC magnet. Measured and calculated magnetic fields are given. Error bars for the measured points are smaller than the points.	105
5.5	Measured and calculated axial magnetic field on axis. $z = 0$ denotes the center of the magnet.	106
5.6	Evolution of the spin during the spin flip process. In this scheme, the B_0 field is along the z axis, and the B_1 field along the x axis.	107
5.7	Field created by the RF coil. $X=Y=Z=0$ is the center of the coil. r is an arbitrary distance of 50 mm.	108
5.8	The new vertical field adiabatic spin flipper.	109
5.9	Axial magnetic field created by the SCM compared to the one created by the gradient coils. r is in cm. $x=0$ is the center of the SC magnet.	110
5.10	The static gradient coils scheme (cut). Their length allow us to use the resonance point for the spin flipper between 700 and 1500 μT as expected. The radius is 150 mm, and the current used in each coil is (from left to right): 5.33 A, 2.22 A, 0.6 A	111
5.11	Scheme of the experiment. The chopper was not used in this measurement.	111
5.12	Photo of the experiment. The corrections coils (thin solenoids between the two gradient coils) are not used since the Earth field is large enough to keep the polarization between the two gradient coils.	111
5.13	Comparison between theoretical dependence of the spin flipper efficiency with the adiabaticity parameter (line) and experimental results (dots).	112
5.14	Spin flipper efficiency for 25 identical measurements.	113
5.15	Experimental setup for the polarizing-analyzing efficiency determination. Only the SF1 spin flipper is used for this part.	115
5.16	TOF spectrum with and without spin flipper.	115
5.17	UCN charge spectrum. The cut at channel 5000 is shown. The UCN contribution is denoted in yellow, and the γ -noise contribution is denoted in red.	116
5.18	Example of a time sequence. The monitoring and counting periods are indicated.	118
5.19	Evolution of the number of counted UCN as a function of the filling time.	118
5.20	Evolution of the number of counted UCN as a function of the storage time. The depicted fit is the sum of two exponentials.	119
5.21	Decreasing of the measured asymmetry as a function of the counting time.	120
5.22	Evolution of the asymmetry as a function of the storage time.	122
1	Correlations between the number of counted neutrons using the West-2 Cascade-U monitor and the “monitoring” position of the Switch.	ii

List of Symbols

α	Visibility
α_n	Neutron Polarizability
β	UCN depolarization probability per wall reflection
χ	Magnetic susceptibility
η	UCN loss probability per wall reflection
η_{exp}	Experimental baryon to photon ratio
η_{theo}	Theoretical baryon to photon ratio
γ_n	Neutron gyromagnetic ratio
λ_n	Neutron wavelength
\mathcal{A}	Asymmetry
\mathcal{L}_θ	QCD Lagrangian
$\mu(E_\perp)$	Energy dependent UCN loss probability
μ_n	Neutron magnetic dipole moment
ω_L	Larmor precession frequency
σ_{abs}	Absorption cross section
τ_{fill}	Filling time
τ_n	Neutron lifetime

d_n	Neutron Electric Dipole Moment
$F_{\mu\nu}$	Gluon field strength tensor
FT	Fourier transform
g	Earth's gravitational acceleration
h, \hbar	Planck's constant
J	Angular momentum
k	Adiabaticity parameter
M	Magnetization
m_n	Neutron mass
P	Polarization
p_{diff}	Probability of diffuse reflection
q_n	Neutron charge
R_i	Autocorrelation function
T_0	Storage time
T_1	Longitudinal depolarization time
T_2	Transversal depolarization time
v_c	Critical velocity
V_F	Fermi potential
W	Imaginary part of the Fermi potential

List of Abbreviations

ANL	Argonne National Laboratory
BAU	Baryon Asymmetry of the Universe
BIM	Boundary Integral Method
BNL	Brookhaven National Laboratory
CERN	Centre Européen de la Recherche Nucléaire
CKM	Cabibbo-Kobayashi-Maskawa
CN	Cold Neutron
CP	Charge-Parity
CSWC	Central SWitch Coil
DAQ	Data Acquisition
DLC	Diamond-like Carbon
dPS	Deuterated Polystyrene
EDM	Electric Dipole Moment
EM	Electromagnetic
FT	Fourier transform
HGSW	Horizontal Guide SWitch side solenoid
HGSC	Horizontal Guide SC magnet side solenoid

HV	High Voltage
ILL	Institut Laue-Langevin
LANL	Los Alamos National Laboratory
MC	Monte Carlo
MDM	magnetic dipole moment
MIT	Massachusetts Institute of Technology
MSSM	minimal supersymmetric standard model
nEDM	Neutron Electric Dipole Moment
NiMo	Nickel Molybdenum
OILL	Old ILL apparatus
ORNL	Oak Ridge National Laboratory
PMT	Photomultiplier tube
PNPI	Petersburg Nuclear Physics Institute
PSI	Paul Scherrer Institut
QCD	Quantum Chromodynamics
RAL	Rutherford Appleton Laboratory
RF	radiofrequency
SC	Superconducting
SCM	Superconducting polarizer magnet
SF	Spin Flipper
SFC	Surrounding Field Compensation
SINQ	Swiss Spallation Neutron Source
SM	Standard Model
SNS	Spallation Neutron Source
SR	Switch Rectangular coils
SS	Stainless Steel
SUSY	Super Symmetry
TRIGA	Training, Research, Isotopes, General Atomics

UCN	Ultracold Neutron
UCK	UCN “Kamin”
UV	Ultraviolet (light)
VCN	Very Cold Neutron
VGSA	Vertical Guide Saddle coil
VGSO	Vertical Guide Solenoid

TITRE

Développement et optimisation d'un système de polarisation de neutrons ultra froids dans le cadre d'une nouvelle mesure du moment dipolaire électrique du neutron.

RÉSUMÉ

Le travail réalisé dans ce mémoire de thèse s'inscrit dans le cadre d'une expérience effectuée à l'institut Paul Scherrer (PSI) et dédiée à la mesure du moment dipolaire électrique du neutron (nEDM). Une sensibilité de 10^{-27} e.cm est attendue à la fin 2013. La mesure est réalisée avec des neutrons ultra-froids (UCN) polarisés. Pour ce faire, de nouveaux systèmes de polarisation, de transport et d'inversion de spin ont été réalisés. Leur étude est présentée dans ce mémoire. Ils sont actuellement utilisés auprès de l'expérience. Grâce à des mesures de champs magnétiques effectuées sur le spectromètre, des simulations de champs réalisées avec les codes Radia et Maentouch, ainsi qu'à des simulations Monte-Carlo effectuées avec le code Geant4, l'efficacité du dispositif de polarisation a été calculée. L'efficacité mesurée en direct est de $88.5 \pm 0.3\%$, soit légèrement moins que la valeur attendue de 95%. Par ailleurs, la prise de données préliminaire effectuée en octobre 2011 a permis de déterminer certains des paramètres fondamentaux de l'expérience, tel les constantes de temps de remplissage, de stockage et de dépolarisation longitudinale du spectromètre. Ces paramètres sont encourageants pour la suite de l'expérience.

MOT-CLEFS

Neutrons – Polarisation, Neutrons ultrafroids, Moments dipolaires, Spin
Mesure de précision

TITLE

Development and optimisation of a ultracold neutron polarizing system in the framework of a new measurement of the neutron electric dipole moment.

ABSTRACT

The work presented in this thesis has been performed within the framework of an experiment located at the Paul Scherrer Institut (PSI) and dedicated to the measurement of the neutron electric dipole moment (nEDM). The expected sensitivity is 10^{-27} e.cm at the end of 2013. The experiment requires a polarized ultracold neutron (UCN) beam. A new polarizing system, a spin transport device and a spin reversal system have been developed for this purpose. Their study is detailed in this thesis. These systems are currently installed on the experiment. Thanks to magnetic field mappings done on the spectrometer, to magnetic field simulations using the Radia and Maentouch programs and also to Monte-Carlo simulations using the Geant4 software, the efficiency of the device has been calculated. The measured efficiency is $88.5 \pm 0.3\%$, which is slightly less than the expected value of 95%. Furthermore, this preliminary data taken in October 2011 allows the determination of some fundamental parameters of the experiment such as the filling, storage and longitudinal depolarization time constants of the spectrometer. These parameters are promising for the continuation of the experiment.

KEYWORDS

Neutrons – Polarization, Ultracold neutrons, Dipole moments, Nuclear spin
